國 立 交 通 大 學

光電工程研究所

博 士 論 文

成長與製作高效率氮化鎵系列發光元件

Growth and fabrication of high efficiency GaN based light emitting devices

研 究 生：羅明華

指導教授：王興宗 教授

郭浩中 教授

中華民國九十九年十月

成長與製作高效率氮化鎵系列發光元件

Growth and fabrication of high efficiency GaN based light emitting devices

研 究 生：羅明華 Student : Ming-Hua Lo

指導教授：王興宗 Advisor : Shing-Chung Wang

郭浩中 Hao-Chung Kuo

國 立 交 通 大 學

光 電 工 程 研 究 所

博 士 論 文

A dissertation

Submitted to Department of Electro-Optical Engineering

College of Electrical Engineering and Computer Science

National Chiao Tung University

In partial Fulfillment of the Requirements

For the Degree of

Doctor in Philosophy

In Electro-Optical Engineering

October 2010

Hsinchu, Taiwan, Republic of China

中華民國九十九年十月

成長與製作高效率氮化鎵系列發光元件

學生：羅明華　　　　　　　　　指導教授：王興宗 教授

郭浩中 教授

國立交通大學光電工程研究所

摘 要

近年來，寬能隙氮化鎵系列半導體是製作寬波長發光元件非常重要的材料系統。其中氮化鎵雷射與發光二極體元件已經很廣泛利用於很多領域，如光資訊儲存、液晶顯示器背光光源、交通號誌與固態照明。

在本研究論文中，為了達到製作高效率發光元件與克服晶體成長於不適合機板所產生的問題，首先我們利用原子層沉積技術建立一新穎的方法達成高品質氮化鋁鎵/氮化鎵多重量子井結構之成長。經由原子層沉積後之應變磊晶層可有效阻擋大多數從基板產生之線缺陷。並且插入原子層沉積磊晶層之氮化鎵系列發光二極體與一般發光二極體在操作電流為20mA 相比較下可提升 27% 之外部輸出功率。

我們同時也研究利用缺陷填補法來降低磊晶層缺陷密度。此缺陷填補法是利用化學蝕刻方式定義缺陷位置，將利用沉積二氧化矽薄膜填補蝕刻後的空洞，接者使用側向磊晶方式將其填補。此方法可以有效的降低磊晶層缺陷密度從單位面積 $1x10^9/cm^2$ 至 $4x10^7/cm^2$ 。在與一般發光二極體相比較之下，缺陷填補發光二極體可有效提升 45% 外部發光功率。

在另一方面，我們也提出倒金字塔結構位於氮化鎵與藍寶石積板介面製作高效率紫外光發光二極體，此倒金字塔結構可以同時有效提升

光萃取效率與磊晶層品質。在與一般發光二極體相比較之下，此結構之外部發光功率可有效提升 85%。除此之外，我們建立了首先利用機械式剝離法製作垂直式發光二極體。並且在拉曼光譜可以顯示氮化鎵磊晶層之應力在此倒金字塔結構中可以有效的被釋放。

最後，我們製作氮化鎵奈米柱結構應用於雷射操作上並討論其雷射特性。首先，利用氮化鎵磊晶層與奈米級鎳金屬遮罩進行蝕刻後形成氮化鎵奈米柱狀結構，接者利用再成長的方式重新成長新的晶格表面於奈米柱側壁。並且在光激發操作下，此結構之臨界條件為 122 MW/cm^2，雷射發光波長與發光半寬度分別為 363 nm 與 0.38 nm。我們推測此激發的現象歸因於在氮化鎵奈米柱結構中所產生隨機雷射與同調反饋的現象所致。

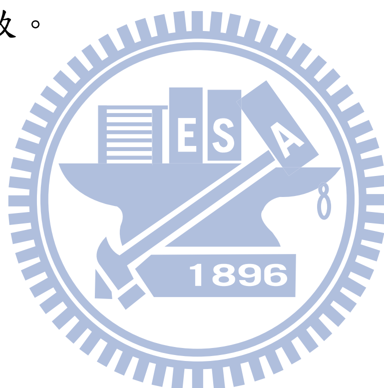

Growth and fabrication of high efficiency GaN based light emitting devices

Student: Ming-Hua Lo Advisor: Dr. Shing-Chung Wang

Dr. Hao-Chung Kuo

Institute of Electro-Optical Engineering

National Chiao Tung University

Abstract

Recently, GaN-based wide bandgap semiconductors are very important material system for fabrication of light emitting devices in a wide range of wavelength. The GaN-based laser diodes and light emitting diodes have been widely used in many areas, such as optical storage, backlight in liquid crystal displays, traffic signal and solid state lighting.

In this study, in order to achieve high efficiency light emitting devices and overcome the epitaxial issues on foreign substrate, we demonstrated a novel approach for high quality $Al_xGa_{1-x}N/GaN$ multiple quantum well epitaxy using atomic layer deposition (ALD) technique. The strain ALD layers effectively block a majority of threading dislocation from the substrate. The light output power for the GaN-based LED with an ALD insert layer at 20 mA was 27% higher than that for a conventional GaN-based LED structure.

We also study the defect selective passivation method to block the propagation of threading dislocations. The defect selective passivation is done by using defect selective chemical etching to locate defect sites, followed by silicon oxide passivation of the etched pits, and epitaxial over growth. The threading dislocation density in the regrown epi-layer is

significantly improved from $1x10^9$ to $4x10^7$ cm^{-2}. The output power of DP-LED is enhanced by 45% at 20 mA compared to a conventional LED.

On other hand, we also proposed the fabrication of high efficiency UV light emitting diodes with inverted pyramid (IP) structures at GaN-sapphire interface. The pyramid structures have significantly enhanced the light extraction efficiency and at the same time also improved the crystal quality. The output power was enhanced by 85% compared to a conventional LED. In addition, we demonstrated the first mechanical lift-off technique for fabrication of vertical type LED with IP structure. Raman spectroscopy analysis revealed that the compressive strain of GaN epilayer effectively relaxed in the IP structures.

Finally, the GaN based nanopillars structure for laser operation has been also fabricated and the laser behaviors were also been studied. The nanopillars were fabricated from a GaN epitaxial wafer by self-assembled Ni nanomasked etching, followed by epitaxial regrowth to form crystalline facets on the etched pillars. The lasing action occurs at threshold pumping power density of 122 MW/cm^2 with a linewidth of 0.38 nm at 363 nm. The lasing phenomenon could to due to random laser action with coherent feedback in GaN nanopillars.

致謝

時間總是過得很快，一轉眼四年的博士班生涯就結束了。也許這是一個結束，但也是另外一個新的開始。在這求學的階段裡，在學業上我學會如何自主學習，解決問題，思考創新，更學習接受挫折與失敗。在人際上，我也了解到互相合作，以及團隊的重要性，更了解到能力越強時態度要更謙卑。不論在各方面，我都成長了，這不是一個人的功勞而是在我周遭身邊的人深深地影響著我人生的態度。在這裡由衷的感謝這一群人。

首先非常感謝王興宗老師，沒有王老師我今天就不可能順利拿到博士學位，因為他的鼓勵與支持，讓我放棄了休學的念頭，更感謝他願意當我的指導教授。我在王老師身上學到的不僅僅只有學術上的態度，還有人生的價值觀。我也將它當作我的好朋友，因此這亦師亦友的關係將永久保存在我心裡。此外在此非常感謝郭老師帶領我進實驗室，給我非常多的研究資源與機會讓我有今天的成就。也感謝郭老師耐心的教導，我在未來的工作與表現上不會讓您失望。此外還有中研院的程博，她雖然不是我正式的指導教授，但是沒有他也不可能有今天的我，感謝他能接受我放蕩不羈的態度，並讓我一步一步的循序漸進做好研究。我也很樂於向他學習。

我最常說的一句話，實驗室就像一個家，大家都是一家人。實驗室裡有一位最好的姊姊，麗君。她對實驗室大家都很好，她很照顧我，感謝她四年的照顧。在我的研究生涯裡遇到了非常多優秀又可愛的碩士班學弟妹。感謝金門的高粱酒讓我酒量大增，潤琪，小恬恬，伯駿，我沒有很厲害但是我只是把我懂得都教給妳/你們，董ㄟ沒日沒夜做實驗和修機器，小柯的實驗上的贊助與沒事聊天很開心，小馬給的鼓勵與支持，玫君在中研院的幫忙，依嚀共同完成我最後的高難度論文，治凱，阿翔，阿菲，小新, JoJo 實驗上的大力幫忙，非常感謝他們的幫助與互相激勵，才有今天的成就。更感謝博士班學弟，柏孝沒事就一起出國八卦，鏡學的互相鼓勵與打氣，我相信你一定行的。感謝信助，板弟，大為，家揚就因

為有了以上這些好朋友在我的念書生涯中多添了更多的色彩。也感謝我的同學，士偉，清華，俊榮，碩均，小賴，宗鼎這些人都是鼓勵我畢業的動力，你們都很強，更感謝再一起出遊的日子很開心，還有感謝鎮宇學長感謝他的包容與幫忙才有我的成就。希望在未來可以一起打拼。

此外更感激在中研院研究時期的各位夥伴，博閔真的很厲害讓我學會很多知識，還有許博認真的態度，還有張校長實驗室的哲榮和他學弟妹都給我很大的幫忙。在生活上非常感謝，張博，小安和秀宇，他們最常聽我發牢騷，但是都會我很大的鼓勵與支持謝謝你們。

最後我要感謝我的家人，尤其是我父親。他無私的付出讓我奮發向上，我最想跟他說，我做到了，這次沒有讓您失望。還有最重要的一個人就是陪伴我九年的女友雪芹，她不僅犧牲了她的青春年華在等待與支持我念完博士班，也一直鼓勵與包容我，感謝妳，如果沒有認識妳我沒有今天。

明華
2010/10/13
交大光電所

Contents

Abstract (in Chinese) I
Abstract III
Acknowledgement V
Contents VII
List of tables X
List of figures XI

Chapter 1 Introduction 1
1.1 Background 1
1.2 GaN based material and its application for light emitting devices 2
1.3 An Overview of thesis 3
References 6
Chapter 2 Mechanisms, Fabrication Process and Measurement system 8
2.1 The physical mechanisms for light emitting diode 8
2.1.1 Internal quantum efficiency & Non-radiative recombination center 8
2.1.2 The limits of light extraction efficiency 10
2.2 Key issues for realizing high efficiency LEDs 12
2.2.1 Quality issues of GaN epitaxial layers 12
2.2.2 Light extraction of GaN LEDs 13
2.3 Metal Organic Chemical Vapor Deposition System 14
2.3.1 Reaction Equations 15
2.3.2 In-Situ Reflectance Monitoring During III-Nitrides Growth 18
2.4 Etching process in molten KOH 20
2.5 Micro photoluminescence spectroscopy (μ-PL) 21
2.5.1 Pumping power density and spotsize calculation 22
References 40
Chapter 3 Growth and fabrication of high quality atomic layer deposition GaN light emitting devices 42
3.1 The progress of AlGaN/GaN Multiple Quantum Well 42
3.2 The principle of Atomic Layer Deposition 43
3.3 The Fabrication of ALD AlGaN/GaN MQWs 44

3.4 Characteristic of AlGaN/GaN MQWs with ALD grown AlGaN Barriers.....44
3.5 Fabrication of near UV LED with ALD insert layer.....48
3.6 Performance of near UV LED with ALD insert layer.....49
References.....63

Chapter 4 Defect selective passivation in GaN epitaxial growth and its application to light emitting diodes.....65
4.1 The progress of low defect high quality GaN based light emitting devices..65
4.2 The Fabrication of defect passivation LED.....66
4.3 Characteristic of DP-LEDs.....67
References.....83

Chapter 5 High Efficiency light emitting diodes with Anisotropically Etched GaN-sapphire Interface and Mechanical Lift-off Technique.....85
5.1 High Efficiency light emitting diode with inverted pyramid structure.....85
5.1.1 The progress of high extraction efficiency GaN LEDs.....85
5.1.2 Fabrication of high efficiency light emitting diodes with inverted pyramid structure.....86
5.1.3 Characteristic of Inverted Pyramid LEDs.....87
5.1.4 Prediction of light extraction efficiency of IP-LED by ray trace simulation.....90
5.2 Vertical type thin GaN LED with hexagonal inverted pyramid by means of the mechanical lift-off.....91
5.2.1 The background of lift-off process in vertical type GaN LED.....91
5.2.2 Fabrication of vertical type LED with inverted pyramid structure.....92
5.2.3 Characteristic of thin GaN LED with IP structure.....94
References.....120

Chapter 6 Growth and Fabrication of GaN nanopillars.....123
6.1 The progress of low dimension GaN structure.....123
6.2 Fabrication of hexagonal GaN Nanopillars.....124
6.3 Characteristics of Optically Pumped Nitride-Based nanopillars.....125
6.4 Random lasing in GaN nanopillars.....125
References.....133

Chapter 7 Summary and Future Works.....134
7.1 Summary.....134
7.2 Future Works.....135

7.2.1 Fabrication and characterization of ultra-low dislocation density LED with Two-step Maskless defects passivation layers 135

Publication lists 138

Patent 141

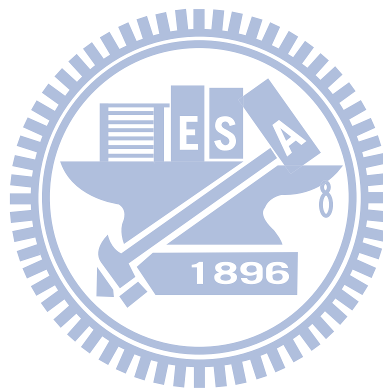

List of tables

Chapter 2

Table 2.1 All of etching method employed in recent years 25
Table 2.2 Comparison of calculation results and experimental results 26

Chapter 3

Table 3.1 Examples of thin film materials deposited by ALD including films deposited in epitaxial 51

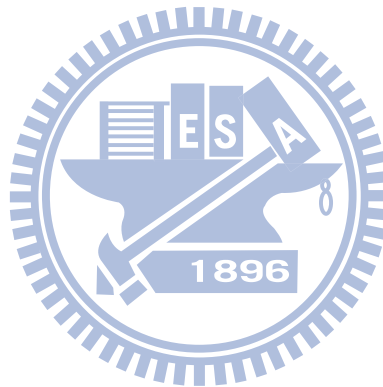

List of figures

Fig. 1.1 Lattice constant as a function of bandgap energy of III-N compounds 5
Fig. 2.1 Schematic analogy of carriers injected into active regions and depletion through radiative, nonradiative, and leakage recombinations 27
Fig. 2.2 Radiative and nonradiative recombination in active region. 28
Fig. 2.3 (a) Cross-section schematic diagram of typical LED structures (b) Photon trajectories inside the LED 29
Fig. 2.4 Total internal reflect in GaN-Based LED 30
Fig. 2.5 The angle of total internal reflection defines the light-escape cone 30
Fig. 2.6 (a) Cross section TEM image of typical GaN LED structure growth on sapphire substrate. (b) Enlarge TEM image of ten pairs multiple quantum well on GaN epitaxial layer. 31
Fig. 2.7 Some LED light extraction schemes. 32
Fig. 2.8 Schematic of in-situ monitoring configuration. 33
Fig. 2.9 The measured reflectivity of GaN bulk layer on sapphire. 34
Fig. 2.10 Illustration of different polarity, (a) GaN-face ($+c$ GaN, Ga-polarity) (b) N-face ($-c$ GaN, N-polarity) 35
Fig. 2.11 Schematic diagrams of the cross-section GaN film viewed along the $[\bar{1}\bar{1}20]$ direction for N-polar GaN to explain the mechanism of the polarity selective etching. (a) Nitrogen terminated layer with one negatively charged dangling bond on each nitrogen atom; (b) adsorption of hydroxide ions; (c) formation of oxides; (d) dissolving the oxides 36
Fig. 2.12 Nd:YVO4 355-nm pulsed laser microPL measurement system..................37
Fig. 2.13 (a) Knife Edge measurement diagram (b) the distance between lens and knife is 2 5μm,and laser beam spotsize is about 4.6μm 38
Fig. 2.14 Laser spotsize calculation and experimental results byknife edge measurement...39
Fig. 3.1 Schematic representation of an ALD process...52
Fig. 3.2 Growth procedure of AlGaN barrier and GaN well layers............................53
Fig. 3.3 High-resolution x-ray diffraction pattern at (0002) plane for the AlGaN/GaN MQWs sample 54

Fig. 3.4 RSM of the sample obtained from $(1 0 \bar{1} 5)$ diffraction 55
Fig. 3.5 Surface morphology of the grown AlGaN/GaN MQWs sample scanned by AFM 56
Fig. 3.6 Cross-sectional TEM image of the grown sample 57
Fig. 3.7 Plane-view TEM image of the AlGaN/GaN MQWs sample..........................58
Fig. 3.8 Enlarged cross-sectional TEM images of the sample...................................59
Fig. 3.9 The 13K and room temperature PL spectra of the AlGaN/GaN MQWs sample. Inset shows CL image taken at E = 3.71 eV. 60
Fig. 3.10 The schematic diagram of the two fabricated LEDs 61
Fig. 3.11 L-I-V characteristics of the two fabricated LEDs.......................................62
Fig. 4.1 Defect selective passivation process flow 73
Fig. 4.2 Top-view SEM image of the grown sample surface morphology after high temperature KOH etching process. 74
Fig. 4.3 Top-view SEM image of etched sample after deposit SiO2 film process. 75
Fig. 4.4 Top-view SEM image of etched sample with SiO_2 film morphology after CMP process...76
Fig. 4.5 TEM image of LED sample with defect selective passivation.......................77
Fig. 4.6 SEM image of the defect passivated sample after molten KOH etching 78
Fig. 4.7 SEM image of the defect passivated sample after high temperature H_3PO_4 etching 79
Fig. 4.8 Cross section CL (a) and SEM image (b) of the defect passivated epi-wafer under same magnification 80
Fig. 4.9 L-I and V-I curve of the DP-LED and R-LED 81
Fig. 4.10 The reverse voltage versus current characteristics of DP-LED and R-LED 82
Fig. 5.1 Process flowchart of LED with inverted pyramid structure..........................99
Fig. 5.2 SEM image of the etched GaN surface. The inverted pyramid structures can be seen from the over etched opening holes...100
Fig. 5.3 SEM cross section image of the regrown sample.......................................101
Fig. 5.4 A zoom out view of the inverted pyramid structures at GaN-sapphire interface 102
Fig. 5.5 X-ray diffraction rocking curves for IP-LED and R-LED samples 103
Fig. 5.6 Surface morphology of the UVLED with inverted pyramid scanned by AFM 104

Fig. 5.7 The schematic of the LED with inverted micro pyramid structures 105
Fig. 5.8 EL spectra of IP-LED and R-LED in normal direction...............................106
Fig. 5.9 L-I-V curves of IP-LED and R-LED..107
Fig. 5.10 The reverse voltage versus current characteristics of IP-LED and R-LED108
Fig. 5.11 Three-dimension far field patterns of IP-LED and R-LED 109
Fig. 5.12 Two-dimension far field pattern at 20 mA injection current (normal direction) 110
Fig. 5.13 Monte Carlo Ray tracing simulations. (a) and (b) are zoom in views at GaN-sapphire interface for IP-LED and R-LED.....................................111
Fig. 5.14 Light extraction enhancements versus different pyramid heights.............112
Fig. 5.15 The process flowchart for fabrication of thin GaN structure 113
Fig. 5.16 Cross-sectional SEM images of (a) IP structure formed in the wet etching process (b) The re-growth HIP GaN/air interface; Cross-sectional TEM images of (c) GaN-based LED structure grown on IP GaN/air template (d) The re-growth IP GaN/air boundary. The diffraction condition is g=(0002). 114
Fig. 5.17 Cross-sectional SEM image of the vertical LED structure after mechanical lift-off GaN LED/Silicon from sapphire substrate. Inset shows top-view SEM image of the IP surface morphology...115
Fig. 5.18 Surface morphology of the thin GaN LED structure after mechanical lift-off scanned by AFM...116
Fig. 5.19 Room temperature Raman spectrum of GaN epilayer regrowth on IP structure and mechanical lift-off by IP structure 117
Fig. 5.20 EL spectra of Ref-LED and V-LED in normal direction at 20mA. Inset shows peak wavelength shift of Ref-LED and V-LED 118
Fig. 5.21 L-I-V characteristics of the two fabricated LEDs 119
Fig. 6.1 (a)-(d) GaN nanopillars fabrication steps...128
Fig. 6.2 (a) Top view SEM image of Ni nano mask, (b) Tilted SEM image of GaN nanopillars before regrowth, (c) Top view SEM image of GaN nanopillars after regrowth, (d) Tilted SEM image of GaN nanopillars after regrowth and (e) cross section SEM image of GaN nanopillars after regrowth.......129
Fig. 6.3 Emission spectra of optically pumped GaN nanopillars 130
Fig. 6.4 Peak intensity and linewidth vs. pump intensity..131
Fig. 6.5 The schematic diagram showing the formation of a closed loop path for light

through recurrent scattering in GaN nanopillars 132
Fig. 7.1 The process flowchart for fabrication of two-step DP-LED 137

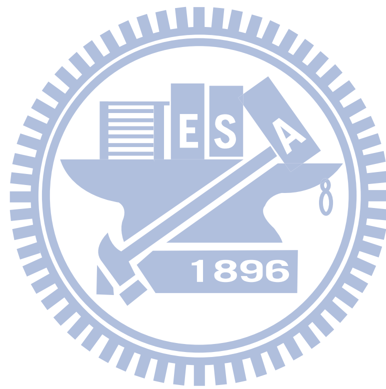

Chapter 1 Introduction

1.1 Background

Since the 1960s, many researchers studied the gallium nitride based materials and devices due to their wide direct bandgap and excellent thermal properties. However, owing the lack of GaN bulk growth methods, the GaN are often grown on foreign substrate such as sapphire or silicon carbide. It is difficult to grow high quality GaN film on these substrates for its applications to optoelectronic devices. In the 1967, the Maruska and Tietjen demonstrated the first large area single crystalline GaN thin films on sapphire substrate using chemical vapor deposition (CVD) approach [1]. In 1971, Pankove and Miller announced the first GaN blue light emitting diode at RCA laborites [2]. This device consists of an undoped n-type region, an insulating Zn-doped layer, and an indium surface metal contact [3]. However, the most of GaN based devices were still deposited on sapphire or SiC substrate using hydride vapor phase epitaxy (HVPE) system. The obstacles result from large lattice mismatch, thermal expansion coefficient mismatch and could not obtain the well conductivity at p-type GaN, which led to the GaN based LED development without eminent breakthrough. In 1986, Amano research group employed the MOCVD system to grow a thin AlN buffer layer at low temperature (LT) for decrease the dislocation density, which approach could obtain the mirror-like thin film [4]. In 1991, Nakamura used the LT GaN buffer layer could acquire the high crystal quality and mirror-like thin films as well [5]. In 1989, Akasaki (Amano et al.) was the first one used the low-energy electron-beam irradiation (LEEBI) to irradiate the suface of Mg doped gallium nitride then got p-GaN, which dopant concentration could reach to 10^{17} cm^{-3} and about 12 –cm sheet

resistance [6]. Nakamura technical group found that once the Mg doped gallium nitride under the high temperature and sufficient N_2 surroundings, then low sheet resistance *p*-GaN could be obtained [7]. The nitride-based compound semiconductor rapidly developed in past decade.

1.2 GaN based material and its application for light emitting devices

GaN-based wide bandgap semiconductors are very important material system for fabrication of photon emitters in a wide range of wavelength. Therefore, wurtzitic polytypes of GaN, AlN, and InN, and their ternary and quaternary alloys have attracted a great deal of attention (LEDs) and laser diodes (LDs) [8-10]. Since wurtzite polytypes of III-nitrides form a continuous alloy system whose direct bandgap ranging from 0.7 eV for InN [11], to 3.4 eV for GaN, and to 6.2 eV for AlN [12] as shown in Fig. 1.1. In addition, the III-nitrides are superior materials for high-temperature and high-power applications. [13-15].

Nitride-based green and blue LEDs with efficiency, brightness, and longevity that are well in excess of those required for outdoor applications are already commercially available. In addition, blue LEDs are employed to pump integrated inorganic and organic media to produce colors reaching red, on the one hand, and white light on the other. In addition to the traditional displays, these LEDs have applications in traffic lights, moving signs, indicator lights, spot lights, and possibly light sources for accelerated photosynthesis, and medicine for diagnosis and treatment. Potentially, further improvement in LEDs would expand the applications to lighting with large energy savings, as LEDs are more efficient than incandescent bulbs.

1.3 An Overview of thesis

This thesis is divided into the seven parts. The first part of this thesis briefly reviews the major development of GaN light emitting devices.

In Chapter 2, we introduce the fundamental physical-mechanisms of LED science to define and judge LED performances. The current challenges for realizing the high efficiency LED are also discussed in this chapter, including reduction of dislocation density in GaN epitaxial layers and improvement of light extraction efficiency by several geometric pattern structures. We also show fabricated process systems which include metal organic chemicals vapor deposition system, chemicals wet etching process in GaN epitaxial layers and optical measurement system.

In Chapter 3, we present a novel approach of reducing propagation of threading dislocations into active region and growth of high quality AlGaN/GaN multiple quantum structure using atomic layer deposition (ALD). The crystalline quality of as-grown sample is characterized by atomic force microscope (AFM), transmission electron microscopy (TEM) and x-ray diffraction (XRD). The device performances of LED with ALD insert layer are also shown in this chapter.

In Chapter 4, we investigate the fabrication process of defect passivation LEDs (DP-LEDs). The defect selective passivation is done by using defect selective chemical etching to locate defect sites, followed by silicon oxide passivation of the etched pits, and epitaxial over growth characteristics of the DP-LEDs are shown and studied.

In Chapter 5, by combing the chemical wet etching process and lateral overgrowth methods, we fabricate the high efficiency LED with inverted pyramid (IP) structure between GaN and sapphire interface. Characteristics of the IP-LEDs are shown and studied. We also build the light prorogation modeling in IP-LED by the Monte Carlo ray tracing

methods. Then, a process technique to fabricate the vertical type LED with IP structure by mechanical lift-off and wafer bonding process are proposed and demonstrated experimentally.

In the chapter 6, we report the fabrication of GaN nanopillars and their lasing characteristics under optical pumping at room temperature. The nanopillars were fabricated from a GaN epitaxial wafer by self-assembled Ni nanomasked etching, followed by epitaxial regrowth to form crystalline facets on the etched nanopillars.

Finally, a conclusion and a brief description in the future works are presented.

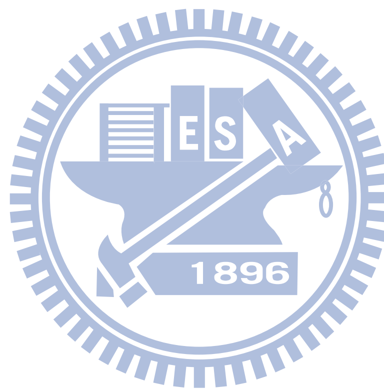

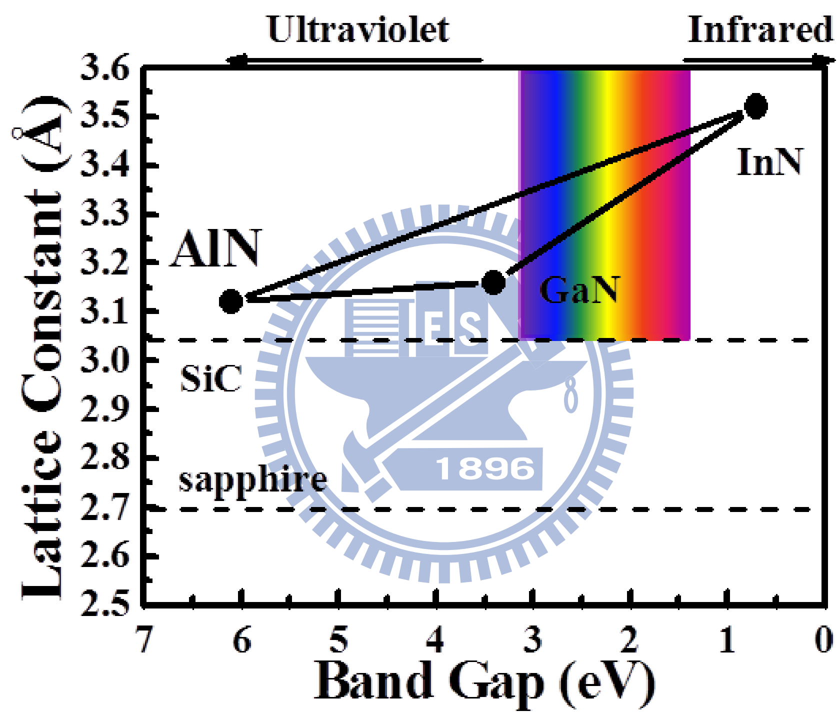

Fig. 1.1 Lattice constant as a function of bandgap energy of III-N compounds

References

[1] H.P. maruska and J. J. Tietjen, Appl. Phys. Lett. **15**, 367 (1969)

[2] J. I. Pankove, E. A. Miller and J. E. Berleyhesier, RCA Rev. **32**, 283 (1971).

[3] J.I. Pankove, E.A. Miller, D. Richman and J.E. Ber keyheiser, J. Lumin. **4**, 63 (1971)

[4] H. Amano, N. Sawaki, I. Akasaki and T. Yoyoda, Appl. Phys. Lett. **48**, 353 (1986).

[5] S. Nakamura, Jpn. J. Appl. Phys. **30**, L1705 (1991).

[6] H. Amano, M. Kito, K. Hiramatsu and I. Akasaki, Jpn. J. Appl. Phys. **28**, L2112 (1989).

[7] S. Nakamura, M. Senoh and T. Mukai, Jpn. J. Appl. Phys. **30**, L1708 (1991).

[8] S. Nakamura, T. Mukai, and M. Senoh, Appl. Phys. Lett. **64**, 1687 (1994).

[9] S. Nakamura, M. Senoh, N. Iwasa, and S. Nagahama, Jpn. J. Appl. Phys. **34**, L797 (1995).

[10] G. Y. Xu, A. Salvador, W. Kim, Z. Fan, C. Lu, H. Tang, H. Markoc, G. Smith, M. Estes, B. Goldberg, W. Yank, and S. Krishnankutty, Appl. Phys. Lett. **71**, 2154 (1997).

[11] T. Matsuoka, H. Okamoto, M. Nakao, H. Harima, and E. Kurimoto, Appl. Phys. Lett. **81**, 1246 (2002).

[12] L. J. Schowalter, G. A. Slack, J. B. Whitlock, K. Morgan, S. B. Schujman, B. Raghothamachar, M. Dudley, and K. R. Evans, Phys. Stat. Sol. (c) 0, No. **7**, 1997 (2003).

[13] T. G. Zhu, D. J. H. Lambert, B. S. Shelton, M. N. Wong, U. Chowdhury, H. K. Kwon, and R. D. Dupuis, Electron Lett. **36**, 1971

(2000).
[14] B. S. Shelton, D. J. H. Lambert, H. J. Jang, M. M. Wong, U. Chowdhury, Z. T. Gang, H. K. Kwon, Z. Liliental-Weber, M. Benarama, M. Feng, and R. D. Dupuis, IEEE Trans Electron Devices **48**, 490 (2001).
[15] A. P. Zhang, J. Han, F. Ren, K. E. Waldrio, C. R. Abernathy, B. Luo, G. Dang, J. W. Johnson, K. P. Lee, and S. J. Pearton, Electronchem. Solid-State Lett. **4**, G39 (2001).

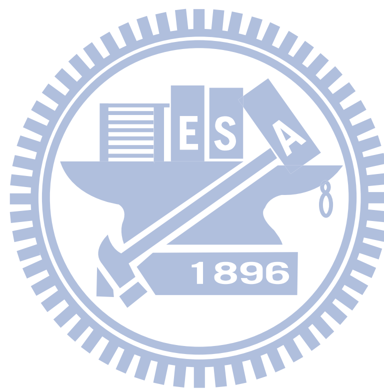

Chapter 2 Mechanisms, Fabrication Process and Measurement system

2.1 The physical mechanisms for light emitting diode

2.1.1 Internal quantum efficiency & Non-radiative recombination center

For the double heterostructure active region, the injected current provides a generation term and various radiative and nonradiative recombination processes as well as carrier leakage provides recombination term. The process of a certain steady-state carrier density in the active region could be compared to that a reservoir analogy, which is being simultaneously filled and drained, as shown in Fig. 2.1. In Fig. 2.1, there are $\eta_i = (\frac{I}{eV})$ electrons per second per unit volume being injected into the active region. The η_i , is the fraction of terminal current that generates carriers in the active region and V is the volume of the active region.

Thus, rate equation is determined as

$$\frac{\mathrm{dn}}{\mathrm{dt}} = G_{gen} - R_{rec} \quad (2\text{-}1)$$

where G_{gen} is the rate of injected electrons and R_{rec} is the rate of recombining electrons per unit volume in the active region. The recombination process is accompanied with spontaneous emission rate R_{sp}, nonradiative recombination rate, R_{nr}, and carrier leakage rate, R_l, as depicted in Fig. 2.1. Carrier leakage rate, R_l, is occurred when the transverse or lateral potential barriers are not sufficiently high. Thus total recombination rate is expressed as below

$$\mathrm{R_{rec}} = \mathrm{R_{sp}} + \mathrm{R_{nr}} + \mathrm{R_l} \quad (2\text{-}2)$$

It is common to describe the natural decay processes by a carrier lifetime, τ. In the absence of photon generation term, the rate equation for carrier decay is,

$$\frac{d_n}{d_t} = \frac{n}{\tau}, \text{ where } \frac{n}{\tau} = R_{sp} + R_{nr} + R_l \tag{2-3}$$

The carrier rate equation in equivalent be expressed as

$$\frac{dn}{dt} = G_{gen} - R_{rec} = \left(\frac{I}{eV}\right) - \frac{n}{\tau} \tag{2-4}$$

The spontaneous photon generation rate per unit volume is exactly equal to the spontaneous electron recombination rate, R_{sp}, since by definition every time an electron-hole pair recombines radiatively, a photon is generated. Under steady-state conditions (*dn/dt =0*), the generation rate equals the recombination rate,

$$\left(\frac{I}{eV}\right) = \frac{n}{\tau} = R_{sp} + R_{nr} + R_l \tag{2-5}$$

The spontaneously generated optical power, P_{sp}, is obtained by multiplying the number of photons generated per unit time per unit volume, R_{sp}, by the energy per photon, hν, and the volume of the active region V, Then

$$P_{sp} = h\nu \times V \times R_{sp} = \eta_i \eta_r \frac{h\nu}{e} I \tag{2-6}$$

where the radiative efficiency, η_r, is defined as

$$\eta_r = \frac{R_{sp}}{R_{sp}+R_{nr}+R_l} \tag{2-7}$$

Usually, the η_r depends upon the carrier density and the product of $\eta_i\eta_r$ is the internal quantum efficiency, η_{int}. Thus according to Eq (2-6), the internal quantum efficiency is defined as:

$$\eta_{int} = \frac{P_{sp}/(h\nu)}{I/e} = \eta_i \eta_r \quad (2\text{-}8)$$

Internal quantum efficiency:

$$IQE = \frac{\text{(the number of photons emitted from active region per secend)}}{\text{(the number of electrons injected into LED per secend)}} \quad (2\text{-}9)$$

Thus the internal quantum efficiency is related to η_i, the fraction of terminal current that generates carriers in the active region, and to η_r, the fraction of rates between radiative recombination to total carriers' recombination. According to Eq (2-8), we can enhance the internal quantum efficiency of LEDs by either increasing radiative recombination rate, R_{sp}, or decreasing nonradiative recombination rate, R_{nr}, and carrier leakage rate, R_l.

The possible recombinative paths of injected electrons and holes are shown in Fig. 2.2. Typically, material defects —including defects that extend over some distance of the material such as threading dislocations and more localized point defects such as vacancies and impurities — act as centers of nonradiative recombination. Thus the overall goal in this stage is to enhance the radiative recombination rate and suppress the nonradiative recombination rate. Therefore, significantly improvements of grown-layers quality associating with appropriate design of LEDs structures is the main thought to improve the internal quantum efficiency.

2.1.2 The limits of light extraction efficiency

A cross-section schematic diagram of typical LED structures is shown in Fig. 2.3 (a). The most serious problem with rectangular cubic may be that the photons generated at a point in the active region will be

trapped inside the GaN and sapphire region as shown in Fig. 2.3 (b), due to the continued total internal reflections off the chip wall as illustrated in Fig. 2.4. Assume that the angle of incidence in the semiconductor at the semiconductor- air interface is given by θ_1. Then the angle of incidence of the refracted ray, θ_2, can be derived from Snell's law

$$n_s \sin\theta_1 = n_a \sin\theta_2 \qquad (2\text{-}10)$$

Where, n_s and n_a are the refractive indices of semiconductor and air, respectively. The critical angle θ_c for total internal reflection is obtained using $\theta_2 = 90°$, using Snell's law, one obtains.

$$\sin\theta_c = \left(\frac{n_a}{n_s}\right)\sin 90^0 \,, \theta_c = \sin^{-1}\left(\frac{n_a}{n_s}\right) \qquad (2\text{-}11)$$

The angle of total internal reflection defines the light-escape cone as shown in Fig 2.5. Light emitted into the cone can escape from the semiconductor, whereas light emitted outside the cone is suffered from the total internal reflection. The surface area of the escape cone is given by the integral

$$\text{Area} = \int dA = \int_{\theta=0}^{\theta_c} 2\,\pi r \sin\theta_r \, d\theta = 2\pi r^2(1-\cos\theta_c) \qquad (2\text{-}12)$$

Assume that light is emitted from a point-like source in the semiconductor with a total power of P_{source}. Then the power that can escape from the semiconductor is given by

$$P_{escape} = P_{\text{source}} \frac{2\pi r^2(1-\cos\theta_c)}{4\pi r^2} \qquad (2\text{-}13)$$

Where $4\pi r^2$ is the entire surface area of the sphere with radius r. The calculation indicates that only a fraction of the light emitted inside a semiconductor can escape from the semiconductor. This fraction is given by

$$\eta_{ext} = \frac{P_{escape}}{P_{source}} = \frac{2\pi r^2 (1-\cos\theta_c)}{4\pi r^2} \quad (2\text{-}14)$$

Expanding Eq (2-14) into power series and neglecting higher than second-order terms yields

$$\eta_{ext} = \frac{1}{2}\left[1-\left(1-\frac{{\theta_c}^2}{2}\right)\right] = \frac{1}{4}{\theta_c}^2 \approx \frac{1}{4}\frac{n_a}{n_s}, n_a = 1, n_s = n_{GaN} = 2.45 \quad (2\text{-}15)$$

According to Eq (2-15), only a few percent (~4%) of the light generated in the semiconductor can escape from a planar LED.

2.2 Key issues for realizing high efficiency LEDs

2.2.1 Quality issues of GaN epitaxial layers

The GaN-Based material and devices are often epitaxially grown on foreign substrates, such as silicon carbon (SiC) or sapphire. These substrates must be used because wafers of GaN are not available as in the case of more common semiconductors. A layer grown at lower temperature, the nucleation layer, is used to initiate oriented growth on the substrate, followed by epitaxial growth on this layer at higher temperatures. The as grown GaN epitaxial layer has high threading dislocation density (TDD) typically in the range of $10^{8\text{-}10}$ cm^{-2} due to the mismatches in lattice constants (16%) and thermal expansion coefficients (39%) between GaN and sapphire, resulting in defect-mediated nonradiative recombination of electron-hole pairs and reduced mobility because of carriers trapped by defect centers. Fig. 2.6 (a) shows the cross section TEM image of typical GaN LED structure growth on sapphire substrate, the threading dislocation location density is higher than 10^9 cm^{-2} in GaN epitaxial layers and some threading dislocations propagate

through the active region of LED, as shown in Fig 2.6 (b). These threading densities need to be drastically reduced because dislocations quench light emission of LEDs. These dislocation defects can be reduced by substrate patterning techniques such as Epitaxial Lateral Overgrowth (ELOG) [1], or pattern sapphire substrate [2]; above approaches rely on spatial filtering, terminating, and turning of threading dislocations, so they do not reach the device active region. In the chapter 3 and 4 of this thesis, we report novel epitaxial approach and defect passivation structure to effectively block thread dislocation from the substrate to active region. In particular, defect passivation structure not only block the propagation of TD but also can act as light scattering sites to improve LED light extraction efficiency, similar to the use of patterned GaN-sapphire interface to reduce light trapped by total internal reflection.

2.2.2 Light extraction of GaN LEDs

Limitations in light extraction include total internal reflection at interfaces and light absorption within the device or in the packaging. The generation of light in active region of an LED is mostly captured with GaN and sapphire by the guided modes. It is due to the high contrast refractive index at the GaN (n=2.45)/air (n=1) and GaN/sapphire (n=1.78) interfaces, resulting in total internal reflection that traps light in the high index GaN and in the sapphire substrate. Some light-extraction methods are shown in Fig. 2.7 and discussed in following.

(a) Patterned sapphire substrate: Patterned sapphire substrate with chemical wet etching in between epitaxial growth steps has provided another way to improve light extraction efficiency. The light with large incident angle will be reflected coupling into escaping cone. However, some light still might travel multi-times and absorbed finally.

(b) Two-Dimensional (2D) Photonic Crystal

Photonic crystals can be used in multiple ways to increase light extraction efficiency. Two-dimensional (2D) photonic crystals can be used to scatter waveguided modes out of the active layer region. Another approach is to use 2D photonic crystals to change the photonic density of states in the active layer so that no in-plane modes are permitted [3]. This would cause all emitted light from the quantum wells to be normal to the LED surface so that it would lie within the escape cone and not be reflected. A third possibility is to increase the internal quantum efficiency by enhancing the photonic density of states at the LED emission wavelength. These fabrication processes often involves micro lithography and etching.

In the chapter 5 of this thesis, we report high extraction efficiency LED with inverted pyramid structure at the GaN-sapphire interface without complex lithography process. Form Monte Carlo simulation and experiment results, the IP structure can efficiently redirect the propagation of the laterally guided modes to the surface normal direction. The proposed method not only can improve the light extraction efficiency but also provide a sacrificial layer for substrate lift-off technique.

2.3 Metal Organic Chemical Vapor Deposition System

For the past twenty years, metal organic chemical vapor deposition (MOCVD) systemhas become a commonly used technology for production of III-V compound semiconductor optoelectronic and electronic devices. The term “MOCVD” was originated by Manasevit [4-6], and it was used to express a form of chemical vapor deposition (CVD) utilizing the new process transported metals using organic compounds for one or more of the precursors. Alternative names included OM (OrganoMetallic) CVD, MOVPE (Vapor Phase Epitaxy), and OMVPE are all the same meaning, except epitaxy is a special case of thin

film deposition where the layer replicates the crystal structure of the substrate. Because of the improvement in the material quality produced by MOCVD, many important III-V devices have become commercially viable. Indeed, the achievement of growing ultra-bright blue light emitting diodes by MOCVD [7] makes this technology be a leading candidate for manufacturing optoelectronics devices. In this dissertation, we use MOCVD system to grow all the epitaxial structures. The detailed descriptions and specific functions of MOCVD system are given in this chapter.

2.3.1 Reaction Equations

The MOCVD process for the growth of compound semiconductor materials and devices originated in the pioneering work has been done by H. M. Manasevit. Briefly, MOCVD process relies on vapor transport of the group III alkyls combined with group V hydrides into heated substrate. At the heated substrate, the molecules pyrolyze to produce the group III and group V elements needed for formation of desired III-V semiconductors and subsequent reaction. The simplest case in MOCVD [8] involves a pyrolysis reaction of the vapor of a volatile organometallic compound and a gaseous hydride, given by:

$$R_nA + DH_n \rightarrow AD + nRH \qquad (2\text{-}16)$$

A and D are the constituent species for the deposited solid. R is an organic radical ofsome unspecified form, and many organometallic compounds have been studied as sources for the MOCVD processes. However, the lower order organic radicals are generally used, such as a methyl- or ethyl-radical, and the most important are trimethylgallium (TMGa), triethylgallium (TEGa), trimethylaluminum (TMAl), and trimethylindium (TMIn). Desirable properties include a reasonable vapor pressure at room temperature or below, high purity, low cost, a low

affinity for oxygen and water vapor, and low toxicity. Unfortunately, many of the MOs that meet the vapor pressure and purity needs best are also highly reactive with oxygen. They are therefore contained in stainless steel bubblers, and great effort is made to avoid their contamination by air. Contrasting with V sources, metalorganic group III source are either liquids, such as TMGa, TEGa, and TMAl, or solids such as TMIn. Therefore, the organmetallic constituents generally are transported to a heated substrate by passing a carrier gas, over or through the compound contained in a constant-temperature bubble vessel. Highly purified hydrogen or nitrogen is bubbled through the liquid to transport the material into the reactor. Knowledge of the vapor pressure (at the bubble temperature and pressure) and the carrier gas flow rate is sufficient to determine the transport rate. On the other hand, most MOCVD growth of III-V compound semiconductors and alloys involves the use of hydrides, such as arsine, phosphine, or ammonia for the column V species. In principle, these are the simplest of column V sources to use because they are already gaseous and supplied from simple cylinder-based delivery system. In spite of the fact that they are extremely toxic, since they are relatively inexpensive with high purity layers. The dopants processes are available in the form of MOs in bubblers (for example, Cp2Mg), or in the form of gases (for example, SiH4). Because of the concentration may be varied over a wide range, the dopant sources have to adjust the concentration, typically with a dilution network. The growth of semiconductor alloys by MOCVD is easily accomplished by mixing the vapors from the different alloy constituents in the appropriate vapor phase ratio to form the desired composition. A general equation for a ternary alloy is given by:

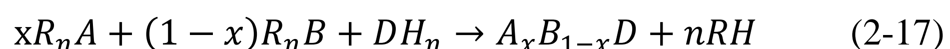

$$\mathrm{x}R_nA + (1-x)R_nB + DH_n \rightarrow A_xB_{1-x}D + nRH \qquad (2\text{-}17)$$

For GaN-based material growth, the first MOCVD system design for GaN growth was developed by Maruska and Tietjen [10]. Soon after, Manasevit applied this technique to grow GaN onto sapphire substrate [11]. The choice of sapphire substrate results from the facts that no GaN bulk substrate are available and a very stable material is required to deal with the high temperature required for GaN growth at around 1000°C. Based on the equation (2-16), the GaN epitaxy process by using MOCVD can bewritten:

$$(\mathrm{CH_3})_3Ga(v) + NH_3(v) \rightarrow GaN(s) + 3CH_4(v) \qquad (2\text{-}18)$$

which v is vapor and s is solid. This simple equation, however, ignores the complicated reaction path and reactive species in the reactor. The incoming materials partially decompose and are then adsorbed on the surface. Then, they decompose further or aredesorbed. The atoms and radicals move around on the surface with growth occurring at steps for smooth, two-dimensional layers, replicating the structure of the substrate [12]. In fact, the detail of the reaction is still unknown. Nishizawa, Abe and Kurabayashi (1985); Denbaars et al. (1996) [13] reported a reaction pathway arise form growing GaAs epitaxial layers involves homogenerous decomposition of TMGa :

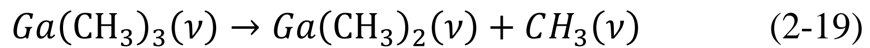

$$Ga(\mathrm{CH_3})_3(v) \rightarrow Ga(\mathrm{CH_3})_2(v) + CH_3(v) \qquad (2\text{-}19)$$

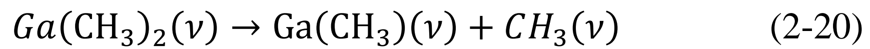

$$Ga(\mathrm{CH_3})_2(v) \rightarrow \mathrm{Ga}(\mathrm{CH_3})(v) + CH_3(v) \qquad (2\text{-}20)$$

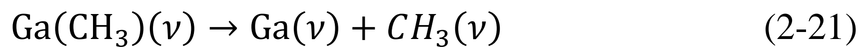

$$\mathrm{Ga}(\mathrm{CH_3})(v) \rightarrow \mathrm{Ga}(v) + CH_3(v) \qquad (2\text{-}21)$$

In the other hand, the group V source, NH3, is considered to decompose heterogeneously on the GaN surface or reactor wall to provide atomic nitrogen, or a nitrogen containing radical at high grow temperature.

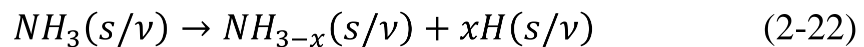

$$NH_3(s/v) \rightarrow NH_{3-x}(s/v) + xH(s/v) \qquad (2\text{-}22)$$

Combine the above mentioned equation, one possible growth mechanism

of GaN that occur at the solid/vapor interface could be expressed as follows:

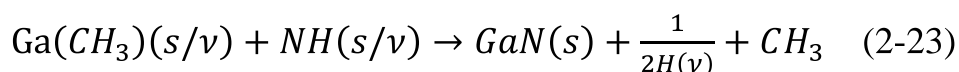

$$\mathrm{Ga}(CH_3)(s/v) + NH(s/v) \rightarrow GaN(s) + \frac{1}{2H(v)} + CH_3 \quad (2\text{-}23)$$

Although the growth mechanism of GaN can be briefly expressed by Eq. (2-23). The most difficult topic is the kinetics of the process and growth mechanism occurring at solid/vapor interface during MOCVD growth.

Optimization of MOCVD grown condition is typically done by empirical studies of external parameters such as grown temperature, V/III ratio, and mass flow rate. These studies have identified three regions of growth: mass transport limited, desorption and surface kinetically limited regimes. Conventional GaN MOCVD growth is usually performed in mass transport limited regime that takes place over a wide temperature (600~1100°C), and the growth is limited by mass transport of the column III reactant to the growing interface.

2.3.2 In-Situ Reflectance Monitoring During III-Nitrides Growth

For many years, high vacuum growth techniques such as MBE have enjoyed the advantage of using in situ diagnostic tools such as RHEED to determine substrate surface conditions and measure growth rates. Now MOCVD has responded with a variety of optical techniques to perform diagnostic on the layers as they grow [14]. Indeed, the in-situ monitoring of optical techniques is very useful for growing optoelectronic devices such as VCSELs due to the stringent requirement of phase matching. The in-situ monitoring is also an important tool to grow III-Nitride materials on foreign substrate, such as sapphire, because the limitation of homoepitaxial substrate absence is usually overcome by growing a low-temperature (LT) AlN [15] or GaN [16] nucleation layer on a sapphire substrate before the high-temperature (HT) growth. In order to

realize the growth information during growing GaN, the in-situ monitoring tool is usually used to extracting growth information. In our D-75 system, we use an in-situ normal incidence reflectance method to extract the information of growth rate and crystal quality. The tungsten-lamp reflectometry is applied as the in-situ monitoring in D-75 type MOCVD system. The schematic of the configuration is shown in Fig. 2.8. Two optical heads are mounted on the top flow flange of the reactor and monitoring the growth conditions for the upper and lower points of the wafer surface. An optical head couples two fibers; one is from the light source with the continue band wavelength, and the other is to the detector. Suppose the optic index of thin film materials is different from the substrate, the reflectance and interference from the underlying interface can be described as $R = |r|^2$, and r can be described as [17]

$$r(t) = \frac{r_\infty + r_i exp(-i4\pi\beta_2)}{1 + r_\infty r_i exp(-4\pi\beta_2)} \quad (2\text{-}24)$$

where $\beta_2 = 4\pi nd/\lambda$ is the phase shift in the film, r_∞ and r_i are the reflectance of an infinitely thick film of the top layer and the internal layer reflectance, respectively.

The $exp(-i4\pi\beta_2)$term describe and oscillatory behavior of β_2. Thus growth rate can be determined with the refractive index at certain growth temperature at a given wavelength. The growth rate can be obtained by

$$G_R = \lambda T_d / 2n_\lambda \quad (2\text{-}25)$$

where λ is the chosen wavelength, Td is the oscillation period of the reflectivity curve, n_λ is the refractive index of the epitaxial layer at the growth temperature for λ This is very useful controlling the thickness of the LT nucleation layer. Fig. 2.9 shows the example for the measured reflectivity of a GaN bulk structure. Furthermore, applying the in-situ monitoring system, we can also do temperature calibrations. In the former case, one can perform temperature calibration with eutectic wafers

(Al-coated Si wafers or Silver-coated Si wafers) quickly and easily by plotting the reflectance as a function of temperature, while the temperature of the reactor is ramped slowly. As the temperature ramping up to the melting point of aluminum or silver, 660°C, and 961°C, respectively, the reflectance would be drop down rapidly. Thus one could know the meter temperature is the metal melting point. In the latter case, one can design a "calibration" structure that contains layers of different compositions or different growth condition in a single growth run without requiring any post growth characterization.

2.4 Etching process in molten KOH

The discrepancy of etching characteristics in Ga-face ($+c$ GaN, Ga-polarity) and N-face ($-c$ GaN, N-polarity) has been specifically investigated as illustrated in Fig. 2.10. Some reports showed that gallium nitride could be etched in the aqueous sodium hydroxide (NaOH) solution but etching ceased when the formation of an insoluble coating of presumably gallium hydroxide ($Ga(OH)_3$) [18, 19]. For further etching, it would need removing of the coating by continual jet action. All other various aqueous acid and base solutions have been tested for etching of GaN at temperature up to 75°C were listed in Table 2.1 [20-22]. The undetermined etch rate (nm/min) was because it various from sample to sample and differences in the defect density. According to the research reports in recent years; the common cognition related to gallium nitride etching process was that the most of gallium nitride could be etched rapidly in N-face. The reason for the face-dependent gallium nitride etching process has been studied by Li et al., who utilized the X-ray photoelectron spectroscopy (XPS) to examine the surface chemistries before and after etching process in aqueous KOH solutions for both Ga- and N-face gallium nitrides. The conclusion is that the different etching

results in Ga- and N-face gallium nitride crystals are due to the different states of surface bonding. Besides, the most important is the etching process only dependent on the polarities, not on the surface morphology, growth condition and which atoms form the surface termination layer. The GaN chemical etching reaction with KOH could be described as the following formula [23]：

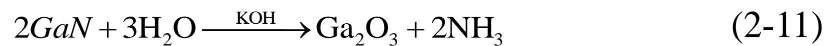

$$2GaN + 3H_2O \xrightarrow{KOH} Ga_2O_3 + 2NH_3 \quad (2\text{-}11)$$

Here, the molten KOH act as a catalyst and a solvent for the resulting Ga_2O_3 (Fig. 2.11 (d)) as well. The mechanism about etching N-face gallium nitride substrate was illustrated in Fig. 2.11 The hydroxide ions (OH^-) were first adsorbed on the gallium nitride surface (Fig. 2.11 (b)) and finally react with Ga atoms once the OH^- ions with sufficient kinetic energy as shown in the Fig. 2.11 (c). The etching could be started at step (c) if the surface was Ga-terminated. The inertness of Ga-face GaN was ascribed to the hydroxide ions would be repelled by the negatively-charged triple dangling bonds of nitrogen near the surface. Thus, if the Ga-face GaN was Ga-terminated, the etching process stops after the first gallium atom layer was removed. In contrast, the N-face GaN, every nitrogen atom with single dangling bond to prevent the hydroxide ions attacking from Ga atoms.

2.5 Micro photoluminescence spectroscopy (μ-PL)

Photoluminescence (PL) spectroscopy has been used as a measurement method to detect the optical properties of the materials because of its nondestructive characteristics. PL is the emission of light from a material under optical excitation. Reducing the laser beam spotsize to micrometer by beam expanders and objective lens is the so-called μ-PL. The laser light source used to excite carriers should have larger energy band gap than the semiconductors. When the laser light is

absorbed within the semiconductors, it would excite the carriers from the valence band to the conduction band. Then, it produces the electrons in the conduction band and the holes in the valence band. When the electron in an excited state return to the initial state, it will emit a photon whose energy is equal to the energy difference between the excited state and the initial state, therefore, we can observed the emission peak from PL spectrum. The schematic setup of our μ-PL system is shown in Fig. 2.12 The pumping source is Nd:YAG 355 pulsed laser with a pulse width of ~1nsec at a repetition rate of 1KHz.The PL is collected by a 15X objective lens and straightly collected by spectrometer with a charge-coupled device (Jobin-Yvon IHR320 Spectrometer) or collected by a fiber with 200μm core, which rotating in the normal plane of the sample, and also coupled into spectrometer. The spectral resolution is about 0.1 nm for spectral output measurement. We can also monitor the image and spatial distribution on the sample surface by charge-coupled device (CCD) and beam view, respectively.

2.5.1 Pumping power density and spotsize calculation

The optical pumping of the samples was performed using frequency-tripled Nd:YVO4 355-nm pulsed laser with a pulse width of 1ns at a repetition rate of 1 kHz. The microPL measurement system was shown in Fig 2.12 It is often necessary to calculate the power density (Power/Area) of a laser beam (for example, when trying to determine whether a beam will damage an optic or detector).Power density is expressed in watts per square meter (W/m^2) or milliwatts per square centimeter (mW/cm^2). Usually power density is more often expressed in terms of W/cm^2 when making surveys. In our experiments, the pumping power density can be presented by following equation

$$\text{Power Density} = \frac{P_{average} \times \frac{1m\sec}{1n\sec} \times 0.3 \times \alpha}{\pi (M^2 R)^2} \quad (2\text{-}26)$$

where $P_{average}$ is the laser optic power measured by power detector, 0.3 is the value of calibration when passing through the 15X objective lens. And,α (=0.85) is the absorption coefficient of the GaN, R is the radius of the laser beam in centimeters.M^2(=1.3) is defined as the ratio of the waist-diameter-divergence product, $2W_m \cdot 2\theta_m$ (usually measured in units of mm・rad),to that expected for a Gaussian beam. Specification of laser shows the full angle is 3mrad,beam waist location is -135mm and M^2 is 1.3, so that initially spotsize which is 75.37μm can be obtained by using equation 2-27

$$\omega_0 = \frac{\lambda}{\pi\theta} \quad (2\text{-}27)$$

The distance between laser and objective lens is about 121.7cm, according to equation 2-26 and 2-27, spotsize expands to 1.83mm , then be focused to 0.8μm by a 15X objective lens which focal length was 13mm by using equation 2-27

$$Z_0 = \frac{\pi \omega_0^{\ 2}}{\lambda} \quad (2\text{-}28)$$

$$\omega_1 = \omega_0 \times \sqrt{1 + \left(\frac{Z}{Z_0}\right)^2} \quad (2\text{-}29)$$

$$\omega_2 = \frac{\lambda f}{\pi \omega_1} \quad (2\text{-}30)$$

In other words, the theoretical model of laser beam spotsize calculation results indicated that the value of beam radius is 0.8μm, Rayleigh range is 5.73μm and the diverge half-angle is 0.14 rad after going through 15X objective lens.

In order to know the real beam raidus, we use Knife Edge experiment

to measure Nd:YVO4 355nm pulsed laser. Under a fixed excited power, we can get the relationship of normalized intensity vs. distance that the knife moved, as shown in Fig. 2.13(a). The distance between 10% and 90% of full scale needs to multiple a factors of 0.78125, and the value is the called pumping spotsize. We have presented some knife edge results obtained on measurements of various Z axis value. For example, when moving knife away from the objective lens focal point about Z=25μm, the spotsize will be attained 4.6um as shown in Fig. 2.13(b). Vary objective lens distance Z from -125μm to 325μm, then we can obtained Gaussian beam curves of the laser, and its diverge half-angle is 0.147 rad. The calculation of Nd:YVO4 pulsed laser beam spotsize is very similar to our experimental results. The comparison between calculation results and experimental results as shown in Fig. 2.14 and Table 2.2

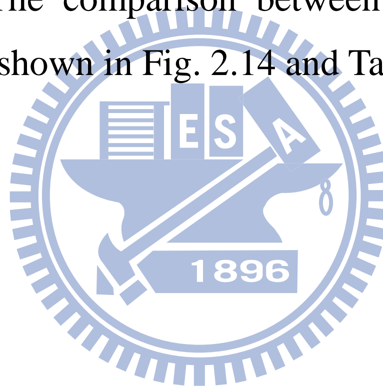

Etching solutions	GaN etch temperature
Citric acid	75°C
Succinic acid	75°C
Oxalic acids	75°C
Nitric acid	85°C
Phosphoric acid	82°C
Hydrochloric acid	80°C
Sulfuric acid	82°C
Potassium triphosphate	75°C
Nitric acid/potassium triphosphate	75°C
Hydrochloric acid/potassium triphosphate	75°C
Boric acid	75°C
Nitric/boric acid	75°C
Potassium tetra borate	75°C
Sodium tetra borate	75°C
Potassium triphosphate	75°C

Table 2.1 All of etching method employed in recent years

	W_0 (μm)	Θ(rad)	Z_R (μm)
Theory	0.8	0.141	5.73
Experiment	1.75	0.147	27.35

Table 2.2 Comparison of calculation results and experimental results

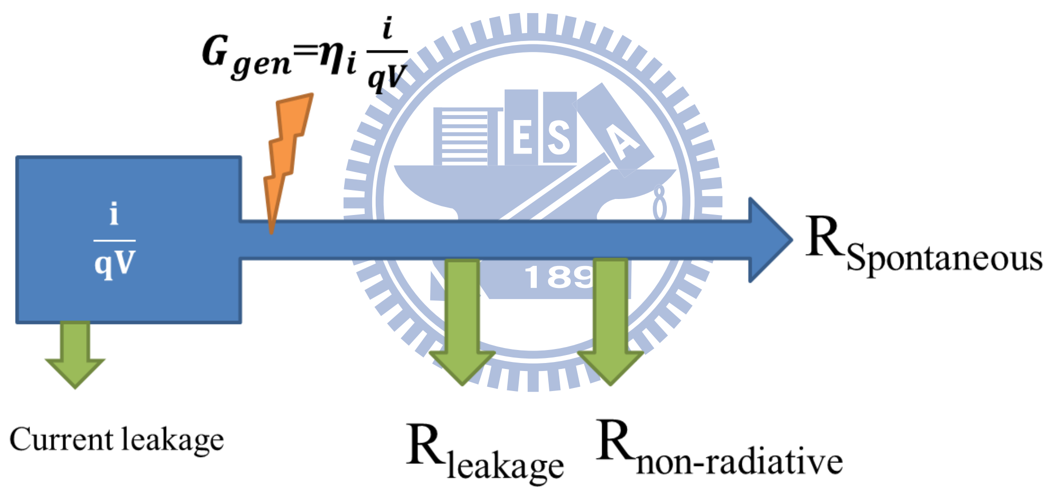

Fig. 2.1 Schematic analogy of carriers injected into active regions and depletion through radiative, nonradiative, and leakage recombinations

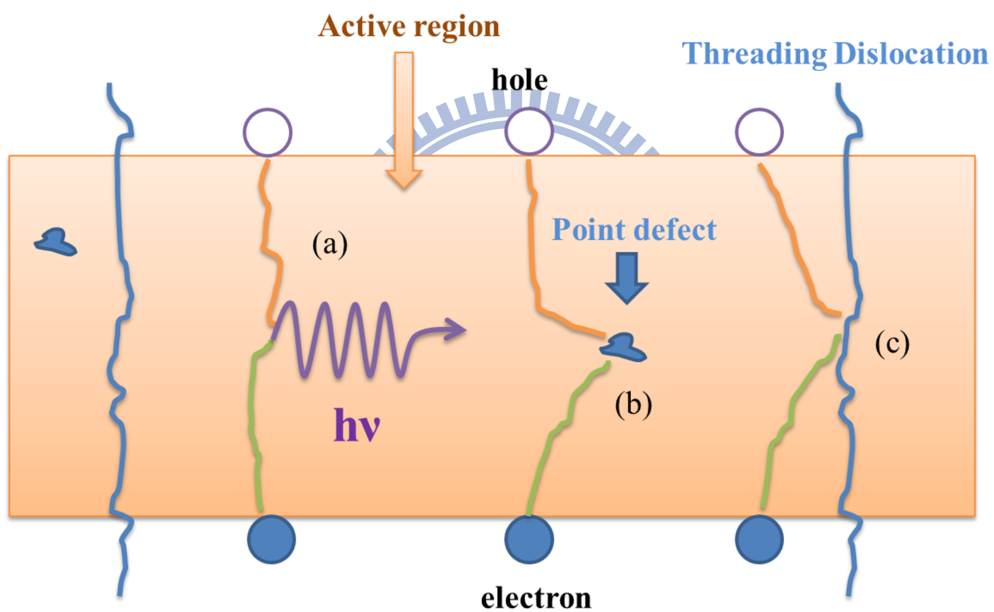

(a) : Radiative Path
(b) and (c): Non-radiative Path

Fig. 2.2 Radiative and nonradiative recombination in active region.

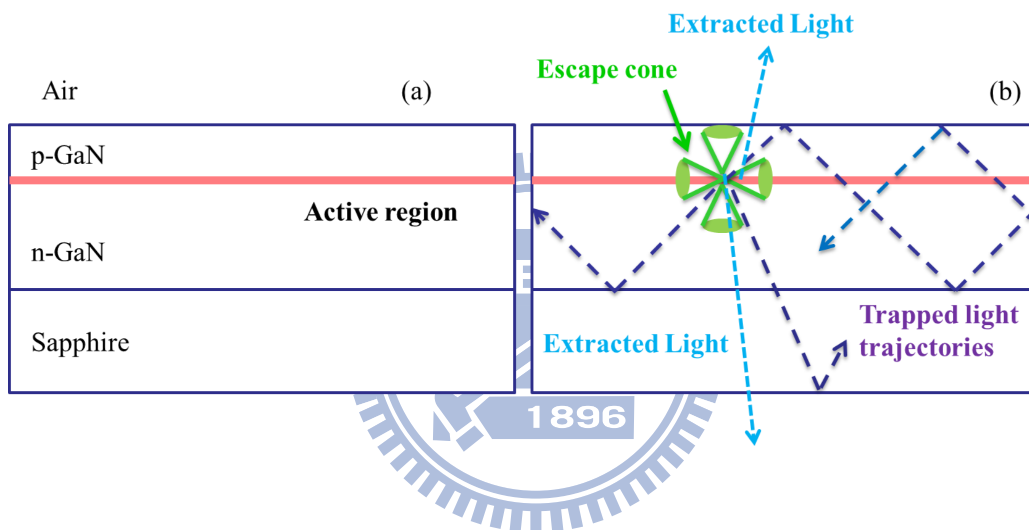

Fig. 2.3 (a) Cross-section schematic diagram of typical LED structures (b) Photon trajectories inside the LED

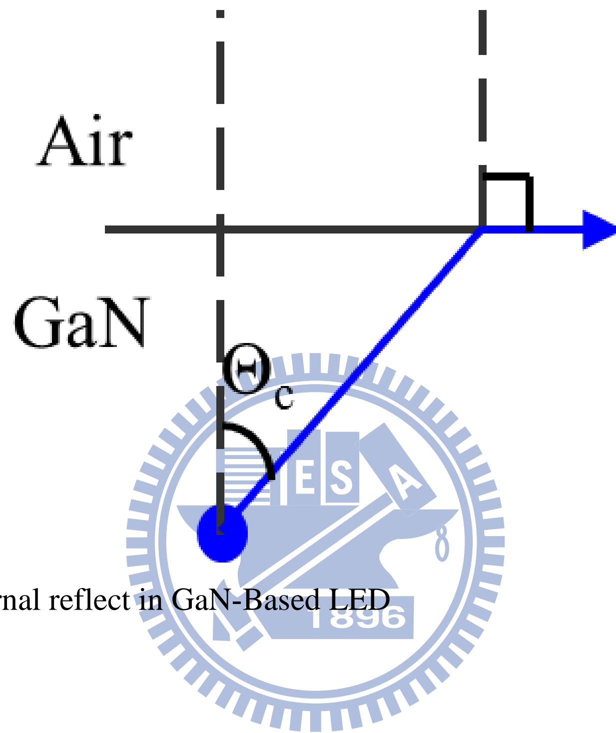

Fig. 2.4 Total internal reflect in GaN-Based LED

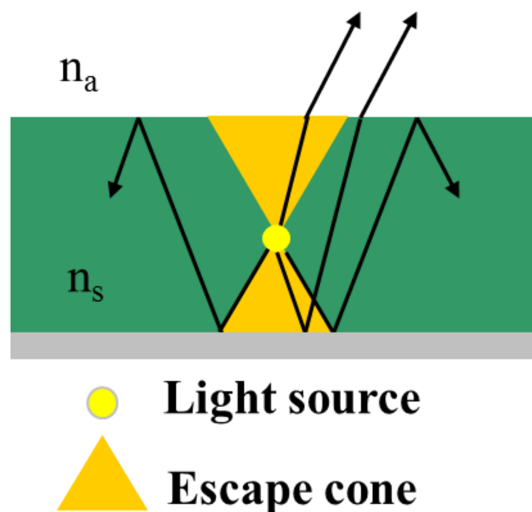

Fig. 2.5 The angle of total internal reflection defines the light-escape cone

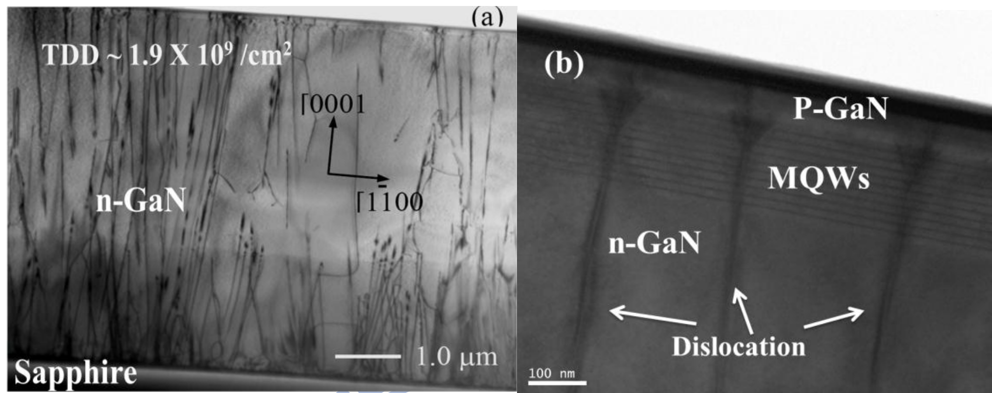

Fig. 2.6 (a) Cross section TEM image of typical GaN LED structure growth on sapphire substrate. (b) Enlarge TEM image of ten pairs multiple quantum well on GaN epitaxial layer.

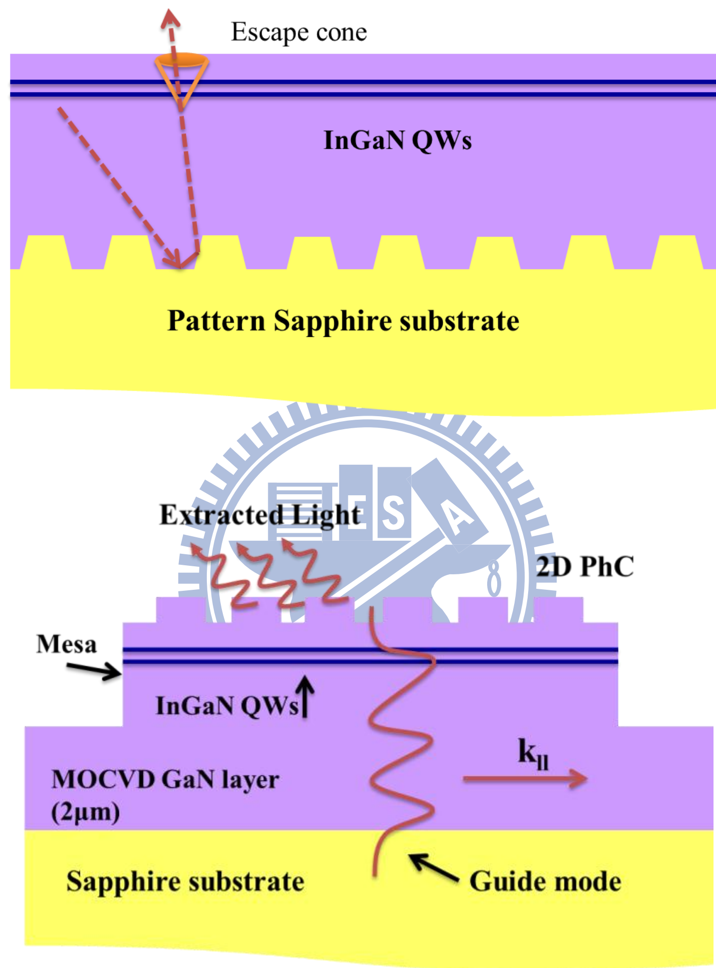

Fig. 2.7 Some LED light extraction schemes.

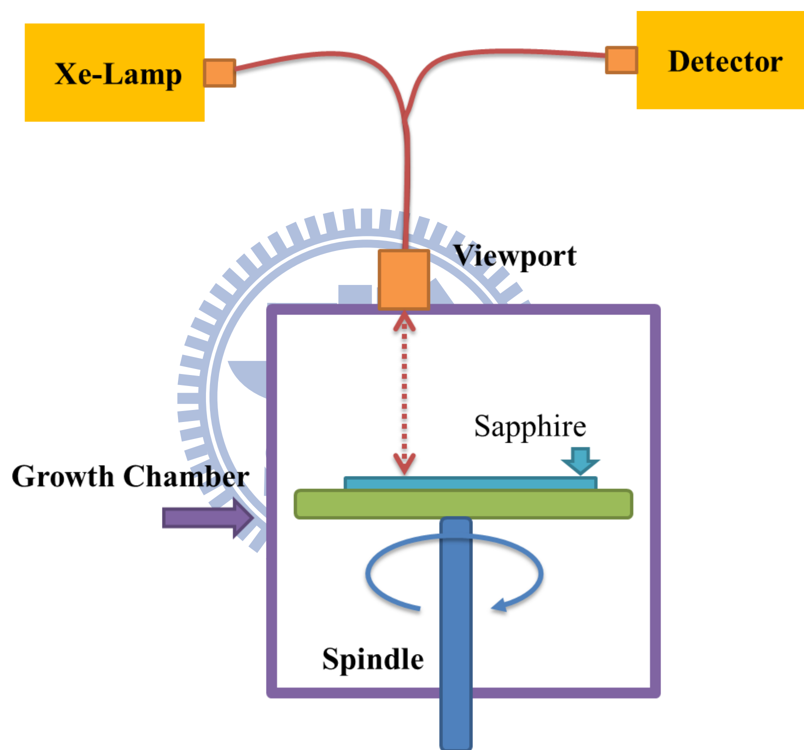

Fig. 2.8 Schematic of in-situ monitoring configuration.

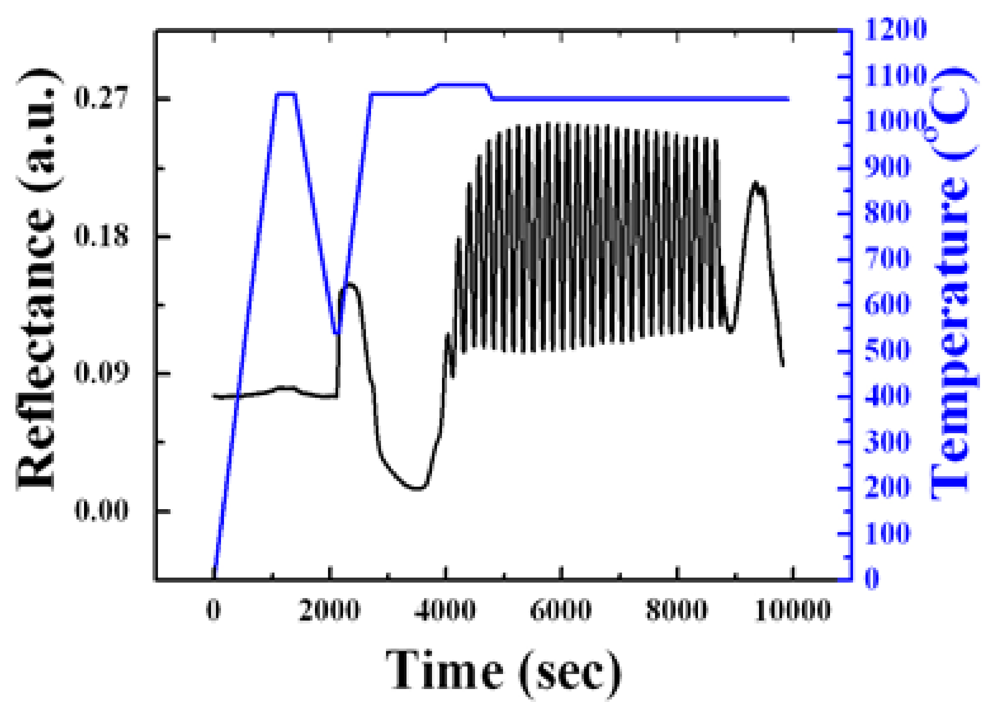

Fig. 2.9 The measured reflectivity of GaN bulk layer on sapphire substrate.

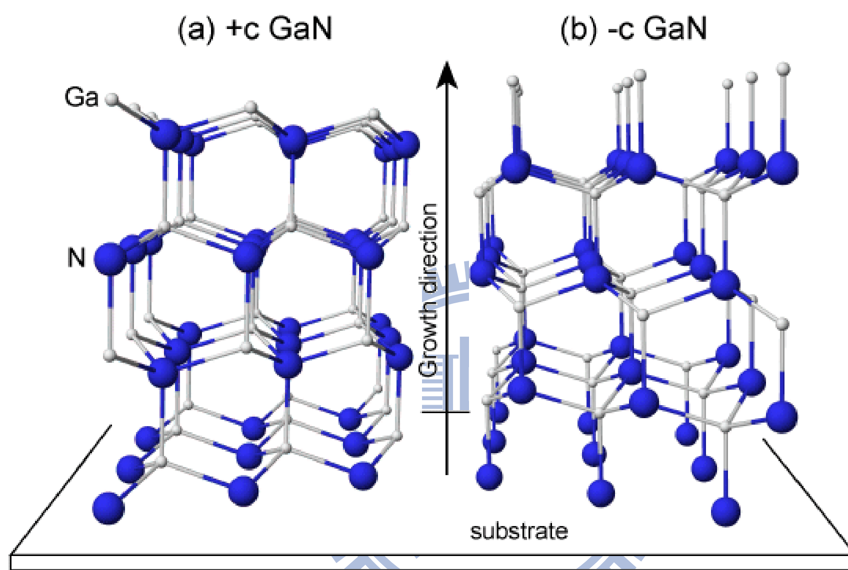

Fig. 2.10 Illustration of different polarity, (a) GaN-face ($+c$ GaN, Ga-polarity) (b) N-face ($-c$ GaN, N-polarity)

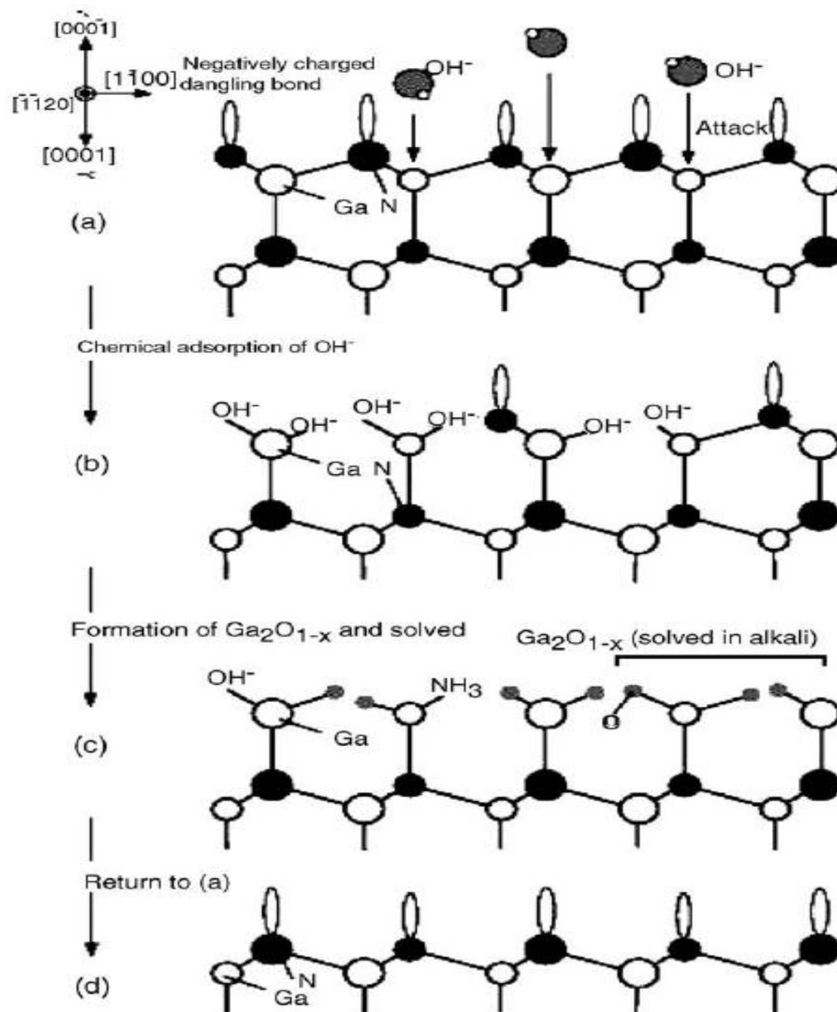

Fig. 2.11 Schematic diagrams of the cross-section GaN film viewed along the $[\bar{1}\bar{1}20]$ direction for N-polar GaN to explain the mechanism of the polarity selective etching. (a) Nitrogen terminated layer with one negatively charged dangling bond on each nitrogen atom; (b) adsorption of hydroxide ions; (c) formation of oxides; (d) dissolving the oxides

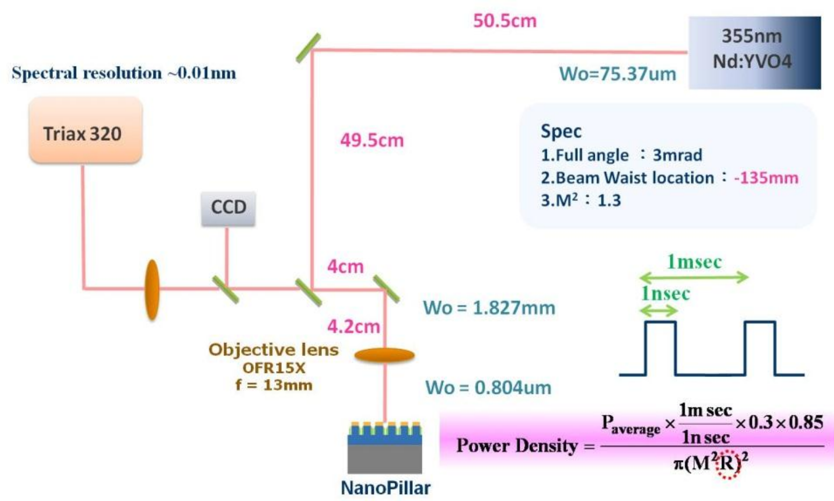

Fig. 2.12 Nd:YVO4 355-nm pulsed laser microPL measurement system

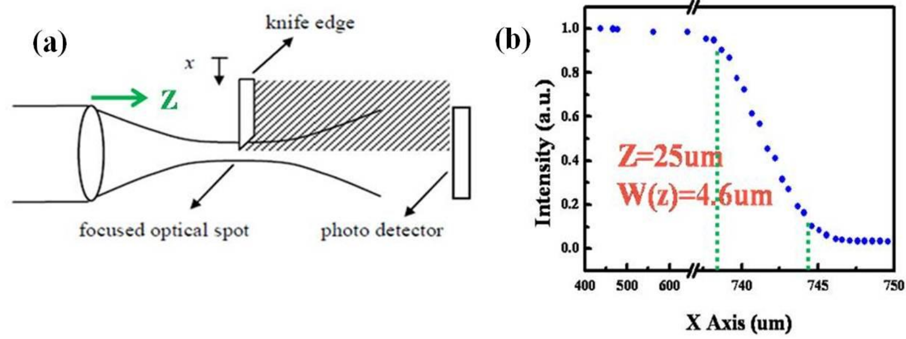

Fig. 2.13 (a) Knife Edge measurement diagram (b) the distance between lens and knife is 2 5μm,and laser beam spotsize is about 4.6μm

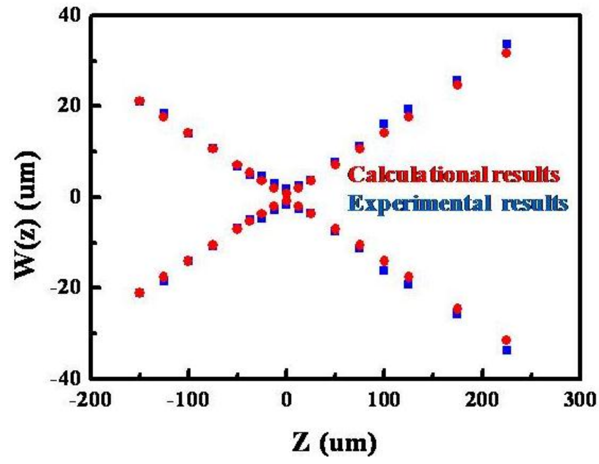

Fig. 2.14 Laser spotsize calculation and experimental results byknife edge measurement

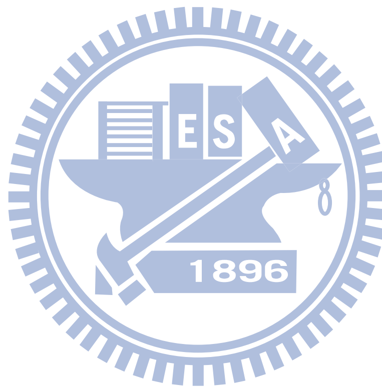

References

[1] A. Usui, H. Sunakawa, A. Sakai and A. A. Yamaguchi, Jpn. J. Appl. Phys. **36**, L889 (1997).

[2] M. Yamada, T. Mitani, Y, Narukawa, S. Shioji, I. Niki, S. Sonobe, K. Deguchi, M. Sano and T. Mukai, Jpn. J. Appl. Phys. **41**, L1431 (2002).

[3] Kenji ORITA, Satoshi TAMURA, Toshiyuki TAKIZAWA, Tetsuzo UEDA, Masaaki YURI, Shinichi TAKIGAWA and Daisuke UEDA Jpn. J. Appl. Phys. **43**,5809-5813(2004)

[4] J. B. Mullin, S. J. C. Irvine, and J. Tunnicliffe, J. Cryst. Growth, **68**, 214, (1984)

[5] B. Cockayne, and P. J. Wright, J. Cryst. Growth, **68**, 223, (1984)

[6] H. M. Manasevit, Appl. Phys. Lett. **12**, 156, (1968)

[7] S. Nakamura, T. Muksi, and M. Senoh, Appl. Phys. Lett. **64**, 1687, (1994)

[8] H. M. Manasevit, and W. I. Simpson, J. Electrochem. Soc, **116**, 1725, (1969)

[9] Alan G. Thompson, Materials Letters, **30**, 255, (1997)

[10] H. P. Maruska, and J. J. Tietjen, Appl. Phys. Lett., **15**, 367, (1969)

[11] H. M. Manasevit, F. Erdmann and W. Simpson, J. Electrochem. Soc, **118**, 1864, (1971)

[12] S.Yu. Karpov, V.G. Prokofjev, E.V. Yakovlev, R.A. Talalaev, Yu.N. Makarov, MRS J.Nitride Semicond. Res. **4**, 4, (1999)

[13] S. P. DenBaar, B. Y. Maa, P. D. Dapkus, and H. C. Lee, J. Cryst. Growth, 77, 188, 1986[14] D. E. Aspnes, IEEE J. Select. Topic Quant Elect., **1**, 1054, (1995)

[15] H. Amano, N. Sawaki, I. Akasaki, and Y. Toyoda, Appl. Phys. Lett., **48**, 353, (1986)

[16] S. Nakamura, Jpn. J. Appl. Phys., **30**, L1705, (1991)

[17] W. G. Breiland, and K. P. Klleen, J. Appl. Phys., **78**, 6726, (1995)

[18] T.L. Chu, J. Electrochem. Soc. **118**, 1200 (1971).

[19] J.I. Pankove, J. Electrochem. Soc. **119**, 1118 (1972).

[20]H. Cho, D.C. Hays, C.B. Vartuli, S.J. Pearton, C.R. Abernathy, J.D. MacKenzie, F. Ren, J.C. Zolper, Mater. Res. Soc. Symp. Proc. **483**, 265 (1998).

[21] C.B. Vartuli, S.J. Pearton, C.R. Abernathy, J.D. MacKenzie, F. Ren, J.C. Zolper, R.J. Shul, Solid-State Electron. **41** (12), 1947 (1998).

[22] S.J. Pearton, R.J. Shul, Gallium nitride I, in: J. Pankove, T.D. Moustakas (Eds.), Semiconductor and Semimetals Series, vol. **50**, Academic Press, New York, NY, p. 103 (1998).

[23] D. Li, M. Sumiya, S. Fuke, D. Yang, D. Que, Y. Suzuki, Y. Fukuda, J. Appl. Phys. **90**, 4219 (2001).

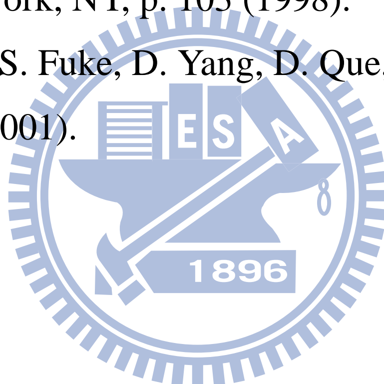

Chapter 3 Growth and fabrication of high quality atomic layer deposition GaN light emitting devices

3.1 The progress of AlGaN/GaN Multiple Quantum Well

The AlGaN/GaN multiple quantum wells (MQWs) have attracted much attention because of their unique properties, such as a high conduction band offset, better carrier confinement, large longitudinal (LO) phonon energy, and ultra-fast carrier and intersubband relaxation, making AlGaN/GaN MQWs promising structures for realizing ultraviolet (UV) light emitting diodes (LEDs), and laser diodes (LDs) [1-5]. Recent reports indicated that the optical and electrical properties of AlGaN/GaN MQWs were very sensitive to the crystalline quality and the threading dislocation density (TDD) in the AlGaN/GaN epilayer [6, 7]. So far most AlGaN/GaN MQWs structures were grown on lattice-mismatched foreign substrates such as sapphire, making it difficult to grow device-quality MQWs due to the lattice mismatch and the misfit in the thermal expansion coefficients between these two material systems. Recently high quality AlGaN/GaN heterostructures using quasi AlGaN formed by AlN/GaN superlattices as barrier layers was reported [8, 9]. However, these results mainly focused on the electrical properties used for AlGaN/GaN high electron mobility transistors and no optical properties were reported. In this paper, we report the growth of low dislocation density and crack-free AlGaN/GaN MQWs by using the atomic layer deposition (ALD) grown AlN/GaN superlattices (SLs) as the AlGaN barrier. The as-grown AlGaN/GaN MQWs sample had low defect density, smooth surface morphology with small root-mean-square (RMS) roughness value, and sharp interfaces. In addition, the AlGaN/GaN MQWs sample showed a sharp photoluminescence (PL) spectrum and a

uniform cathodoluminescence (CL) pattern.

3.2 The principle of Atomic Layer Deposition

Atomic Layer Deposition (ALD) is a chemical vapor deposition (CVD) technique, which is capable of processing extremely conformal, highly uniform and high quality thin films with really low amount of defects. A large number of standard materials are available for deposition in table 1[10]. The principle of ALD is based on sequential pulsing of special precursor vapors, each of which forms about one atomic layer each pulse. Since each pair of gas pulses (one cycle) produces exactly one monolayer of film, the thickness of the resulting film may be precisely controlled by the number of deposition cycles. Normally an ALD growth cycle consist four steps Fig. 3.1 (a) Exposure of the first precursor A, (b) purge of the chamber, (c) exposure of the second precursor B, and (d) further pure of the chamber. This growth cycle is repeated as long as desired film thickness is reached. The deposition may be defined as self-limiting since one, and only one, monolayer of the reactant species remains on the surface after each exposure. In this case, one complete cycle results in the deposition of one monolayer of the compound on the substrate. Repeating this cycle leads to a controlled layer-by-layer growth. Thus the film thickness is controlled by the number of precursor cycles rather than the deposition time, as is the case for a CVD processes. This self-limiting behavior is the fundamental aspect of ALD and understanding the underlying mechanism is necessary for the future exploitation of ALD.

3.3 The Fabrication of ALD AlGaN/GaN MQWs

The AlGaN/GaN MQW structures were grown by the low-pressure metal-organic chemical vapor deposition VEECO D75 system. The TMGa, TMAl and gaseous NH_3 were employed as the reactant sources for Ga, Al and N, respectively and H_2 and N_2 were used as the carrier gaseous. The (0001)-oriented sapphire substrate with a 0.2° offset was first heated to 1000°C under an H_2 ambient for 5 min. Then, a 2-µm-thick GaN epilayer was grown after the deposition of a low-temperature nucleation layer. Finally, the AlGaN/GaN MQWs structure comprising three GaN wells and four AlGaN barriers were grown at 850°C in H_2+N_2 atmosphere. Particularly, the AlGaN barriers were grown using the ALD technique. The ALD process involves alternate control of mass flow of TMAl and TMGa gas during the growth of AlGaN barrier to form six pairs of AlN/GaN SLs. Fig. 3.2 shows the growth procedure of the AlGaN barrier and GaN well layer. The TMAl and TMGa flow time of AlN and GaN layer were 6.8 and 19.8sec, respectively under a continuous flow of the NH_3 gas at 850°C. The growth rate of the ALD grown AlGaN barrier measured by an *in-situ* Filmetrics optical monitoring system was about 0.14µm/hr. After the AlGaN barrier was grown, only TMGa was introduced into the reactor for 34.8second to grow the GaN well.

3.4 Characteristic of AlGaN/GaN MQWs with ALD grown AlGaN Barriers

The surface morphology of the as-grown sample was observed by atomic force microscope (AFM) with a scanning area of 5 µm × 5 µm. Crystalline quality was evaluated by high resolution X-ray diffraction (HRXRD) and reciprocal space mapping (RSM), and Cu K_{α} radiation

was used as the X-ray source. The average thicknesses of the AlGaN barriers and the GaN wells were determined from the angular distance between satellite peaks in (0002) ω/2θ-scan. The optical properties were investigated by PL measurements. PL spectra were excited with a frequency tripled Ti: sapphire laser at wavelength of 266nm and the laser output power was 20mW. The laser pulse width was 200fs and the repetition rate was 76MHz. The luminescence spectrum was measured by a 0.5m monochromator and detected by a photomultiplier tube. The cathodoluminescence (CL) measurements were carried out at 300K by using a MonoCL system installed on a field emission scanning electron microscope (SEM) with beam energies of 5–20keV. The threading dislocations and the sharpness of the AlGaN/GaN interfaces were studied by transmission electron microscope (TEM). The dislocation density of the sample surface with an area of 20μm × 26μm was analyzed after the 5-minute etching in the KOH solution with 0.005M at 80°C.

Fig. 3.3 and Fig. 3.4 show the HRXRD ω/2θ diffraction pattern and the RSM of the as-grown AlGaN/GaN MQWs sample. In Fig. 3.3, the HRXRD diffraction pattern shows two periodical structures: one can be attributed to the AlGaN/GaN MQWs; another can be attributed to the AlN/GaN SLs in the AlGaN barriers. The third order satellite peak of the diffraction pattern for AlGaN/GaN MQWs can be clearly observed, suggesting the high crystalline quality of AlGaN/GaN MQWs and AlN/GaN SLs. From Bragg formula of adjoining satellites peak

$$2\wedge = \sin\theta_L = L\lambda \tag{3-1}$$

$$2\wedge = \sin\theta_L = (L+1)\lambda \tag{3-2}$$

Where, $\wedge$ is θ_L and λ are the period of SLs, the X-ray wavelength, Bragg angle of the SLs L-order satellite peak, respectively. When we define $\Delta\theta_m = \theta_{L+1} - \theta_L$ and use Equation (2)-(1), the period $\wedge$ is given

by the follow equation

$$\Lambda = \lambda / \left\{ 4 \left[\cos\theta_L \cos\left(\frac{\Delta\theta}{2}\right) - \sin\theta_L \sin\left(\frac{\Delta\theta}{2}\right) \right] \sin\left(\frac{\Delta\theta}{2}\right) \right. \qquad (3\text{-}3)$$

Expanding the above equation as Taylor series and omitting the high orders of $\Delta\theta_m$ the period of SLs can be expressed by following equation

$$\Lambda = \lambda / \left\{ 2 \left[\cos\theta_L - \frac{\Delta\theta_m}{2} \sin\theta_L \right] \Delta\theta_m \right. \qquad (3\text{-}4)$$

The thickness of AlN and GaN in the barrier and the GaN wells can be fitted to be about 0.42, 0.77, and 2.9 nm, respectively. The average Al content of AlGaN barrier is also estimated to be about 0.29. From the RSM data of AlGaN/GaN MQWs obtained from $(10\bar{1}5)$ diffraction shown in Fig. 3.4, the spread of RSM intensity for the AlGaN/GaN MQWs was relatively narrow indicating AlGaN epilayers exhibited relatively small distribution of crystal orientation [11]. In addition, the reciprocal lattice points of AlGaN and GaN were lined up at the same Q_x position (red solid line) indicating the AlGaN and GaN had same lattice constant. According the earlier report [12], the degree of lattice relaxations can be estimated from the equation of

$$\varepsilon_{xx} = q_x^{GaN} / q_x^{MQWs} - 1 \qquad (3\text{-}5)$$

, where the q_x^{GaN} and q_x^{MQWs} are the x position of GaN layer and AlGaN layer, respectively. We obtained an estimated degree of lattice relaxation to be only 3.9×10^{-6}, indicating the AlGaN epilayer is fully strained and pseudomorphic to the underlying GaN layer.

As shown in Fig. 3.5, the surface morphology of the top layer was observed by atomic force microscope and no cracks were found. A very small RMS value of the surface roughness of 0.35 nm was achieved. To carefully investigate the threading dislocation within our sample, both cross-sectional and plane-view TEM images were taken. Fig. 3.6 shows the cross-sectional TEM image of the sample with the white dash lines

indicating the top and bottom GaN epilayer regions. It is clear that few dislocations are observable and only one dislocation passes through the GaN epilayer into AlGaN/GaN MQWs. The dislocation density (DD) at the bottom GaN layer is about $3.5\times10^{8}cm^{-2}$ and slightly reduces to $1.4\times10^{8}cm^{-2}$ at the top GaN layer. However, the DD in the AlGaN/GaN MQWs region is only $2.5\times10^{7}cm^{-2}$. Fig. 3.7 shows the plane-view bright-field TEM image from the top surface. The dislocation density was estimated to be about $3.2\times10^{7}cm^{-2}$. Meanwhile, we also estimate the dislocation density in this AlGaN/GaN MQWs sample by evaluating the etch-pit density (EPD) of the KOH etched sample. We obtain an estimated EPD value of about $3.3\times10^{7}cm^{-2}$, which is similar to the above estimated plain-view DD value. These estimated DD values of our sample are nearly two orders of magnitude lower than that of AlGaN films, which were not grown by ALD, reported recently [13]. From the enlarged TEM image shown in the inset of Fig. 3.8, it can be clearly observed that the QWs and SLs exhibited sharp interfaces with good periodicity, showing that the high quality SLs and MQWs were formed by the ALD technique. The image also show that the AlGaN barrier consisted of six pairs AlN/GaN SLs with AlN thickness of 0.43nm and GaN thickness of 0.77nm, respectively forming a AlGaN barrier with thickness of 7.2nm, and the GaN well had a thickness of 3nm, which are in good agreement with the result estimated from HRXRD data.

Interestingly, a bending of threading dislocations at the boundary of MQWs without extending into the top surface was commonly observed in this sample as shown in Fig. 3.8. Previous it was reported [14] that the strain in the epi-layer could exert a net force on the dislocation to be bended or terminated at the strained epilayer edge without threading through the epilayer to the top surface. Since our RSM result

demonstrated that the AlGaN epilayer is fully strained, it suggested that the large strain in the ALD grown AlGaN barrier with AlN/GaN SLs could effectively bend and suppress the threading dislocations, thus reducing the defects in MQW and improving the surface morphology of the sample.

Fig. 3.9 shows the PL spectra of the as-grown sample. The emission peak energy at 3.60 eV and 3.71 eV was observed at room temperature and 13K, respectively. The full width at half maximum (FWHM) of PL spectra is about 80meV at room temperature and reduces to only 47meV at 13K, which are smaller than the previous report by a factor of 2-3 [15], indicating that the crystal quality of AlGaN/GaN MQWs has been improved by using ALD AlGaN barrier. Our PL data analysis confirmed that the two dominant emission peak energy of 3.60eV and 3.71eV at room temperature and 13K, respectively, was emitted from GaN well. In addition, the emission peak energy at 3.62eV can be clearly observed at 13K. According to previous report, the emission peak energy of 3.62eV could be attributed to the LO phonon [16]. Additionally, the inset of Fig. 3.9 shows the CL image of the sample which has near uniform brightness with few dark spots. It was well-known that the dark spots in CL image were related to non-radiative centers in the defects of epilayers. Therefore the CL image data again suggest our sample has relatively low dislocation density and superior crystalline quality.

3.5 Fabrication of near UV LED with ALD insert layer

The high dislocation density led to the poor performance of LED because the threading dislocation density act non-radiative centers and reduce the radiative recombination efficiency. In our early reports, the strain atomic layer is very useful for suppression of dislocation in lattice mismatch epilayers. Therefore, low dislocation density is a key issue for

high efficient light emitting devices. Based on the realization of high efficient UV light emitting devices, we will further fabricate near UV LEDs with inserting ALD-AlGaN/GaN strain layer. The proposed UV -LEDs with ALD-AlGaN/GaN strain layer (ALD-LED) and conventional near UV LEDs (C-LED) were show in Fig 3.10.

3.6 Performance of near UV LED with ALD insert layer

The light-current (L-I) and voltage-current (V-I) characteristics are shown in Fig. 3.11. The forward voltages of ALD-LED and C-LED are respectively 3.84 and 3.90 V at 20 mA and increase to 5.41 and 5.45 V at 100 mA. The electric characteristic of ALD-LED is still reasonably well maintained. The light output power for the GaN-based LED with an ALD insert layer at 20 mA was 27% higher than that for a conventional GaN-based LED structure.

In summary, we have grown low dislocation and high crystalline quality AlGaN/GaN MQWs on sapphire substrate by using the ALD grown AlGaN barrier consisted of AlN/GaN SLs. The AFM data show smooth surface morphology with a small surface roughness RMS value of about 0.35 nm and no surface cracks. The TEM and HRXRD measurements show that the grown sample has sharp interfaces between SLs layers and QWs with good periodicity. The sample has near uniform CL image intensity at room temperature and narrow PL emission peak. The sample has a low dislocation density of about 3.3×10^{7} cm^{-2}. These results indicate that the AlGaN/GaN MQWs grown by the ALD technique is a viable method for growth of a device-quality AlGaN/GaN MQWs structure for various optical devices. The light output power for the GaN-based LED with an ALD insert layer at 20 mA was 27% higher than

that for a conventional GaN-based LED structure

Compound class	**Examples**
II–VI compounds	ZnS, ZnSe, ZnTe, $ZnS_{1-x}Se_x$, CaS, SrS, BaS, $SrS_{1-x}Se_x$, CdS, CdTe, MnTe, HgTe, $Hg_{1-x}Cd_xTe$, $Cd_{1-x}Mn_xTe$
II–VI based thin-film electroluminescent (TFEL) phosphors	ZnS:M (M = Mn, Tb, Tm), CaS:M (M = Eu, Ce, Tb, Pb), SrS:M (M = Ce, Tb, Pb, Mn, Cu)
III–V compounds	GaAs, AlAs, AlP, InP, GaP, InAs, $Al_xGa_{1-x}As$, $Ga_xIn_{1-x}As$, $Ga_xIn_{1-x}P$
Semiconductors/dielectric nitrides	**AlN, GaN, InN**, SiN_x
Metallic nitrides	TiN, TaN, Ta_3N_5, NbN, MoN
Dielectric oxides	Al_2O_3, TiO_2, ZrO_2, HfO_2, Ta_2O_5, Nb_2O_5, Y_2O_3, MgO, CeO_2, SiO_2, La_2O_3, $SrTiO_3$, $BaTiO_3$
Transparent conductor oxides	In_2O_3, In_2O_3:Sn, In_2O_3:F, In_2O_3:Zr, SnO_2, SnO_2:Sb, ZnO,
Semiconductor oxides	ZnO:Al, Ga_2O_3, NiO, CoO_x
Superconductor oxides	$YBa_2Cu_3O_{7-x}$
Fluorides	CaF_2, SrF_2, ZnF_2

Table 3.1 Examples of thin film materials deposited by ALD including films deposited in epitaxial

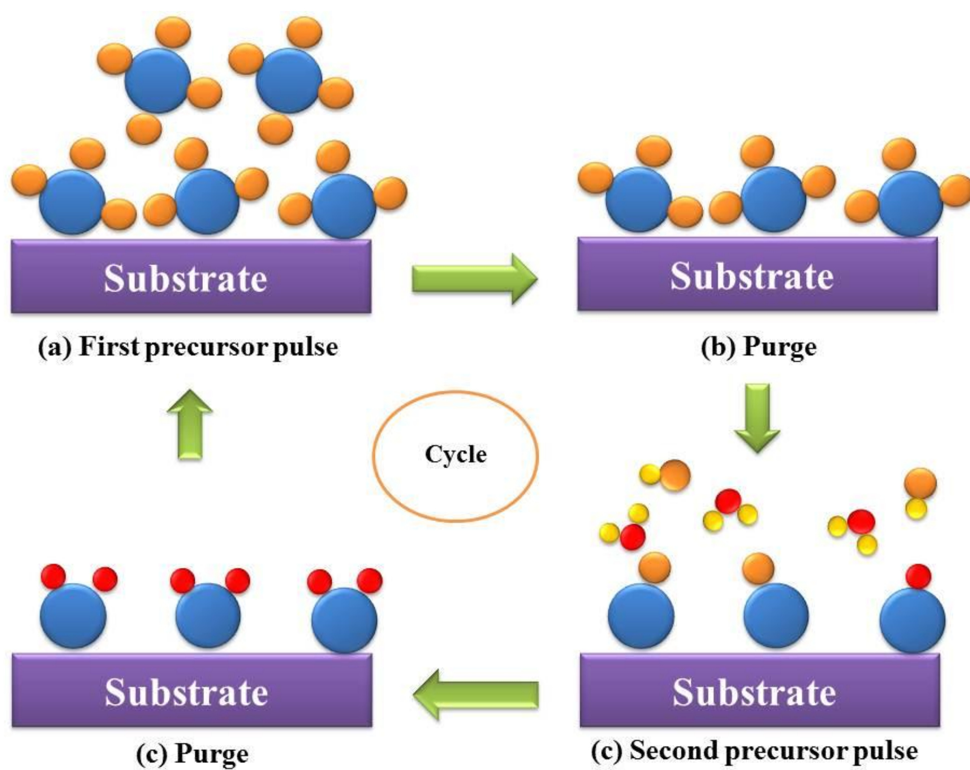

Fig. 3.1 Schematic representation of an ALD process

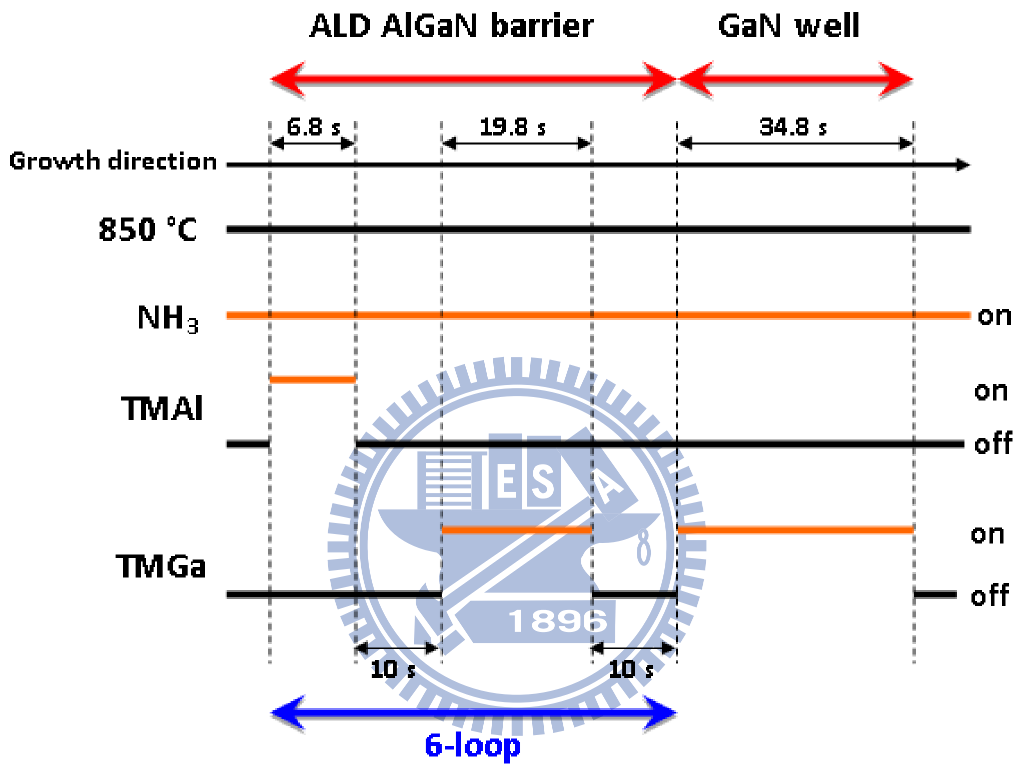

Fig. 3.2 Growth procedure of AlGaN barrier and GaN well layers

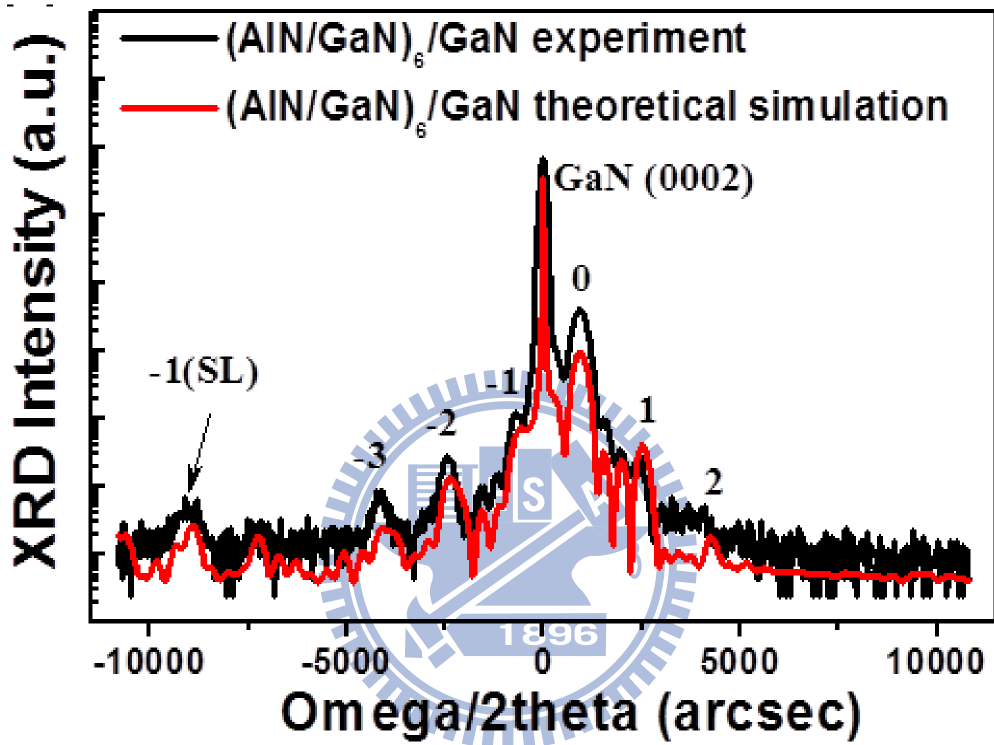

Fig. 3.3 High-resolution x-ray diffraction pattern at (0002) plane for the AlGaN/GaN MQWs sample

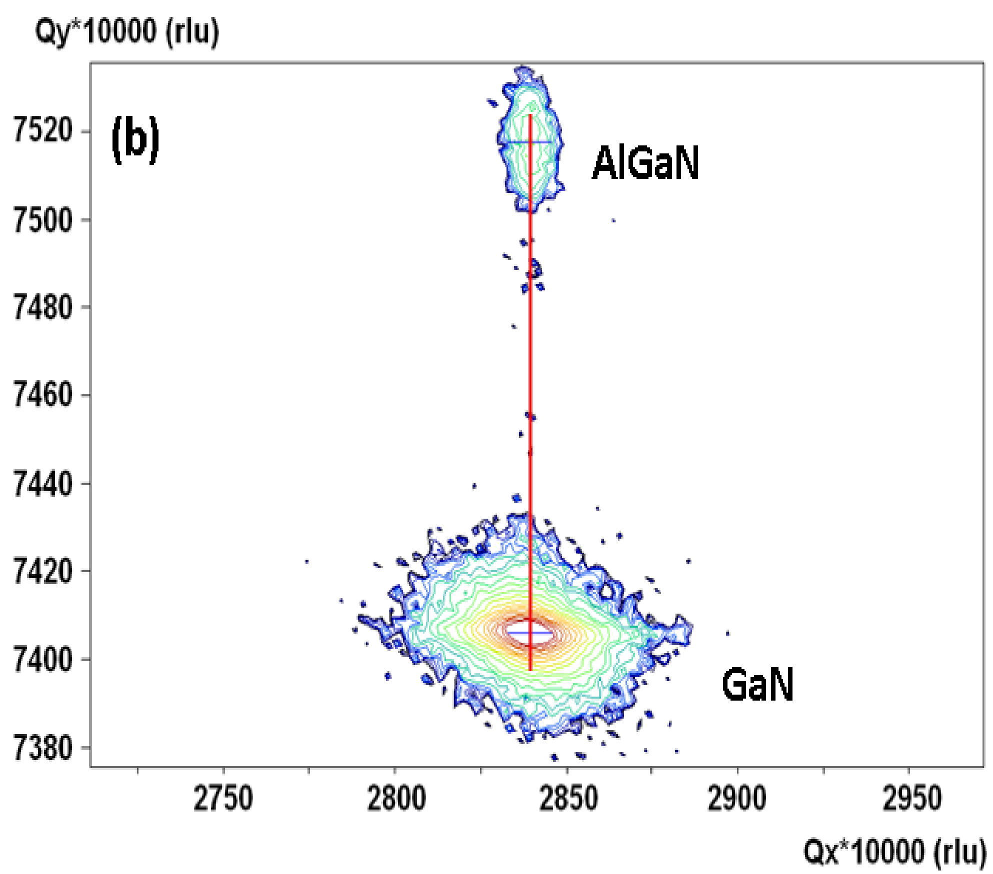

Fig. 3.4 RSM of the sample obtained from $(1\,0\,\bar{1}\,5)$ diffraction

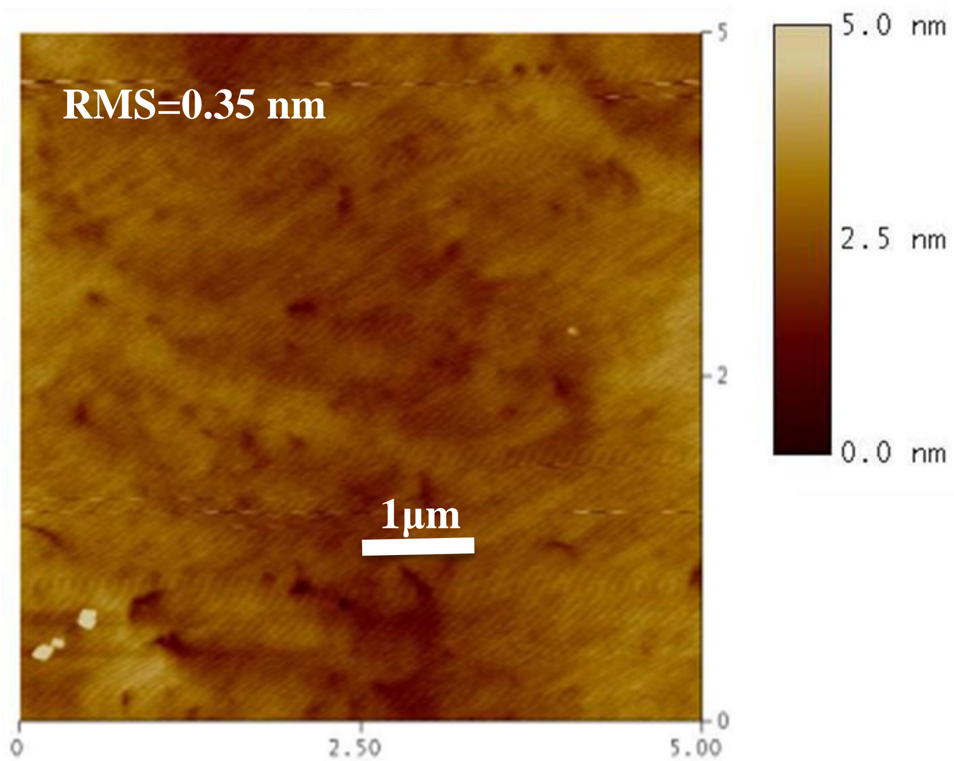

Fig. 3.5 Surface morphology of the grown AlGaN/GaN MQWs sample scanned by AFM

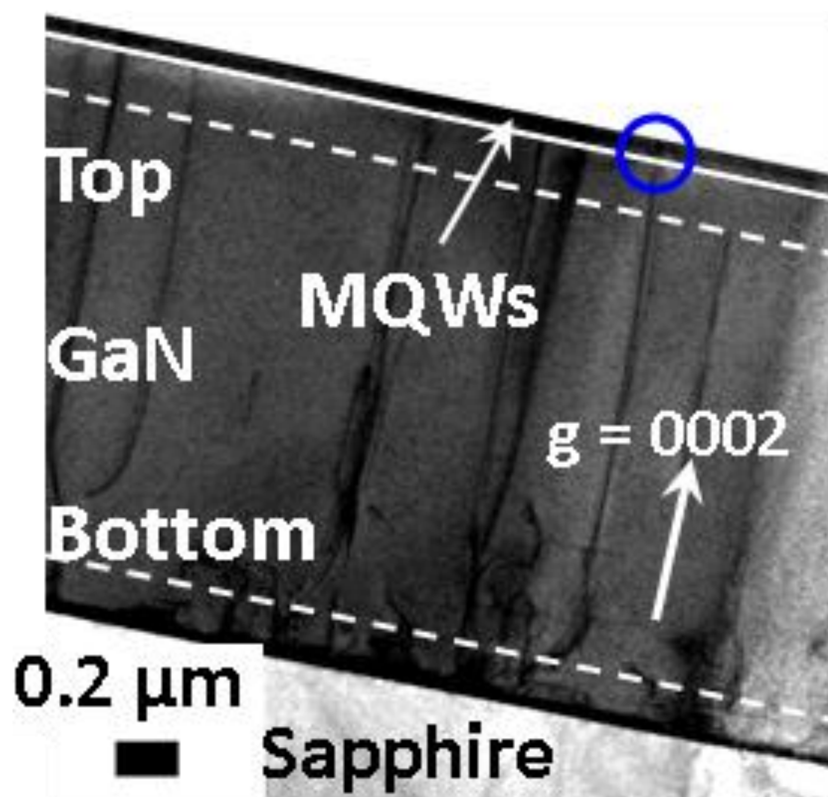

Fig. 3.6 Cross-sectional TEM image of the grown sample

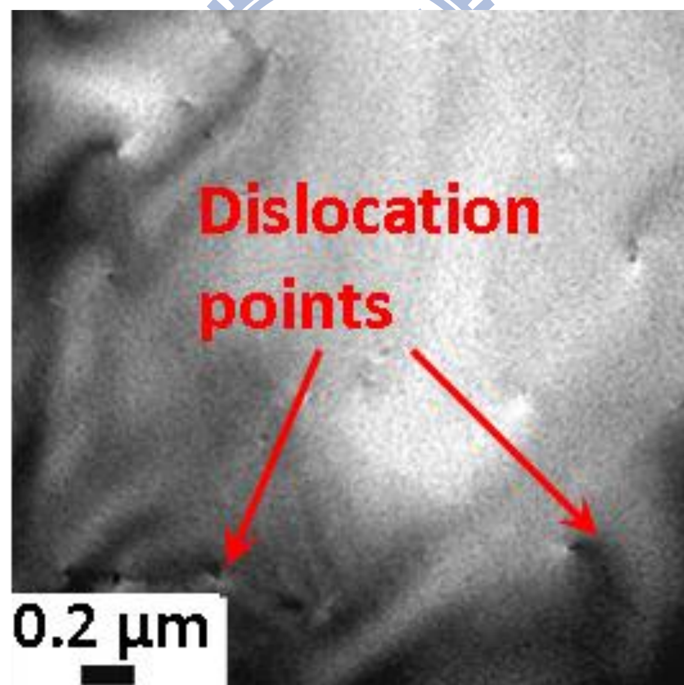

Fig. 3.7 Plane-view TEM image of the AlGaN/GaN MQWs sample

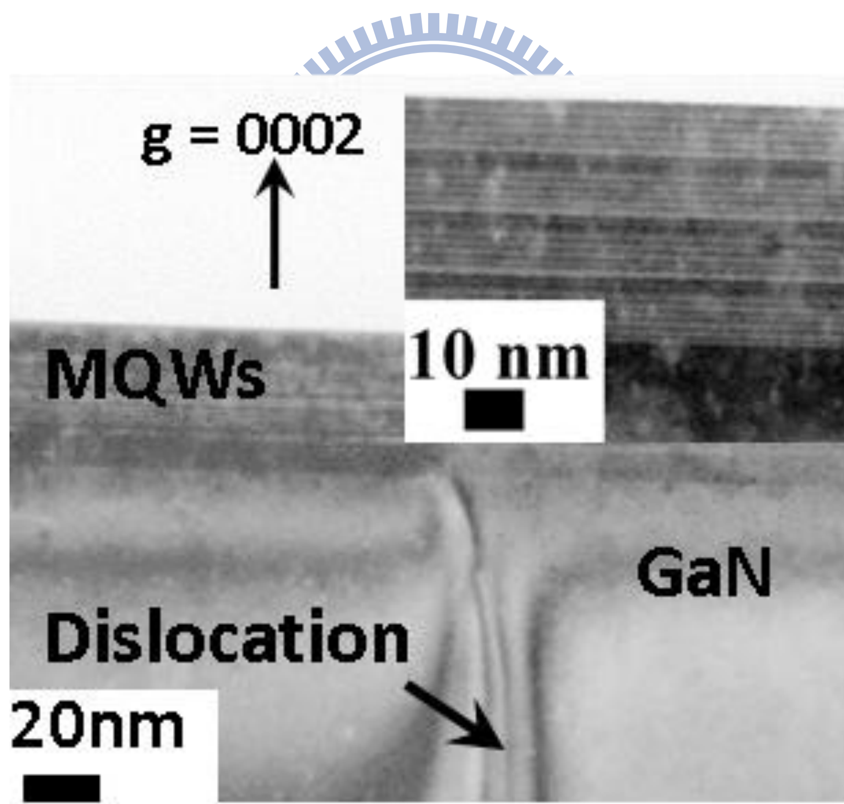

Fig. 3.8 Enlarged cross-sectional TEM images of the sample

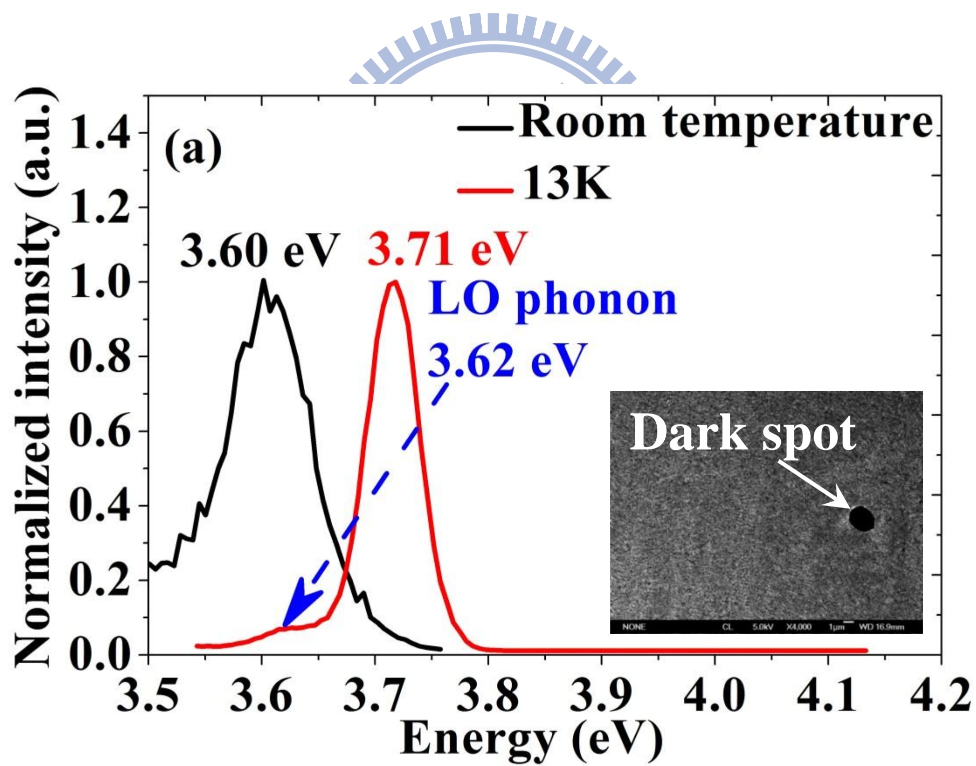

Fig. 3.9 The 13K and room temperature PL spectra of the AlGaN/GaN MQWs sample. Inset shows CL image taken at E = 3.71 eV.

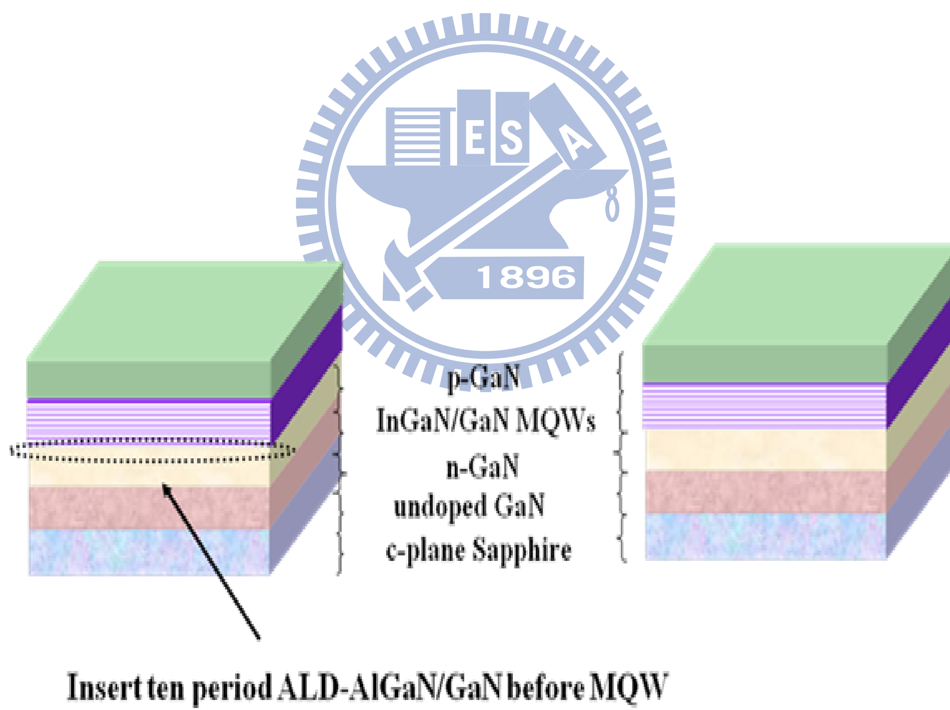

Fig. 3.10 The schematic diagram of the two fabricated LEDs

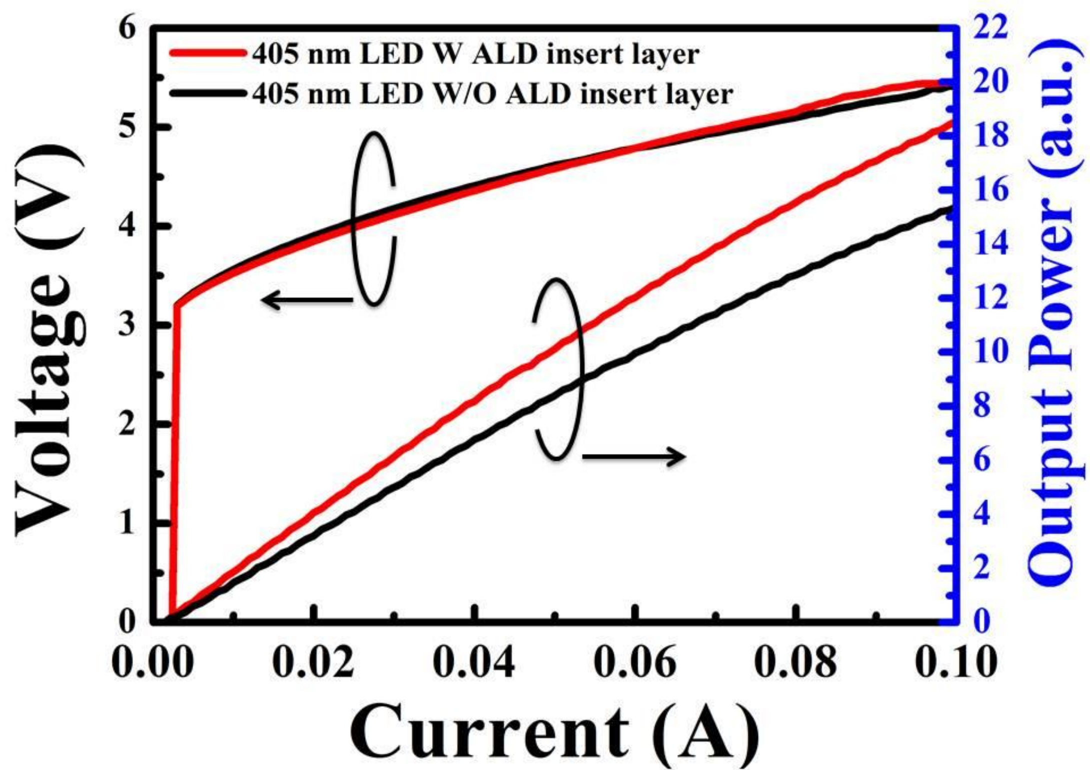

Fig. 3.11 L-I-V characteristics of the two fabricated LEDs

References

[1] Norio Iizuka, Kei Kaneko, Nobuo Suzuki, Takashi Asano, Susumu Noda, and Osamu Wada, Appl. Phys. Lett. **77,** 648 (2000).

[2] Ü mit Ö zgür, Henry O. Everitt, Lei He, and Hadis Morkoç, Appl. Phys. Lett. **82,** 4080 (2003).

[3] T. J. Schmidt, X. H. Yang, W. Shan, J. J. Song, A. Salvador, W. Kim, Ö. Aktas, A. Botchkarev, and H. Morkoç, Appl. Phys. Lett. **68,** 1820 (1996).

[4] J. Han, M. H. Crawford, R. J. Shul, J. J. Figiel, M. Banas, and L. Zhang, Y. K. Song, H. Zhou, and A. V. Nurmikko, Appl. Phys. Lett. **73,** 1688 (1998).

[5] Joan M. Redwing, David A. S. Loeber, Neal G. Anderson, Michael A. Tischler, and Jeffrey S. Flynn, Appl. Phys. Lett. **69,** 1 (1996).

[6] Takayoshi Takano, Yoshinobu Narita, Akihiko Horiuchi, and Hideo Kawanishi, Appl. Phys. Lett. **84,** 3567 (2004).

[7] V. Adivarahan, W. H. Sun, A. Chitnis, M. Shatalov, S. Wu, H. P. Maruska and M. Asif Khan, Appl. Phys. Lett. **85,** 2175 (2004).

[8] Y. Kawakami, X.Q. Shen, G. Piao, M. Shimizu, H. Nakanishi, and H. Okumura, J. Crystal Growth **300,** 168 (2007).

[9] Y. Kawakami, A. Nakajima, X. Q. Shen, G. Piao, M. Shimizu, and H. Okumura, Appl. Phys. Lett. **90,** 242112 (2007).

[10] Adapted from M. Ritala and M. Leskel, Nanotechnology, 1999, 10, 19.

[11] Y S Park, C M Park, S J Lee, Hyunsik Im, T W Kang, Jae-Eung Oh, Chang Soo Kim, and Sam Kyu Noh, Semicond. Sci. Technol. **20,** 775 (2005).

[12] G. S. Huang, T. C. Lu, H. H. Yao, H. C. Kuo, S. C. Wang, Chih-Wei

Lin, and Li Chang, Appl. Phys. Lett. **88,** 061904 (2006).

[13] D. M. Follstaedt, A. A. Allerman, S. R. Lee, J. R. Michael, K. H. A. Bogart, M. H. Crawford, N. A. Missert, J. Cryst. Growth. **310,** 766 (2008).

[14] J. Knall, L. T. Romano, D. K. Biegelsen, R. D. Bringans, H. C. Chui, J. S. Harris, Jr., D. W. Treat, and D. P. Bour, J. Appl. Phys. **76,** 2697 (1994).

[15] Hideki Hirayama, J. Appl. Phys. **97,** 091101 (2005).

[16] M. Smith, J. Y. Lin, H. X. Jiang, A. Salvador, A. Botchkarev, W. Kim, and H. Morkoc, Appl. Phys. Lett. **69**, 2453 (1996).

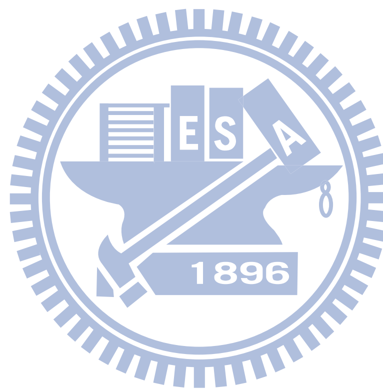

Chapter 4 Defect selective passivation in GaN epitaxial growth and its application to light emitting diodes

4.1 The progress of low defect high quality GaN based light emitting devices

GaN based light emitting devices have attracted great attention in last few years due to its importance in solid state lighting applications. Researchers are actively investigating various approaches to improve device performance. The devices are often epitaxially grown on foreign substrates, for example sapphire. The as grown GaN epitaxial layer has high threading dislocation (TD) density typically in the range of 10^{8-10} cm^{-2} due to the mismatches in lattice constants and thermal expansion coefficients between GaN and sapphire. These defects are non-radiative recombination centers and are detrimental to optoelectronic device performance. The reduction of TD is of great importance for the development of GaN based devices.

There are several epitaxial growth methods to improve crystal quality. A very commonly used one is the epitaxial lateral overgrowth technique (ELOG) [1, 2]. Strips of SiO_2 mask along specific crystal direction are deposited on GaN epi-surface, followed by epitaxial growth. The growth starts from the window regions and grows vertically as well as laterally to cover the SiO_2 strips until obtaining planar surface over whole wafer. The lateral growth above mask area bends the propagation direction of threading dislocation and results in significantly lower defect density. The defect density is however still high at window regions and coalescent

boundaries. Another approach is to use patterned sapphire substrate for epitaxial growth [3, 4], but the reduction in TD defect density is often not as effective as ELOG method. Other methods use in-situ SiNx or ex situ TiNx porous insertion layers [5, 6], where GaN nucleates from the pores of the inserted layer and lateral overgrowth on top of it. Recently, defect reduction methods using defect selective etching followed by metalorganic chemical vapor deposition MOCVD [7] or hydride vapor phase epitaxy [8] regrowth have also been reported. In this letter, we demonstrate a TD reduction method by self-aligned defect selective passivation without the need of photolithography and use it to fabricate a high efficiency LED. The defect selective passivation is done by defect selective etching, SiO_2 passivation at etch pits, and epitaxial over growth.

4.2 The Fabrication of defect passivation LED

The schematic of process flow is shown in Fig. 4.1. A 30 nm of low temperature GaN nucleation layer followed by a 2 μm GaN buffer layer is grown on (0001) sapphire template by low pressure MOCVD. The GaN wafer is immersed in high temperature molten KOH at 280°C for 10 minutes. The molten KOH selectively etches defect sites and forms hexagonal pits on GaN surface [9] as illustrated in Fig. 4.1(a). There can be one or several TDs under an etch pit (EP) and the KOH etching may not etch all defects, which will be explained later. A 0.5 μm SiO_2 film is deposited on the etched surface by plasma enhanced chemical vapor deposition as shown in Fig. 4.1(b). The SiO_2 thin film on the flat surface area is then removed by chemical mechanical polishing, which leaves only SiO_2 at the etched pits as shown in Fig. 4.1(c). The SiO_2 fillings at

etch pits act as defect passivation to block the continuous propagation of TDs in the subsequent epitaxial growth. The exposed GaN flat surface provides the seed layer for epitaxial re-growth, which grows in both vertical and lateral direction to cover over the SiO_2 passivated pits as shown in Fig. 4.1(d). This defect passivation and regrowth process can be viewed as a variation of conventional ELOG method but with some unique advantages. First, photolithography patterning is not required. Secondly, micro SiO_2 masks are self-aligned to the TD pits created by defect selective etching. Thirdly, the size of each mask is exactly matched to individual etch pit size. This method, compared to ELOG, provides defect selective passivation rather than random blocking of TD defects.

Fig. 4.2 shows the random distribution of hexagonal pits on the top surface of as-grown sample after molten KOH etching. The etched crystal planes are mostly {1-101} facets. Aside from individual hexagonal pits, there are often several pits clustered together. The etch pit density counting all the individual pits is about 5×10^8 cm^{-2}. The deposited SiO_2 thin film follows the etched pit topography as shown in Fig. 4.3. After CMP process, only SiO_2 in etched pits are left as shown in Fig. 4.4. Small pits are filled with SiO_2. For large pits, SiO_2 only fills the side walls leaving a void in the center. The subsequent MOCVD epitaxial over growth covers the whole wafer with flat surface. A LED structure with 2 μm Si-doped n-GaN, 10 pairs of InGaN/GaN multiple quantum wells (MQWs), and a 30 nm Mg-doped p-GaN were grown on the template. The QW emission wavelength is at 425 nm.

4.3 Characteristic of DP-LEDs

To assess the TD reduction, a tunneling electron microscope (TEM) image was taken as shown in Fig. 4.5. The TD density can be estimated

by directly counting the TD lines in the plane-view micrograph. The TD density estimated at the dashed line right below defect passivation layer is about $1x10^9$ cm^{-2}. This number is slightly larger than the KOH etch pit density $5x10^8$ cm^{-2}. The discrepancy is due to the fact that there can be multiple TDs under an etch pit as can be seen in Fig. 4.5. The TD density is significantly reduced to $4x10^7$ cm^{-2} at the dashed line near the QW region. SiO_2 passivations at etched pits do effectively block the propagation of TDs. The SEM image however also shows that SiO_2 fillings do not occur on top of all TDs. In other words, no all the TDs are etched by molten KOH. As a result, some TDs are not blocked and propagate all the way to the top surface. Those TDs not etched by KOH are presumably specific types of TDs resistive to molten KOH etching. It has been reported that KOH preferentially etches screw type TD and is less effective in etching edge and mixed type TDs [10]. To verify if those TDs propagating all the way to the top surface are resistive to KOH etching, the regown sample was put in molten KOH under the same etching conditions again. The SEM image of the etched sample is shown in Fig. 4.6. There are much less etch pits, with density of only $1x10^5$ cm^{-2}. The great reduction in etch pit density from $5x10^8$ to $1x10^5$ cm^{-2} shows that the TDs that can be etched by KOH are mostly blocked by the SiO_2 fillings in the defect selective passivation process. The etch pit density $1x10^5$ cm^{-2} is much smaller than the TD density $4x10^7$ cm^{-2} estimated from the cross section TEM image near surface region. Most of TDs not blocked by defect passivation process are those resistive to KOH etching. The sample was subsequently immersed in 195°C H_3PO_4 solution for 20 minutes. It has been reported that KOH and H_3PO_4 have different preferential crystallographic etch planes [11]. The surface SEM image is shown in Fig. 4.7. The H_3PO_4 etch pit morphology is very different from

that of KOH etching. The etch pit density is about $1.2x10^{7}$ cm^{-2}. This number is close to the TD density estimated from the TEM image near surface region. This implies that KOH and H_3PO_4 somehow etches different defect types of TDs and both should probably be used to etch TDs in the defect selective etching process to increase defect passivation coverage.

The optical characteristic is investigated by cathodluminescent (CL) and SEM cross section images as shown in Fig. 4.8(a) and Fig. 4-8(b). These two images are taken by simply switching detection mode from cathodoluminescent detection to scattering electron detection under the same magnification condition and thus have one to one location correspondence. The CL intensity changes dramatically across SiO_2 passivation boundary. The bright CL spots are mostly located at the regrown GaN right on top of SiO_2 passivation masks. The intensity of bright CL spot is so high that when it is adjusted not to saturate detector, the CL intensity difference between lower GaN layer and sapphire become visually hard to distinguish. By analyzing the gray scale levels of image pixels, we can still identify GaN-sapphire interface, which is also confirmed by comparing Fig. 4-8(a) and Fig. 4-8(b). The CL intensity averaged over the cross section area of the regrown layer is measured to be about 23 times of that of the layer below passivation boundary. The threading dislocation defects are strong non-radiative recombination centers [12]. The significant increase in CL intensity demonstrates that the loss of excited carriers due to non-radiative recombination is greatly reduced in the defect passivated layer as a result of the reduction in TD density.

LED chips with size of 300×300 μm^2 were fabricated from the defect passivated epi-wafer. The optical and electrical characteristics are compared with a reference LED going through the same fabrication process except for the defect passivation layer. The light current (L-I) and voltage current (V-I) curves of the defect passivated LED (DP-LED) and reference LED (R-LED) are shown in Fig. 4.9. The driving voltage of DP-LED (red solid line) is slightly lower than that (black dotted line) of R-LED. We remark that this slightly lower driving voltage may be due to the lower defect density. When the defect density is lower, electrons are easier to move across material without scattering thus leading to lower resistance and driving voltage. The optical output power is however significantly enhanced by 45% compared to that of the reference sample at 20 mA. The SiO_2 masks not only block the propagation of TD but also can act as light scattering sites to improve LED light extraction efficiency, similar to the use of patterned GaN-sapphire interface [13, 14] to reduce light trapped by total internal reflection. Fig. 4.10 shows the reverse voltage versus current characteristics of DP-LED and R-LED. To examine the leakage current of both LED devices under reverse bias voltage. The leakage current of R-LED and DP-LED were 10.6 nA and 6.2 nA at -10 V, respectively. The much smaller leakage current might induced from better crystal quality for LED regrowth on substrate with DP structure.

A Monte Carlo ray tracing simulation is used to check if light extraction enhancement is a significant part of total output power enhancement. A simplified 2D array of inverted hexagonal pyramid SiO_2

masks is used to model the defect passivation. Various geometries with 0.7-1μm lateral size, 0.5-1μm height, and 3-4 μm center to center spacing are calculated and show a variation of light extraction enhancement from 10-25%. In real device, both the size and spacing have random distributions. This is only a coarse estimate. Nevertheless, the calculation shows that light extraction enhancement cannot be totally neglected in the total 45% output power enhancement. The output power enhancement from TD defect reduction is not as large as the above measured CL intensity enhancement. It has been reported that InGaN quantum well emission is less sensitive to TD defects. It was remarked that the excited carriers are effectively localized by potential minima created by In composition fluctuations in InGaN QWs to form excitons before they are depleted by TD non-radiative recombination centers [15, 16]. LEDs with InGaN QWs are therefore less sensitive to TD density. LEDs using GaN or AlGaN active layer is however very sensitive to TD defects and really requires the reduction of TD [15, 16].

In summary, we have demonstrated a defect selective passivation method to reduce TD density and used it to fabricate a LED. The defect passivation SiO_2 masks are self-aligned to the TD defect pits created by KOH defect selective etching without photolithography patterning and can significantly reduce TD density from $1x10^9$ to $4x10^7$ cm^{-2}. The SiO_2 masks also improve the light extraction efficiency in LED application. TEM image shows that some defects are resistive to KOH etching and propagate all the way to the top surface. Further improvement can be made by exploring additional etching chemicals that are complementary

to KOH in defect selective etching to increase the coverage rate of defect selective passivation.

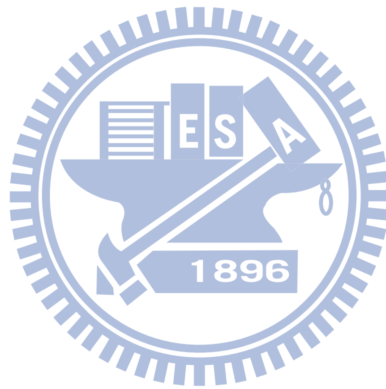

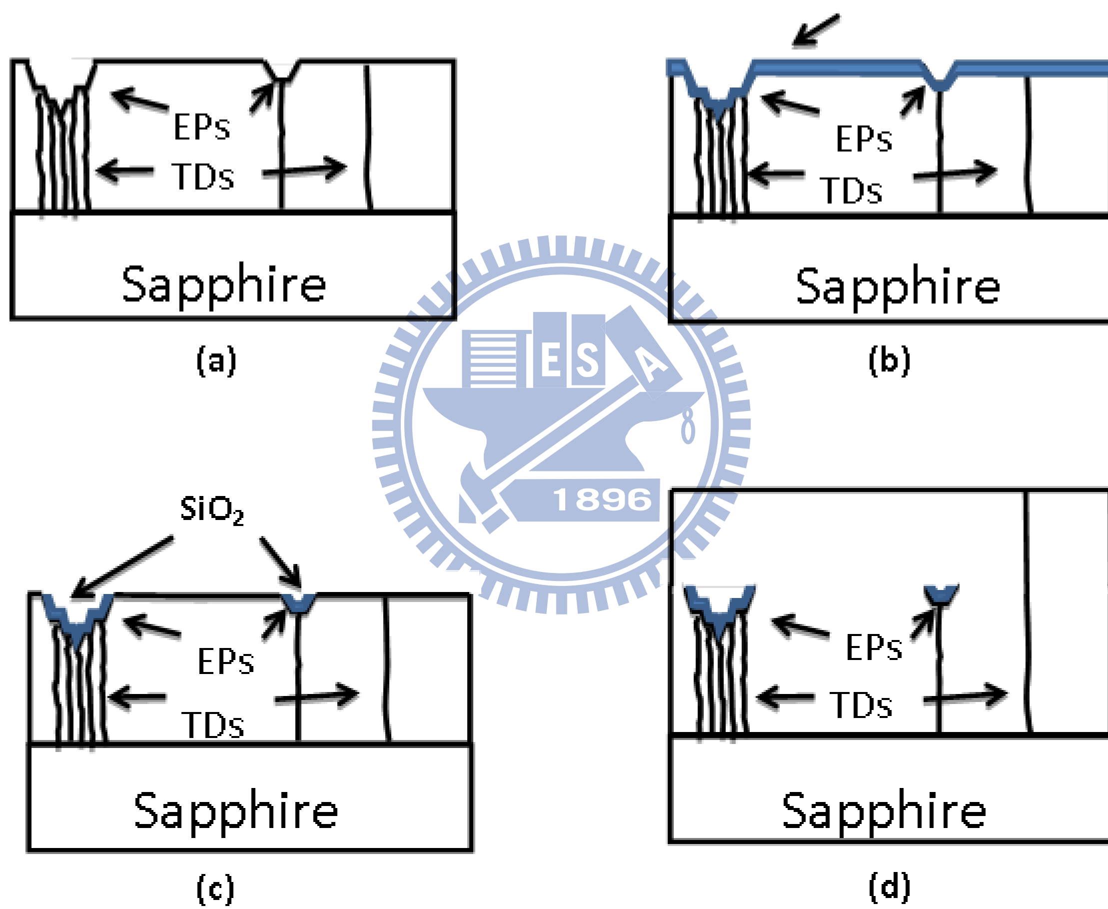

Fig. 4.1 Defect selective passivation process flow

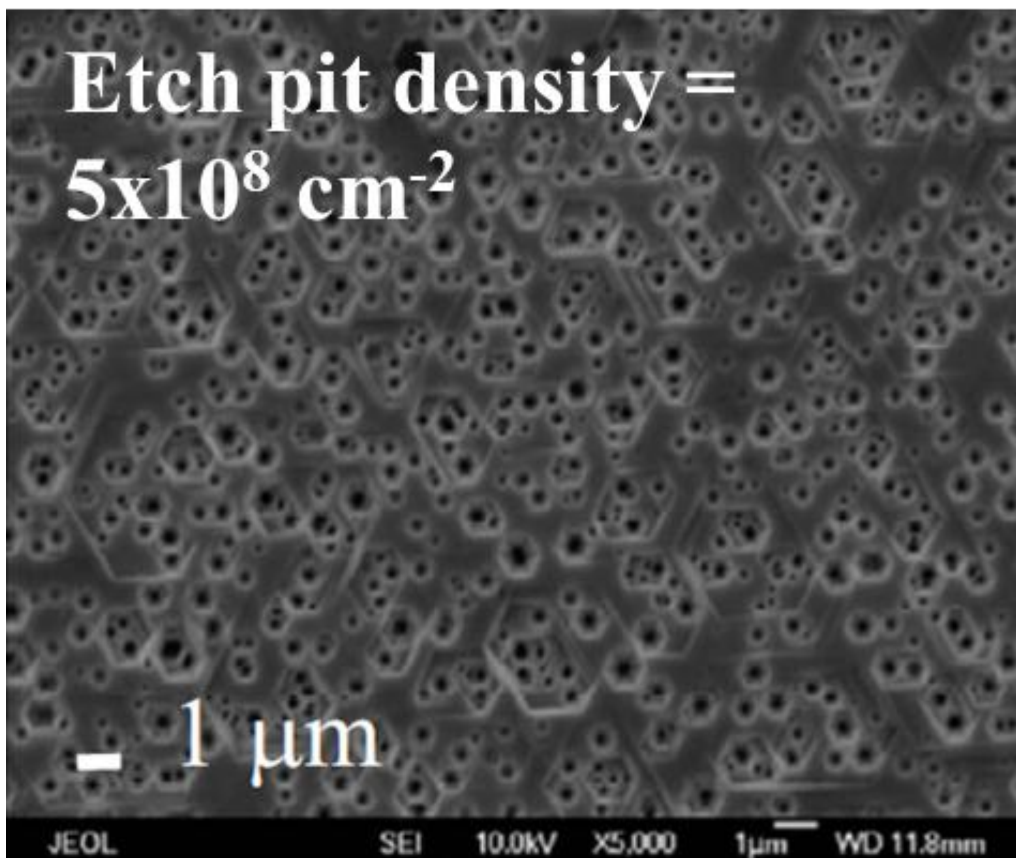

Fig. 4.2 Top-view SEM image of the grown sample surface morphology after high temperature KOH etching process.

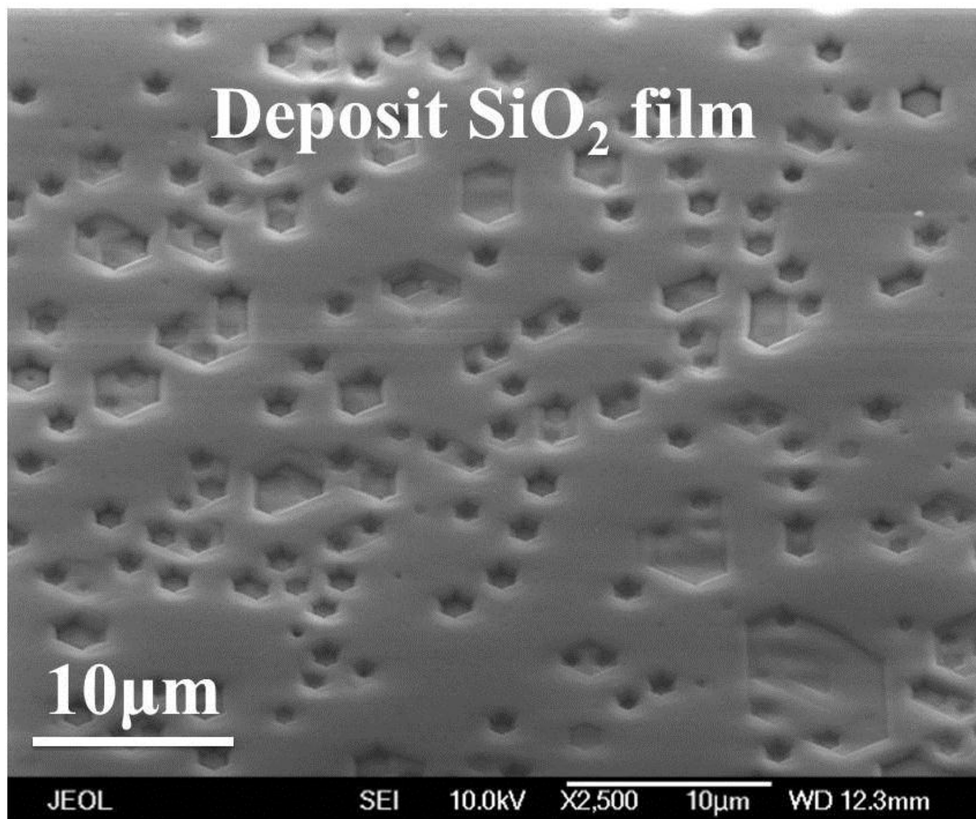

Fig. 4.3 Top-view SEM image of etched sample after deposit SiO2 film process.

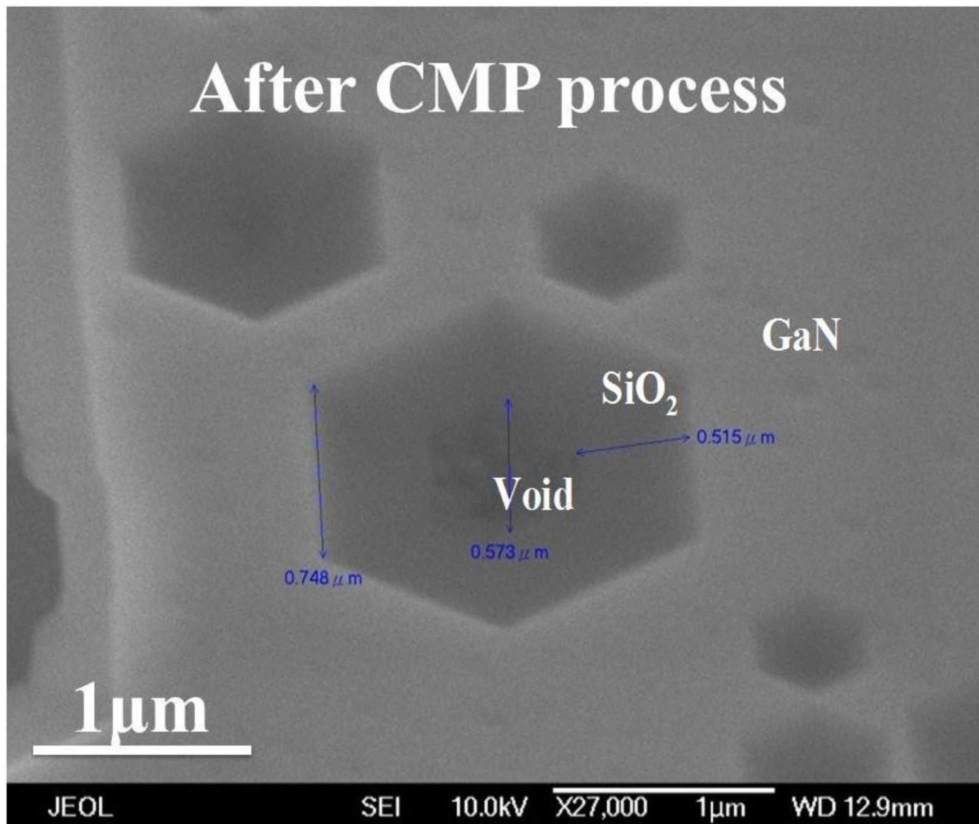

Fig. 4.4 Top-view SEM image of etched sample with SiO_2 film morphology after CMP process.

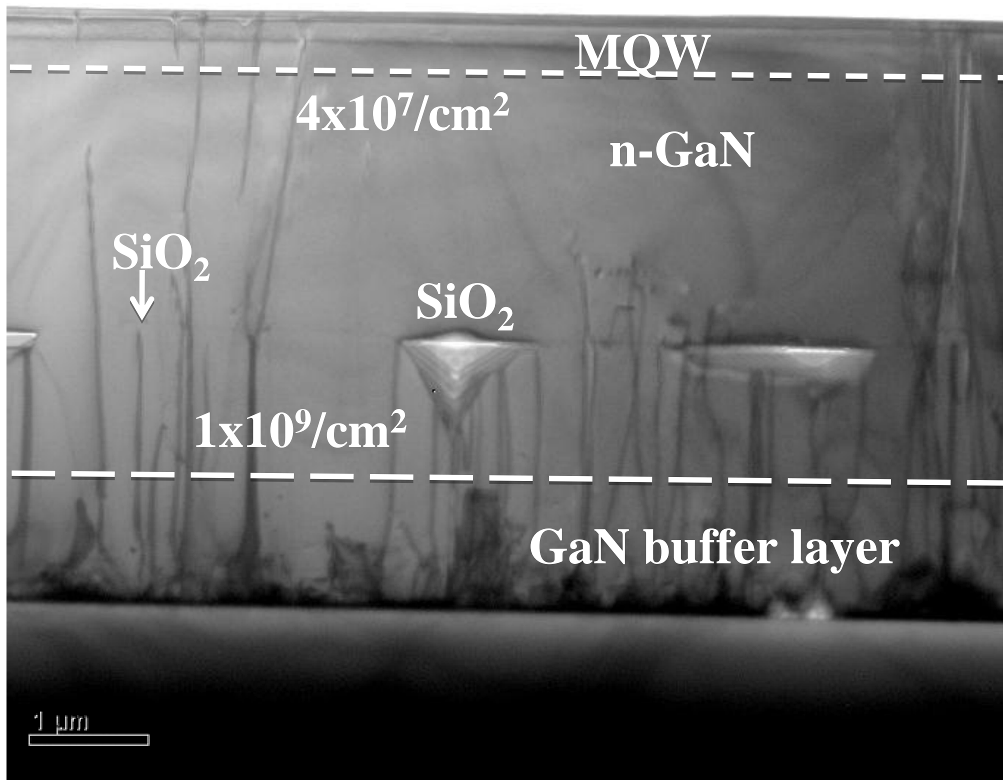

Fig. 4.5 TEM image of LED sample with defect selective passivation.

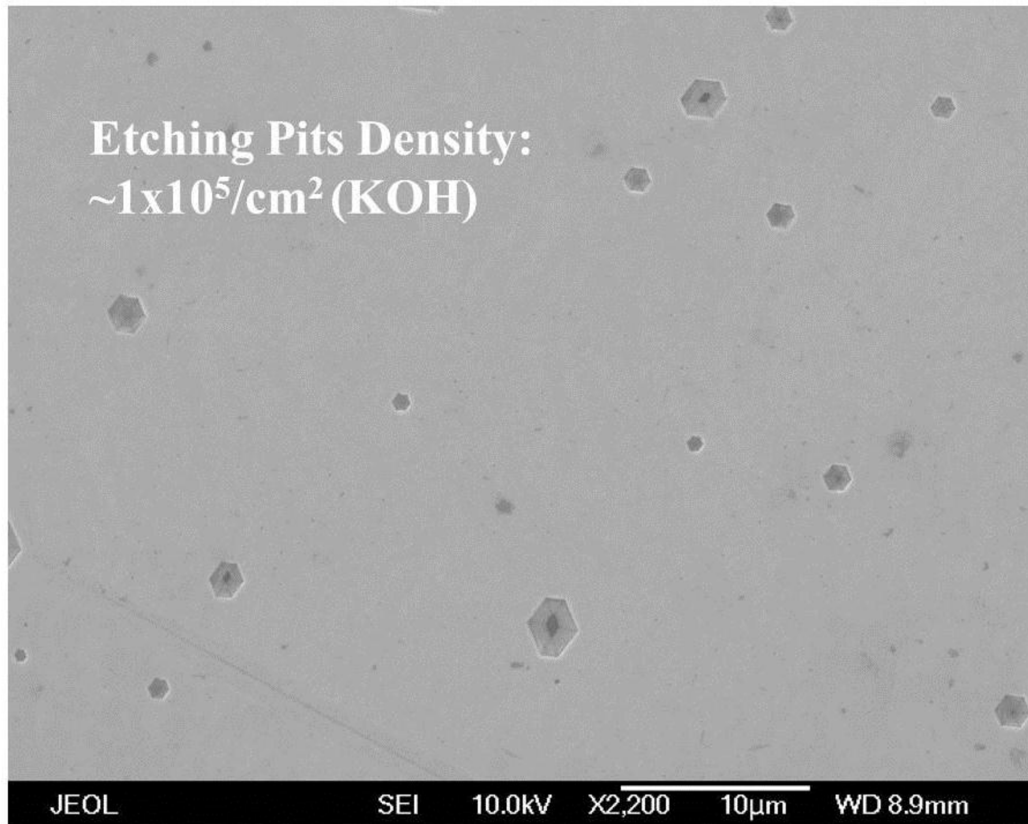

Fig. 4.6 SEM image of the defect passivated sample after molten KOH etching

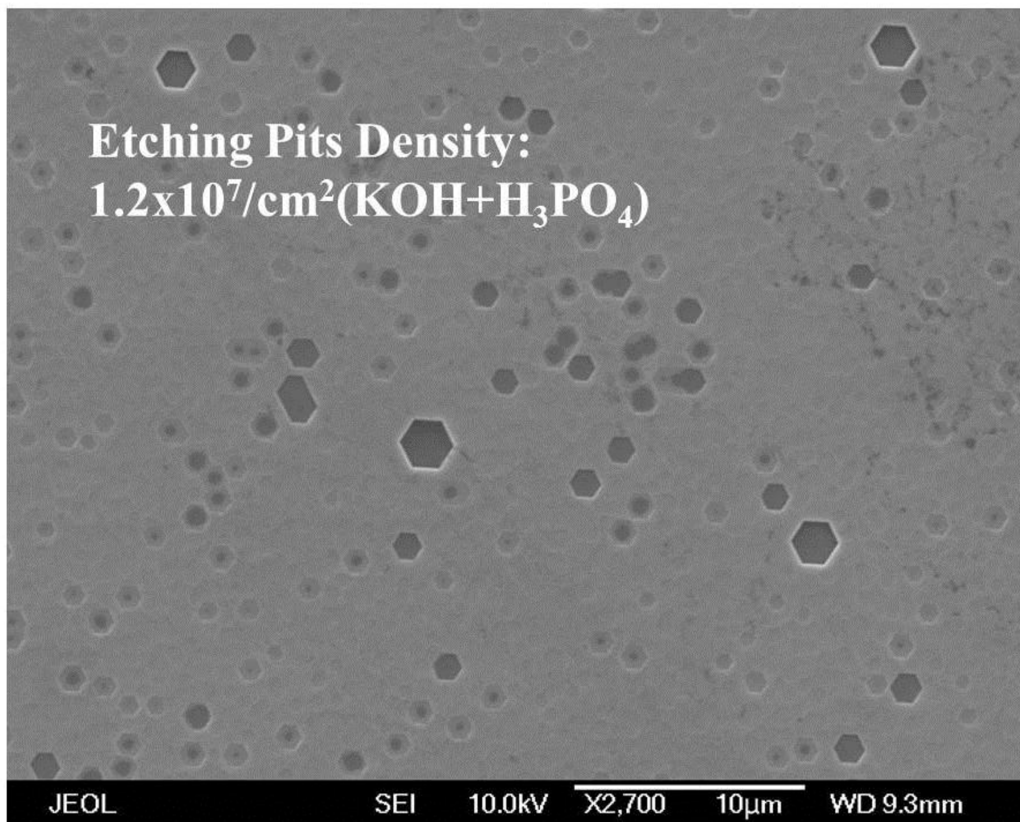

Fig. 4.7 SEM image of the defect passivated sample after high temperature H_3PO_4 etching

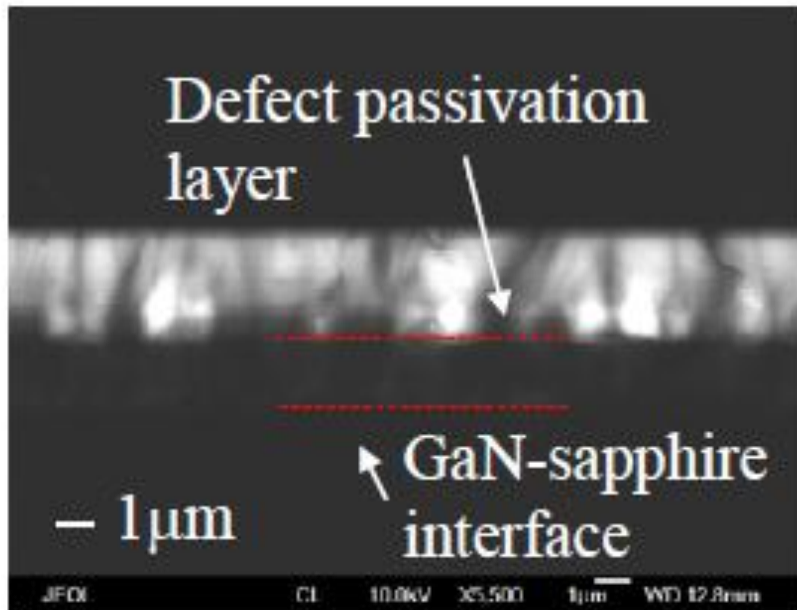

(a)

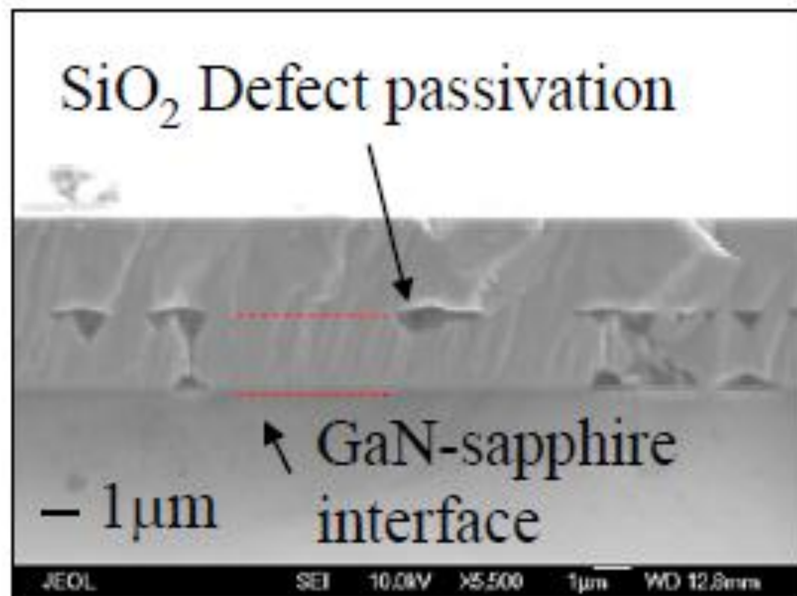

(b)

Fig. 4.8 Cross section CL (a) and SEM image (b) of the defect passivated epi-wafer under same magnification

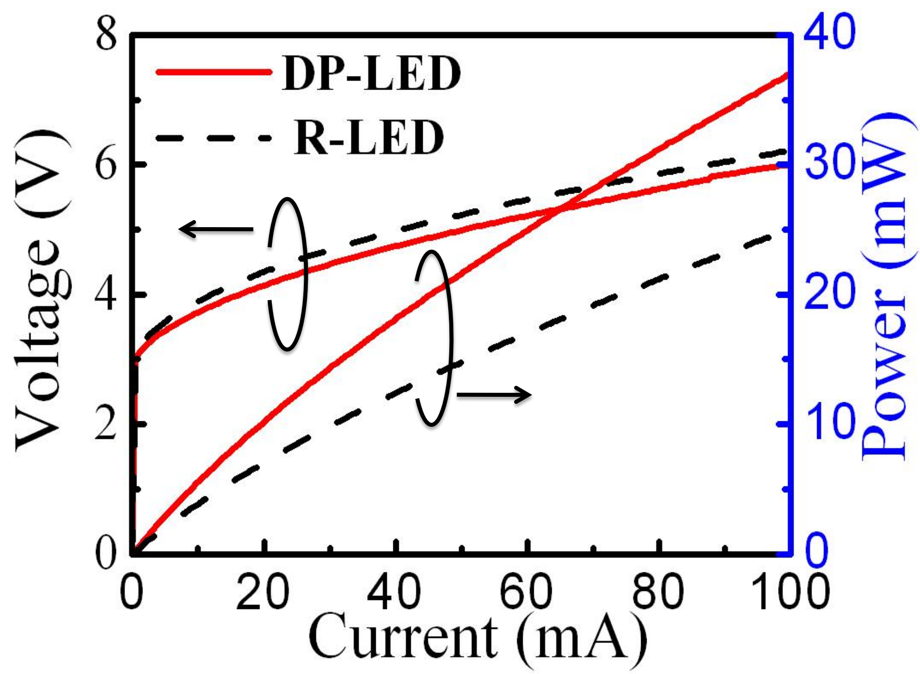

Fig. 4.9 L-I and V-I curve of the DP-LED and R-LED

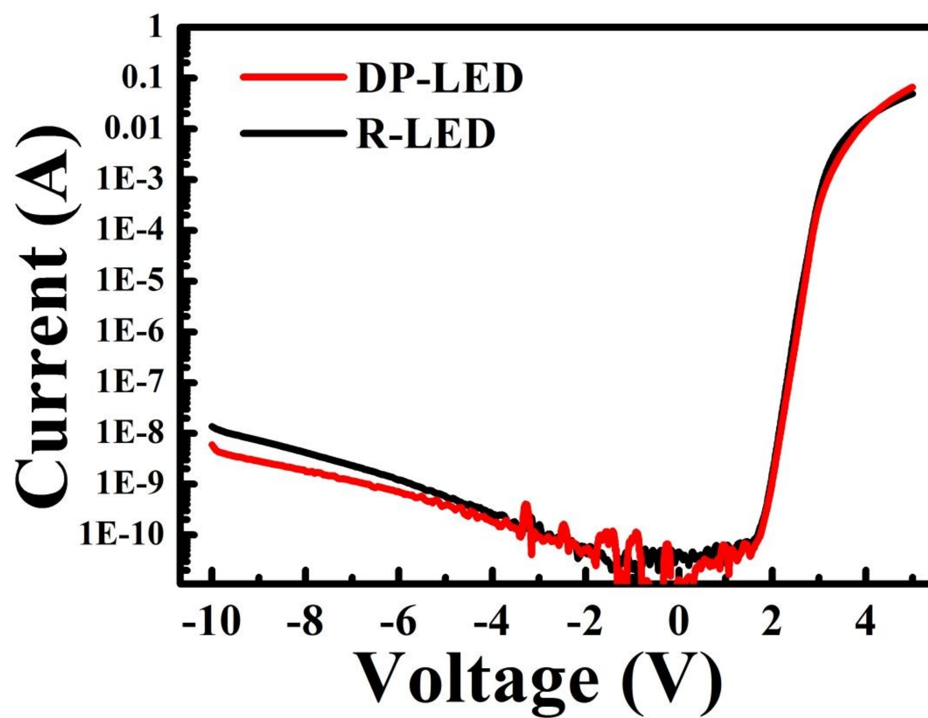

Fig. 4.10 The reverse voltage versus current characteristics of DP-LED and R-LED

References

[1]. T. Mukai, K. Takekawa, and S. Nakamura, Jpn. J. Appl. Phys., Part 2 **37**, L839 (1998).

[2]. O.-H. Nam, M. D. Bremser, T. S. Zheleva, and R. F. Davis, Appl. Phys. Lett. **71**, 2638 (1997).

[3]. Eun-Hyun Park, Jin Jang,1 Shalini Gupta, Ian Ferguson, Cheol-Hoi Kim, Soo-Kun Jeon, and Joong-Seo Park, Appl. Phys. Lett. **73,** 1688 (2008).

[4]. Y. J. Lee, H. C. Kuo, T. C. Lu, B. J. Su, and S. C. Wang, Journal of The Electrochemical Society, **153,** G1106 (2006).

[5]. J. Xie, Ü. Ö zgür, Y. Fu, X. Ni, H. Morkoç, C. K. Inoki, T. S. Kuan, J. V. Foreman, H. O. Everitt, Appl. Phys. Lett. **90**, 041107 (2007).

[6]. Ü. Ö zgür, Y. Fu, Y. T. Moon, F. Yun, H. Morkoç, H. O. Everitt, S. S. Park and K. Y. Lee, Appl. Phys. Lett. **86**, 232106 (2005).

[7]. J. W. Lee, C. Sone, Y. Park, S.-N. Lee, J.-H. Ryou, R. D. Dupuis, C.-H. Hong, and H. Kim, Appl. Phys. Lett. **95**, 011108 (2009).

[8]. J. L. Weyher, H. Ashraf, and P. R. Hageman, Appl. Phys. Lett. **95**, 031913 (2009).

[9]. Takahiro Kozawa, Tetsu Kachi, Takeshi Ohwaki, Yasunori Taga, Norikatsu Koide and Masayoshi Koike, J. Electrochem. Soc., **143**, L17 (1996).

[10]. Lu Min, Chang Xin, Fang Hui-Zhi,Yang Zhi-Jian, Yang Hua, Li Zi-Lan, Ren Qian, Zhang Guo-Yi, and Zhang Bei, Phys. Stat. Sol. (c) **1**, 2438 (2004).

[11]. D. A. Stocker, E. F. Schubert and J. M. Redwing, Appl. Phys. Lett. **73**, 2654 (1998).

[12]. M. Albrecht, J. L. Weyher, B. Lucznik, I. Grzegory, and S. Porowski, Appl. Phys. Lett. **92**, 231909 (2008).

[13]. K. Tadatomo, H. Okagawa, Y. Ohuchi, T. Tsunekawa, Y. Imada, M. Kato, and T. Taguchi, Jpn. J. Appl. Phys., Part 2 **40**, L583 (2001).

[14]. Eun-Hyun Park, Jin Jang, Shalini Gupta, Ian Ferguson, Cheol-Hoi Kim, Soo-Kun Jeon, and Joong-Seo Park, Appl. Phys. Lett. **93,** 191103 (2008).

[15]. T. Mukai, D. Morita, S. Nakamura, J. Crystal Growth **189/190**, 778 (1998).

[16]. S. Nakamura, Science, **281**, 956, (1998).

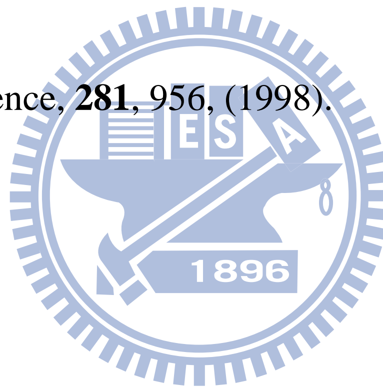

Chapter 5 High Efficiency light emitting diodes with Anisotropically Etched GaN-sapphire Interface and Mechanical Lift-off Technique

5.1 High Efficiency light emitting diode with inverted pyramid structure

5.1.1 The progress of high extraction efficiency GaN LEDs

GaN-based light emitting diode (LED) has attracted great attention in last few years due to its importance in solid state lighting applications. Researchers are actively investigating various approaches to improve output efficiency. Among those factors affecting output efficiency, material defect density and light extraction efficiency are two important problems. The GaN-based devices are often epitaxially grown on sapphire. The as grown GaN epitaxial layer has high crystal dislocation density, typically in the range of 10^{8-10} cm^{-2}. These crystal defects are detrimental to optoelectronic device performance. The high refractive index of GaN restricts the escape angle of emitting light and results in low light extraction efficiency. There have been great efforts in solving these two problems. While the improvement in defect density has been slow, the light extraction efficiency has experienced rapid progress. Various surface texture [1-3], photonic crystal structure [4-5], and patterned substrate [6-8] methods have been investigated and demonstrated significant light extraction enhancement. Recently, patterned sapphire substrate with chemical wet etching in between epitaxial growth steps has provided another way to improve light extraction efficiency [9-10]. A common feature in all these different methods is having large surface variations at the GaN-air or GaN-sapphire interface. The fabrication process often involves micro

lithography and etching.

In this section, we report an innovative fabrication process that can significantly improves both the light extraction efficiency and crystal quality without the need of photolithography substrate patterning. The fabricated UV LEDs have inverted pyramid structures throughout the GaN-sapphire interface. The pyramid structures are created by anisotropic chemical wet etching of GaN at sapphire interface. The chemical etching agent reaches GaN-sapphire interface through channels self-assembled by defect selective etching from top surface. The pyramid structures help to redirect light to the front emitting surface and at the same time also partially relieves the strain in GaN, which in turn reduces dislocation defects.

5.1.2 Fabrication of high efficiency light emitting diodes with inverted pyramid structure

The material epitaxial growth uses nominal low pressure metalorganic chemical vapor deposition (MOCVD). A 30 nm of low temperature GaN nucleation layer followed by a 2.5 μm GaN buffer layer was grown on (0001) sapphire template. The GaN wafer was then immersed in high temperature molten KOH at 350°C for 12 minutes. The molten KOH selectively etched defect sites on GaN wafer surface and etched continuously downward opening up channels to sapphire interface. The molten KOH was led to GaN-sapphire interface through these self-assembled channel openings. The etching process then turned into lateral direction because the defect density was high at interface and etched away a thin layer of GaN along sapphire interface. Additional GaN was grown on the etched GaN wafer by MOCVD to fill up both the etched vertical openings and hexagonal surface pits to provide flat top surface for the subsequent LED device growth. The LED device structure

was 3.5 um n-doped GaN, 10 pairs of $Al_{0.05}Ga_{0.95}N$/InGaN quantum wells (13 nm/2.5 nm), and 100 nm of p-doped GaN cap layer. The designed quantum well emission wavelength was at 394 nm. The process flowchart of chemical wet etching and regrowth are shown in Fig. 5.1 .It is known that KOH etching is typically anisotropic and preferentially etches specific crystallographic planes. A tilted view SEM image is shown in Fig. 5.2, where the inverted pyramid structure at GaN-sapphire interface can be seen from an etched large opening. A large number of hexagonal pits were also formed on the top surface. The etch pit density was $\sim 5\times 10^8$ cm^{-2} from SEM image estimation. A cross section SEM image of a cleaved sample after regrowth process is shown in Fig. 5.3. The space and the inverted pyramid structures created at the GaN-sapphire interface are still well maintained and distributed throughout large area as shown in the zoom out Fig. 5.4. Most of the pyramid tips are still in contact with sapphire. To investigate the performance of the device structure and make fair comparisons, a reference wafer also went through exactly the same fabrication process except for skipping the KOH etching step

5.1.3 Characteristic of Inverted Pyramid LEDs

The X-ray diffraction (XRD) rocking curves of these two samples are shown in Fig. 5.5. The linewidth for (102) planes was reduced from 552 to 472 arcseconds. The linewidth for (002) planes was only reduced from 338 to 335 arcseconds. The XRD linewidths for (102) and (002) planes are respectively related to edge and screw threading dislocation densities [11]. The decrease in XRD linewidth indicates improved material quality. The improvement is attributed to the strain relaxation of the partially relieved GaN layer by interfacial etching and the subsequent regrowth. When the initial GaN epitaxial layer was grown on sapphire, a compressive strain was built up in the material due to the mismatched

lattice constants and thermal expansion coefficients between GaN and sapphire. The KOH interfacial etching partially relieved GaN from sapphire interface and relaxed the compressive strain. This partially relieved layer served as a template for subsequent regrowth. It acted as a buffer layer to partially reduce the problems of mismatched lattice constants and thermal expansion coefficients during MOCVD regrowth and eventually led to improved crystal quality. We also employed the AFM to examine the surface morphology after UVLED was regrowth on IP GaN substrate as shown in Fig. 5.6. The root mean square (rms.) value of flatness was 0.924 nm, which demonstrates the IP structure, would not be destroyed the flatness of UVLED. These two samples were made into LED chips. Indium–tin oxide (ITO) was used as a current spreading layer and Ni/Au as a p-type electrode contact. Ti/Al/Ni/Au was deposited on the exposed n-GaN to serve as an n-type electrode contact. The sapphire substrates of both samples were lapped down and a 240 nm Al metal reflector coating was deposited on the sapphire back surface. The use of back reflector is a common design in finished LED package to reflect light into front surface direction. Therefore, it was also used in the comparison between these two samples. They were finally scribed into 350×350 μm^2 UV LED chips. The schematic of the LED with inverted micro pyramid structures (IP-LED) is shown in Fig. 5.7. The reference LED (R-LED) has similar structure except for a flat GaN-sapphire interface. The fabricated LED chips were mounted on TO-14 cans without capping epoxy. The electroluminescence (EL) spectra of both LEDs collected in the normal to the front surface direction are shown in Fig. 5.8. The peak intensity of IP-LED is enhanced by 112% compared to that of R-LED. The EL spectrum of R-LED shows slight Fabry-Perot mode ripples. The Fabry-Perot modes are formed by the top GaN-air and

bottom GaN-sapphire interfaces. The Fabry-Perot mode spacing is about 5 nm, which is consistent with the overall thickness of 6 μm and GaN refractive index of ~2.55 at 394 nm. The EL spectrum of IP-LED on the other hand does not have the same Fabry-Perot mode ripples. This is because the randomly distributed surfaces of micro pyramid structures suppress the standing wave formation between the top and bottom interfaces. It is also worth to note that the peak wavelength of IP-LED is red shifted by ~2 nm compared to that of R-LED. The red shift in peak emission wavelength indicates the relaxation of compressive strain in IP-LED [12], in consistent with the description in last paragraph for the improved crystal quality.

The light-current (L-I) and voltage-current (V-I) characteristics are shown in Fig. 5.9. The forward voltages of IP-LED and R-LED are respectively 3.86 and 3.80 V at 20 mA and increase to 5.09 and 4.93 V at 100 mA. The electric characteristic of IP-LED is still reasonably well maintained after chemical etching and regrowth process. Fig. 5.10 shows the reverse voltage versus current characteristics of IP-LED and R-LED. To examine the leakage current of both UV LED devices under reverse bias voltage. The leakage current of R-LED and IP-LED were 7.2 nA and 1.4 nA at -5 V, respectively. The much smaller leakage current might induced from better crystal quality for UVLED regrowth on substrate with IP structure.

The optical power was collected by an integrating sphere. The optical power of IP-LED and R-LED are respectively 7.31 and 3.95mW at 20mA and 37.5 and 23.7mW at 100mA. Compared to R-LED, the IP-LED output power exhibits 85% and 58% enhancement at 20 and 100 mA, respectively. The decrease of output power enhancement is likely due to

the lower thermal conductance of the small contacts between the inverted pyramids and sapphire interface. The small interface contacts on the other hand are crucial for relieving the compressive strain and reducing material defects as described previously, which in turn reduces heat generation. The low thermal conductance problem is therefore not as serious as it would be. When contacts are infinitesimally small, the epi-layer can be bonded with p-side down to a better thermal/electrical conductive substrate, for example Si, and be easily removed from sapphire by mechanical force. The low heat conductance of pyramid tip contact is then no longer a problem. We also measure the three-dimension far field pattern of IP-LED and R-LED at a 20 mA operating currents as show in the Fig. 5.11. It could be obviously observed that the IP-LED emission intensity have better distribution in the normal direction. This was suggesting that the guiding light (excess the total reflective angular) in GaN would be redirected by reflection in the inverted pyramid GaN/air interface with high difference refractive index. We plot the two-dimension far field pattern at 20 mA injection current as shown in Fig. 5.12. The IP-LED emission in normal direction is much more enhanced. The emission intensity is enhanced by 120% in normal direction and 62% in 45 degree direction. The divergent angles of IP-LED and R-LED are 108 and 128 degrees, respectively.

5.1.4 Prediction of light extraction efficiency of IP-LED by ray trace simulation

To obtain a better physical understanding of output power improvement, ray tracing simulations based on Monte Carlo method are carried out for both LEDs. There is a distribution of pyramid heights since the etching process has some degrees of randomness. The pyramid facet angle is however fairly well defined as can be seen from the SEM

cross section image Fig. 5.3. To simplify the calculation, an averaged pyramid height of 1 μm and 58^0 facet angle with respect to sapphire surface were used in simulation. This model is not exact but is believed to be close enough to provide reasonable estimates. Fig. 5.13(a) and Fig. 5. 13(b) are the ray tracing results near GaN-sapphire interface for two LEDs. The inverted pyramid structures indeed effectively increase light output in the front surface direction. The light extraction efficiencies versus various pyramid heights are also calculated as shown in Fig. 5.14. The calculated 72% enhancement at 1μm pyramid height accounts for the major part of the observed 85% total power enhancement. The other 13% enhancement can be attributed to internal quantum efficiency improvement due to better crystal quality in IP-LED. The simulation also shows that light extraction enhancement for 1μm pyramid height is close to the optimum enhancement value.

In conclusion, we have demonstrated a high efficiency UV LED with inverted micro pyramid structures at GaN-sapphire interface. The micro pyramid structures were created by interfacial anisotropic chemical wet etching without the need of photolithography patterning. The UV LED was fabricated by growth interrupt, chemical etching, and regrowth processes. The device electrical performance is well maintained after these steps. The overall optical output power has shown significant 85% enhancement at nominal operating current 20 mA, which is attributed to both improved crystal quality and better light extraction efficiency.

5.2 Vertical type thin GaN LED with hexagonal inverted pyramid by means of the mechanical lift-off

5.2.1 The background of lift-off process in vertical type GaN LED

Gallium nitride based materials have recently attracted considerable

attention all over the world due to their potential applications in the optoelectronic devices, such as light emitting diodes (LEDs) and laser diodes [13-15]. These devices were grown heteroepitaxially onto foreign substrates such as sapphire and SiC due to lack of high quality GaN substrates. The sapphire is the most commonly used substrate because of its relatively low cost, but it on the other hand limits the devices performance due to its poor electrical and thermal conductivity. During the last decade of years, the techniques of the laser lift-off (LLO) [16,17] and the chemical lift-off (CLO) which use a CrN layer [18], a ZnO layer [19], and a Si-doping n-GaN layer [20] as the sacrificial layer have been adopted to fabricate the freestanding GaN membrane and the vertical LEDs for high performance optoelectronic devices. However, the LLO may induce some issues by placing it under high temperature in the local area and strain release during the process. And even though the CLO can prevent the GaN layer from the laser damage during the laser lift-off process, but it's difficult to keep the etching uniformity and the crystal quality spontaneously.

In this work, we announce the fabrication of mechanical lift-off high quality thin GaN with Inverted Pyramid (IP) structures as a sacrificial layer for vertical LEDs. The interface morphologies and the optical properties of lifted off GaN epilayer will be analyzed in the following sections.

5.2.2 Fabrication of vertical type LED with inverted pyramid structure

The GaN-based epilayer and LED structure used in this study were all prepared by metal–organic chemical vapor deposition (MOCVD). We first deposited a 3 μm-thick un-doped GaN on a c-plane sapphire

substrate as a template. The GaN epilayer was observed to be etched in the molten KOH for 10 mins at high temperature of 350°C. The Inverted Pyramid (IP) GaN/air structure was formed by the reversed etching from the N-face GaN. The etched path along with the threading dislocation propagation form the GaN top surface to the interface of GaN and sapphire, and the related processes have been presented in our previous study [21].

Next, the GaN-based LED structures were grown on IP GaN/air template in the lateral re-growth process. The LED device structure was 2 μm un-doped GaN, 3.5 μm n-doped GaN, ten pairs of $Al_{0.02}Ga_{0.98}N/In_{0.1}Ga_{0.9}N$ quantum wells 13/2.5 nm, and 100 nm of p-doped GaN cap layer. The designed emission wavelength is measured at approximately 405 nm. After Ni/Au p-GaN contact layer was deposited on the p-GaN layer in the E-gun process, which was followed by a 2 mins annealing process to accomplish a low-resistance contact. The annealing temperature was 500°C in ambient air. After annealing process, a reflective layer of 1500 Å Al was deposited to prevent light from reaching the absorbing Si substrate. In this way, a metalized Ni/Au bonding layer was deposited on the top of the Al layer. The thicknesses of Ni and that of Au layer were 1500 and 2000 Å, respectively. This 1500 Å Ni layer serves as an adhesive barrier layer while the 2000 Å Au layer serves as the seed layer in the electroplating process of 2μm thick Au layer which is used to do Au-Si wafer bonding.

In the Au-Si wafer bonding process, GaN thin film with IP structure and sapphire substrate were under 400°C. GaN thin film will carry

high-level thermal stress under this condition, and it will separate from sapphire substrate during cooling process because of different thermal expansive coefficient (CTE). This prominent CTE mismatch with GaN and sapphire brings an unbearable shear stress to the interface and as well makes the IP structure break off. Therefore, the sapphire substrate can be removed simultaneously by way of this mechanical lift-off technique and follows the process of vertical-LED (V-LED). The entire process of flowchart and thin GaN structure is shown in Fig. 5.15.

5.2.3 Characteristic of thin GaN LED with IP structure

The cleaved sample, which is titled to be examined under the scanning electron microscopy (SEM) after wet etching process, is shown in Fig. 5.16(a), where the IP structure at GaN/sapphire interface can be clearly observed and the V-shaped hexagonal pits of about 2×10^{7} cm^{-2} were also formed on the surface. Additional GaN was grown on the etched GaN wafer to fill up both the etched openings and surface pits to provide a flat top surface for the subsequent LED device growth. Fig. 5.16(b) reveals the cross-sectional SEM image of the GaN-based LED sample at the GaN/sapphire interface in the re-growth process. It was discovered that the IP structures were still complete and some air voids were also found in the IP structures. This result indicates that the vertical etched path was effectively hindered by means of the lateral overgrowth. Fig. 5.16(c) illustrates the cross-sectional transmission electron microscopy (TEM) image of the GaN-based LED sample with the white lines indicating the re-growth boundary of the GaN epilayer regions. The formation of air void usually observed in the etching boundary during the lateral re-growth process. The dislocation density at the bottom of the GaN layer is rendered at about 2×10^{9} cm^{-2} and slightly reduces to 1×10^{8} cm^{-2} at the top of the GaN layer. The density of dislocations degrades due

to bending and a half loop of threading dislocations at the re-growth boundary. Most dislocations associate with each other by bending and loop formation, and they do not extend to the top surface as we can observe in Fig. 5.16(d).

Fig. 5.17(a) unveils the cross-sectional SEM image of the vertical LED structure after mechanical lift-off GaN LED/Silicon from the sapphire substrate at high temperature in the wafer bonding process. The inset in Fig. 5.17(a) reveals a top-view SEM image of the IP surface morphology. Obviously, the cone shape structure and etched path were formed on the GaN surface in this sample. The size and density of etch cone shape estimated from SEM were 0.5 μm ~ 1 μm and 8×10^{7} /cm^{2}, respectively. Accordingly, the etched paths were created throughout the GaN/sapphire interface and the GaN epilayer which is partially attached to the sapphire substrate. Therefore, the mechanical lift-off process was proved to be available by regarding the IP structures as a sacrificial layer at high temperature during the wafer bonding process. We also employed the AFM to examine the backside morphology after V-LED was mechanical lift-off. The root mean square (rms.) value of flatness was 122.5 nm, and the morphology after lift-off as shown in Fig. 5.18. The IP structure was remained as observed in right hand image in Fig. 5.17, the enormous hexagonal structure were corresponding to what we expect in IP V-LED. Fig. 5.19 shows the room temperature Raman spectrum of the GaN epilayer re-growth on IP structure and mechanical lift-off by IP structure. The Raman shift peak of E_2 (high) for the GaN epilayer re-growth on IP structure and mechanical lift-off by IP structure were

located at around 567.82 and 567.11 cm^{-1}, respectively. We can obtain the strain value of GaN epilayer with the following equation [22].

$$\Delta\omega = \omega_{E_2} - \omega_0 = C \cdot \sigma_{xx} \quad (5.2\text{-}1)$$

$$\sigma_{xx} = M_f \cdot \varepsilon_{xx} \quad (5.2\text{-}2)$$

$$\varepsilon_{xx} = \frac{\Delta\omega}{C \cdot M_f} \quad (5.2\text{-}3)$$

As the equation uncovers, $\Delta\omega$ is the Raman shift peak difference between the strained GaN epilayer ω_{E2} and the unstrained GaN epilayer ω_0 (566.5 cm^{-1}). C is the biaxial strain coefficient, which is 2.25 cm^{-1}/GPa. M_f is the biaxial modulus to the substrate, which is 449.6 GPa [23]. σ_{xx} is the biaxial stress, and ε_{xx} is the biaxial strain. The calculated in-plane compressive strain ε_{xx} are approximately 1.30×10^{-3} and 6.03×10^{-4} for the GaN epilayer re-growth on IP structure and mechanical lift-off by HIP structure, respectively. The Raman shift peak of E_2 (high) for GaN on sapphire without IP structure is 569.5 (cm^{-1}), and the in-plane compressive strain ε_{xx} is about 2.97×10^{-3}. In other words, it implies that the residual stress of GaN-based LED can also be considerably declined while introducing the IP structure to the GaN/sapphire interface. In order to compare the performance of V-LED fabricated by mechanical lift-off with regular LEDs on a sapphire substrate, regular LEDs were also fabricated by applying the same LED structure for reference (Ref-LED) and the same size of 380×380 μm^2. The electroluminescence (EL) spectra of both LEDs collected in the normal to the front surface direction at 20 mA is shown in Fig. 5.20 The peak wavelength of V-LED and that of

Ref-LED are 405 and 406nm, respectively. The inset in Fig. 5.20 shows the variation of LED emission peak wavelength of the V-LED and that of the Ref-LED under high current continuous-wave (cw) operation conditions. The peak wavelength of the Ref-LED showed a relatively larger redshift of about 16 nm from a low current of 20 mA to a high current of 100 mA. However, the peak wavelength of V-LED displayed only a slight redshift of about 5 nm in the same current range, indicating the relief of compressive strain in V-LED. Fig. 5.21 shows the light output power–current–voltage ($L - I - V$) characteristics under cw operation conditions for the V-LED and the Ref-LEDs. The forward voltage of V-LED and that of Ref-LED are 3.38 and 3.65 V, respectively. The light oouput power of the V-LED is higher by 100% than the Ref-LED at 20 mA.

The strain of GaN growth on sapphire or Si substrate to be reduced by air gap structure had been discussed [24,25]. The IP structure partially relieves GaN from sapphire interface so that relieves the compressive strain. This partially relieved layer serves as a template in the subsequent re-growth process. It acted as a transition layer to partially filter the mismatched lattice constant and thermal expansion coefficient problems to improve the crystal quality. Therefore, we speculate that this IP structure will efficiently reduce the stress state on re-growth GaN epilayer, in which the high efficiency vertical LED was demonstrated.

In summary, we have successfully demonstrated the fabrication of mechanical lift-off high quality thin GaN LED with IP structures as a sacrificial layer during wafer bonding process for vertical LEDs. The

density of threading dislocations can be efficiently reduced from 2×10^9 to 1×10^8 cm^{-2} by applying the re-growth GaN epilayer on IP structure. The reduction of dislocation was due to bending and a half loop of threading dislocations at the re-growth boundary. The in-plane compressive strain ε_{xx} are calculated to be about 1.30×10^{-3} and 6.03×10^{-4} for the GaN epilayer re-growth on IP structure and mechanical lift-off by IP structure, respectively. It implies that the residual stress of GaN-based LED can also be greatly reduced while introducing the IP structure to the GaN/sapphire interface. The peak wavelength of the V-LED also shows only a slight redshift of about 5 nm in the spectrum from 20 mA to 100 mA. The result indicates the relief of compressive strain in V-LED. Finally, the overall optical output power has shown significant 100% enhancement under operating current 20 mA with this mechanical lift-off technique for fabrication the vertical-LED.

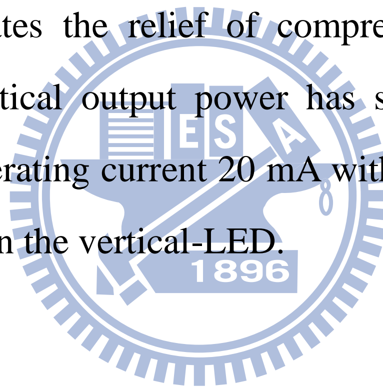

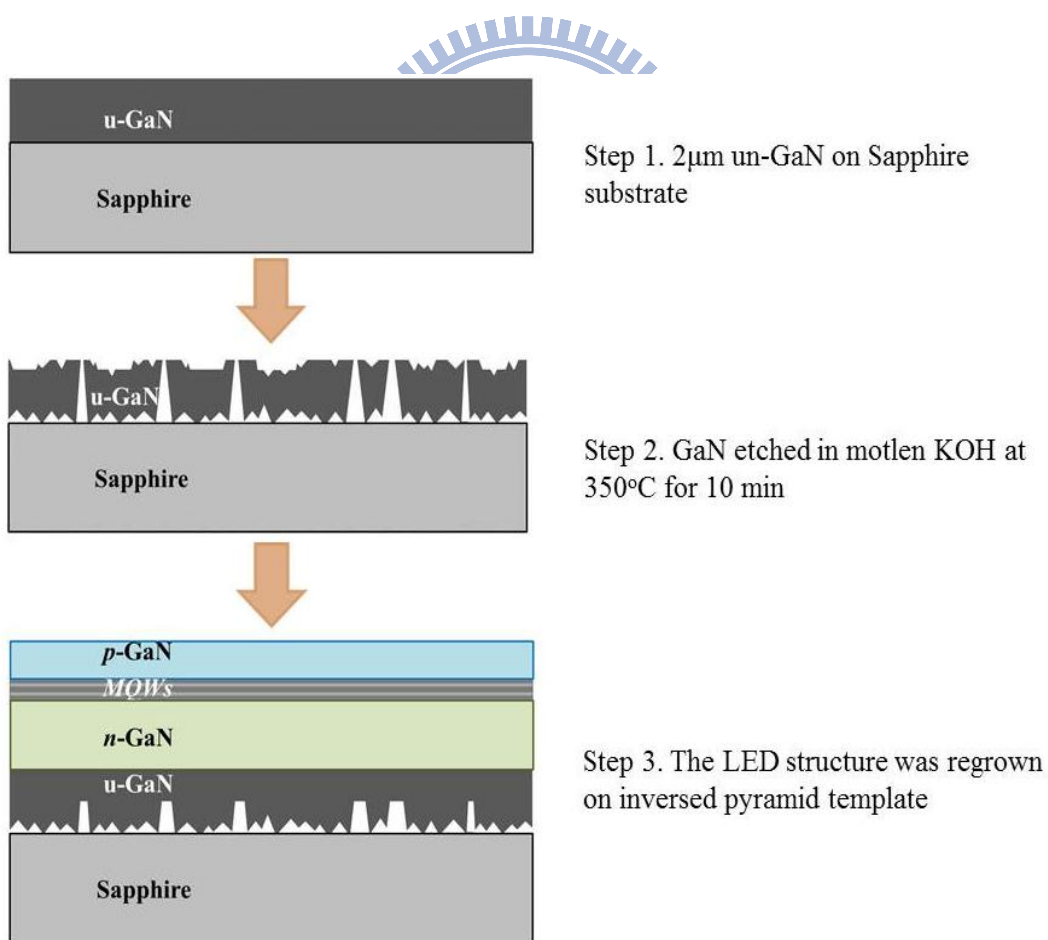

Fig. 5.1 Process flowchart of LED with inverted pyramid structure

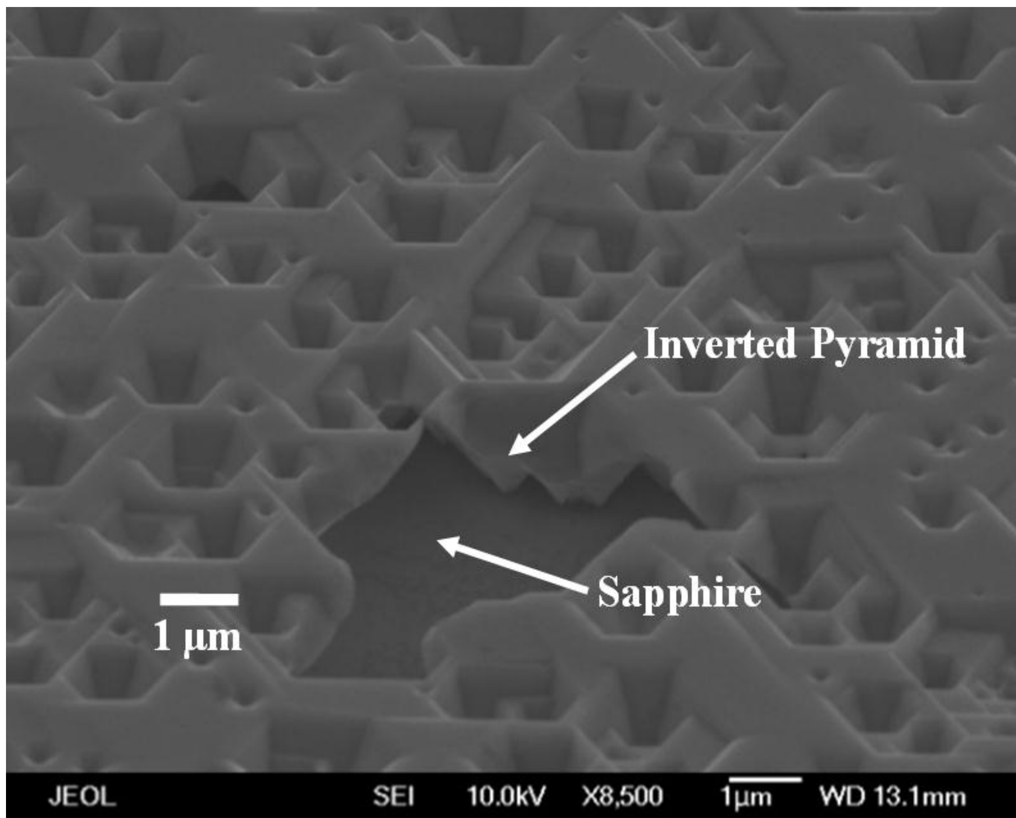

Fig. 5.2 SEM image of the etched GaN surface. The inverted pyramid structures can be seen from the over etched opening holes.

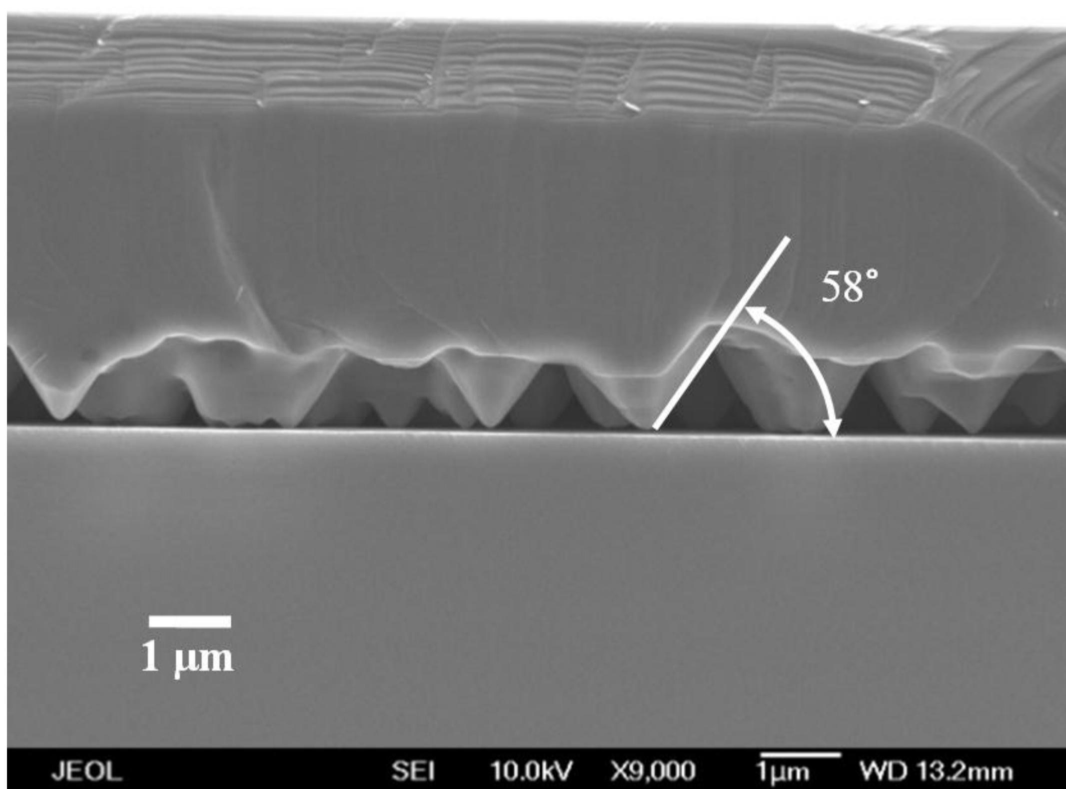

Fig. 5.3 SEM cross section image of the regrown sample

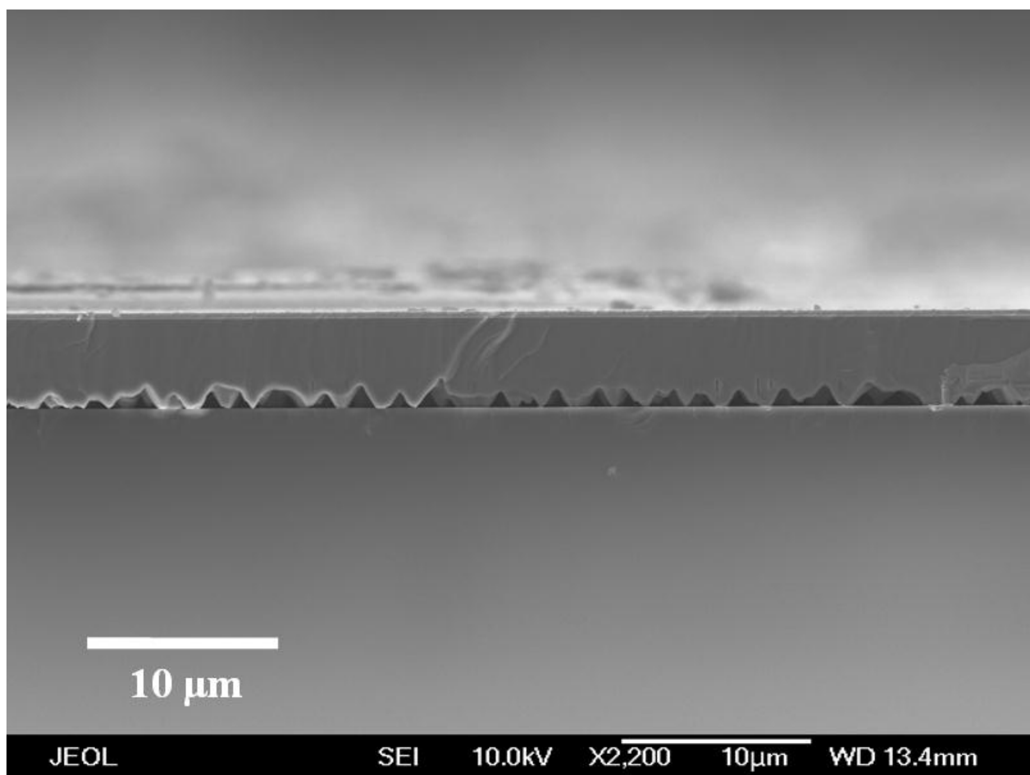

Fig. 5.4 A zoom out view of the inverted pyramid structures at GaN-sapphire interface

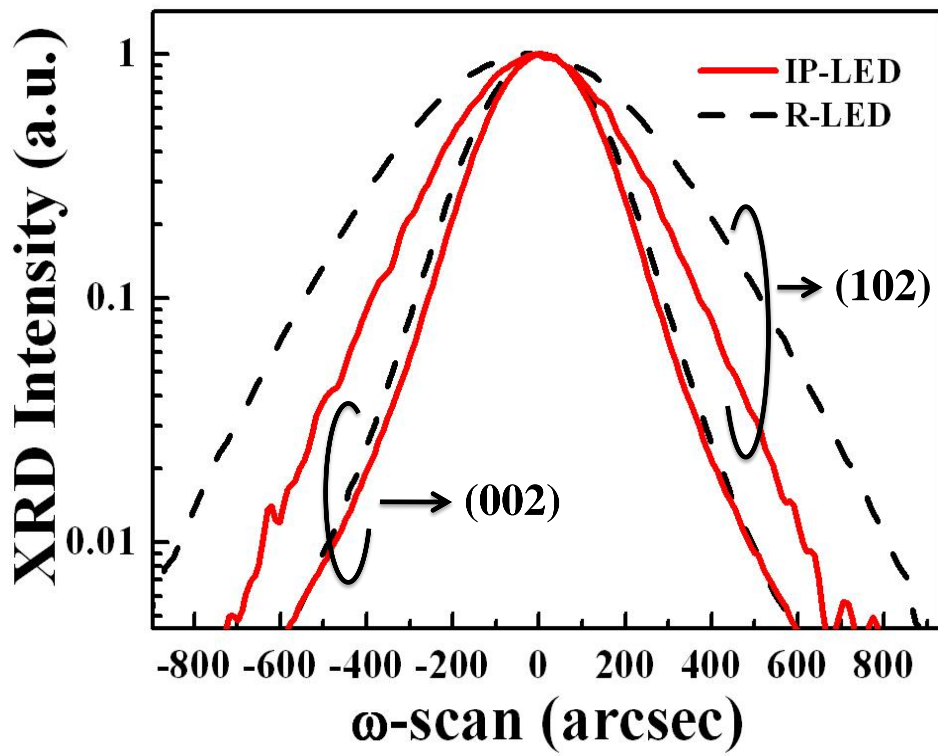

Fig. 5.5 X-ray diffraction rocking curves for IP-LED and R-LED samples

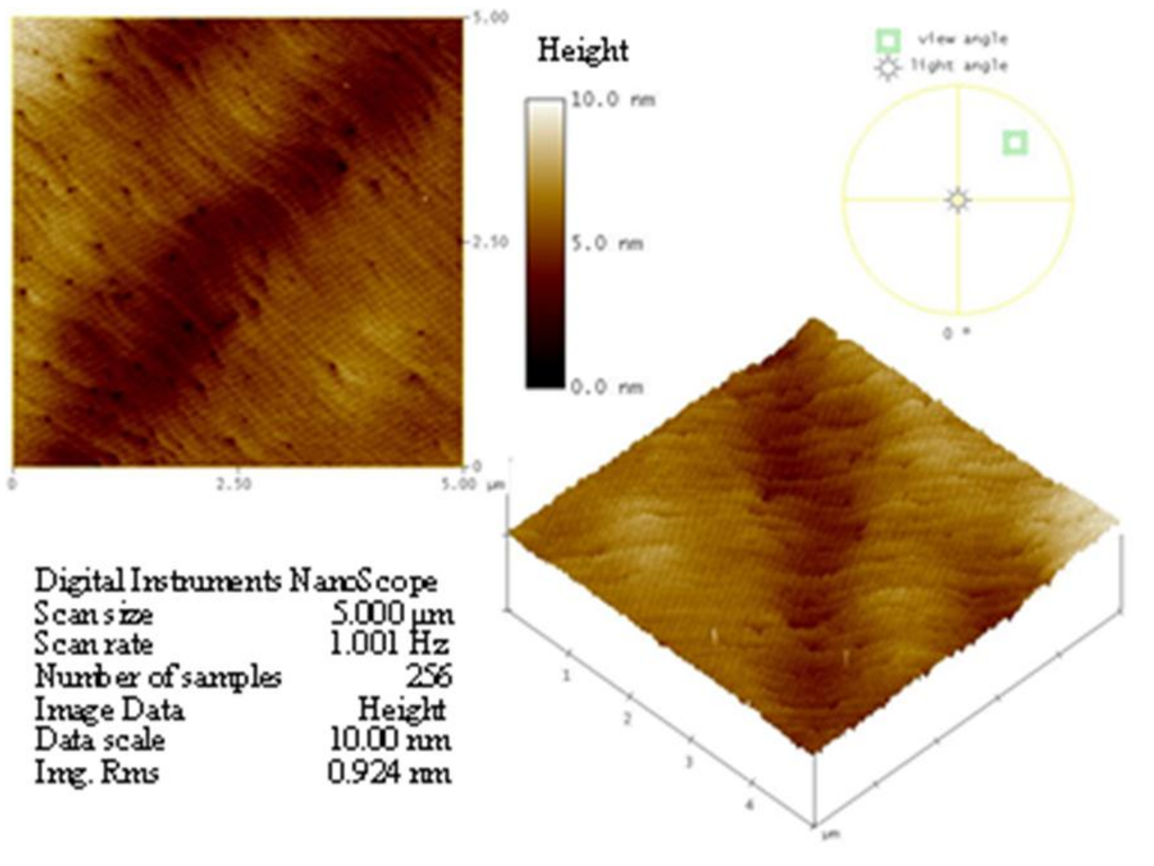

Fig. 5.6 Surface morphology of the UVLED with inverted pyramid scanned by AFM

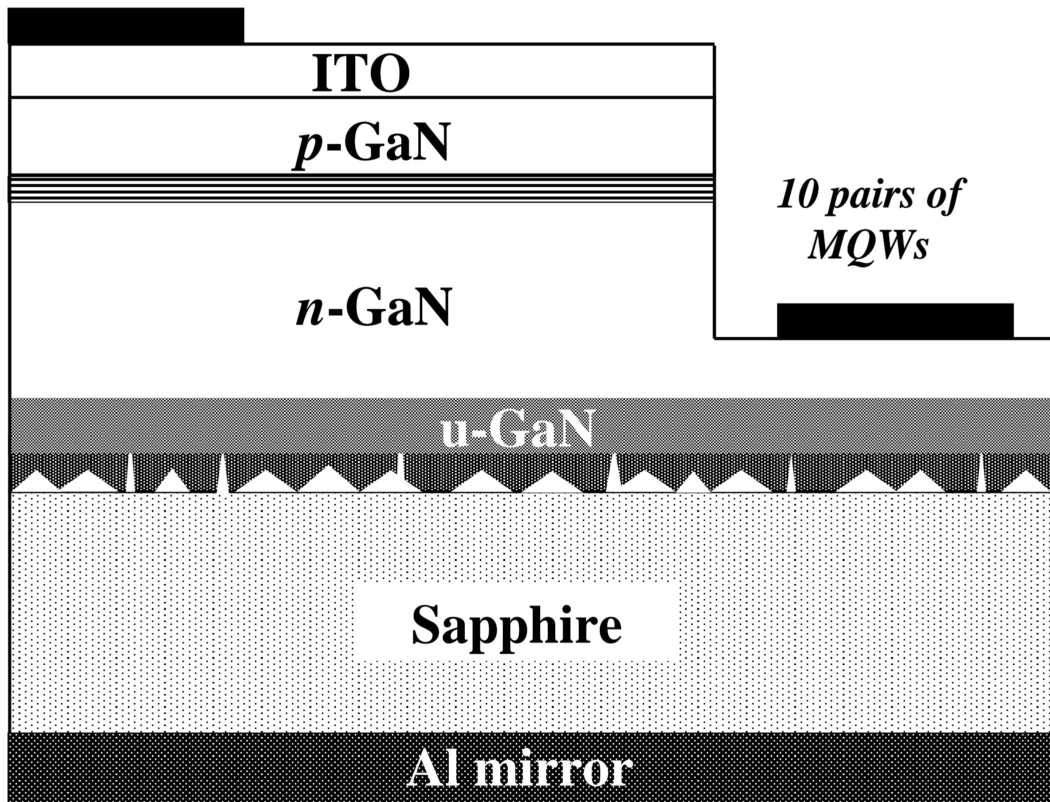

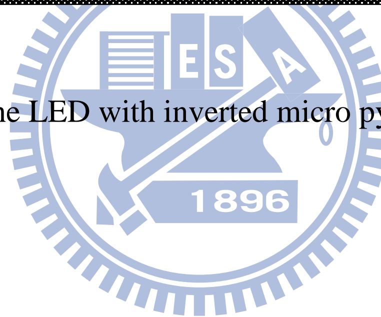

Fig. 5.7 The schematic of the LED with inverted micro pyramid structures

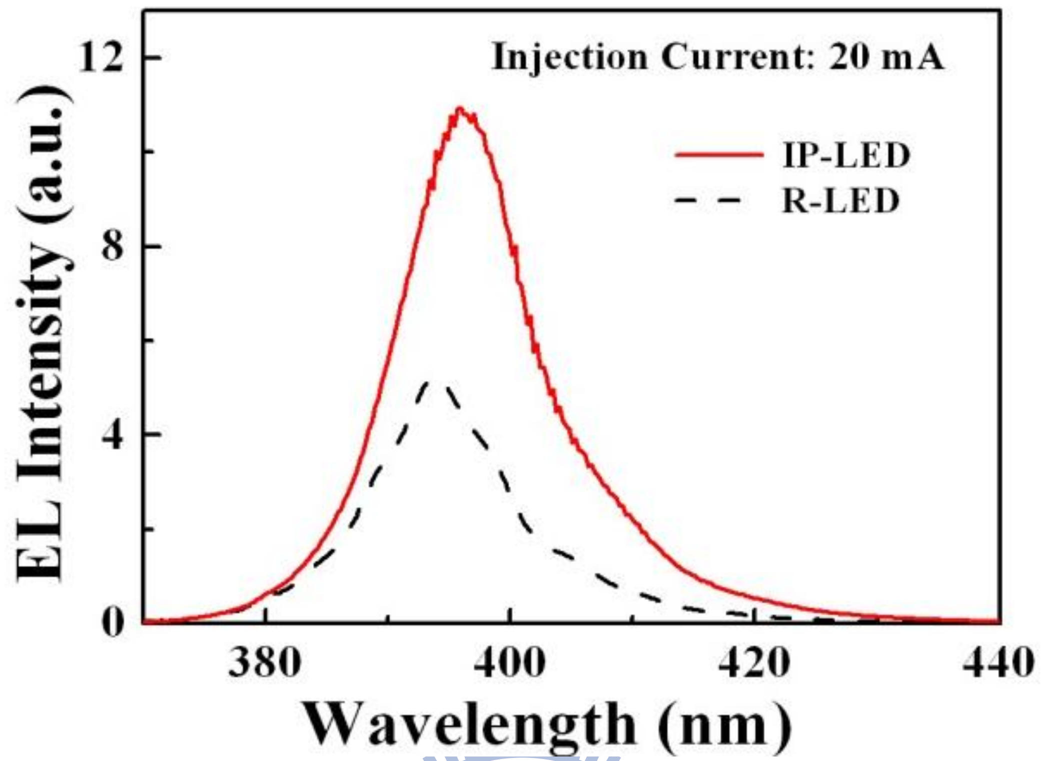

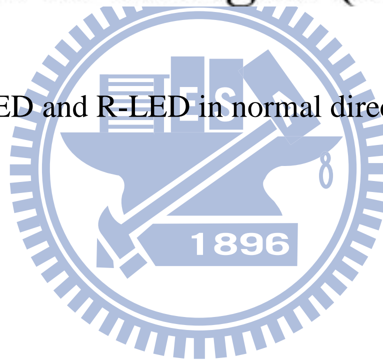

Fig. 5.8 EL spectra of IP-LED and R-LED in normal direction

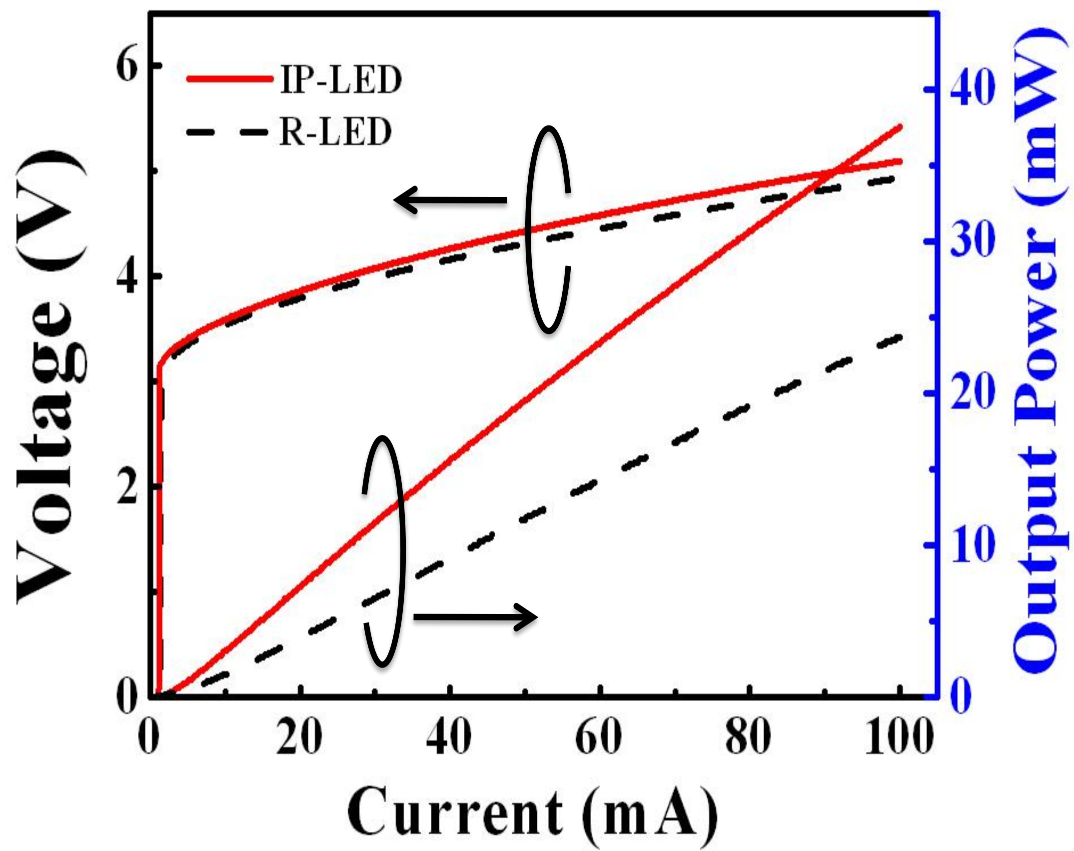

Fig. 5.9 L-I-V curves of IP-LED and R-LED

1896

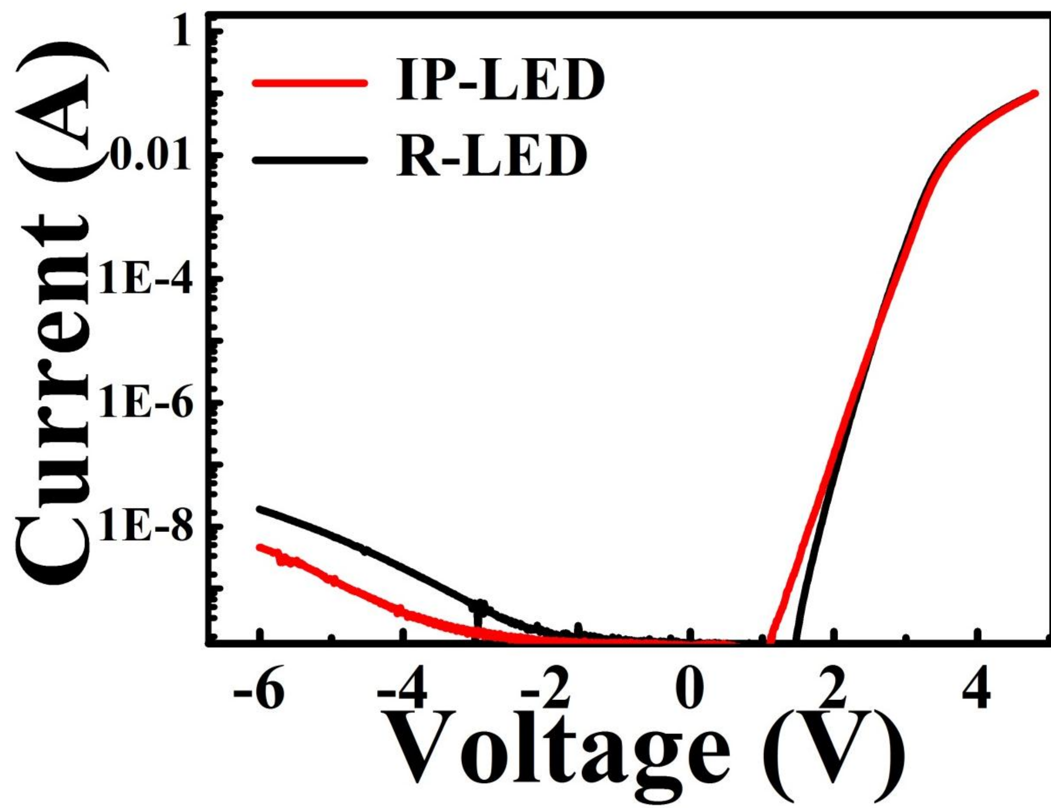

Fig. 5.10 The reverse voltage versus current characteristics of IP-LED and R-LED

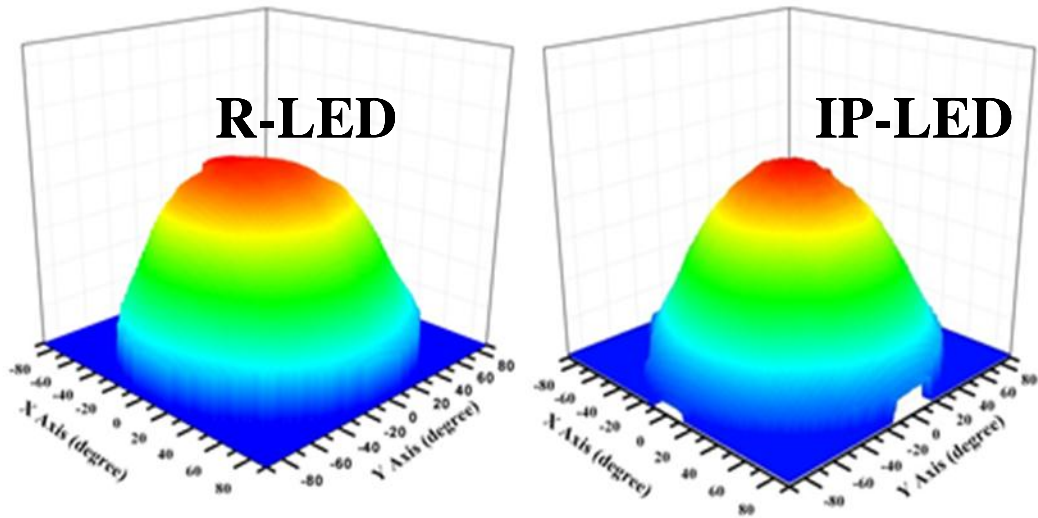

Fig. 5.11 Three-dimension far field patterns of IP-LED and R-LED

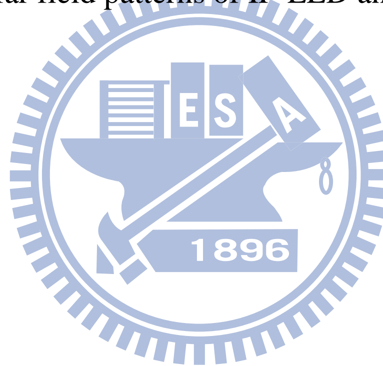

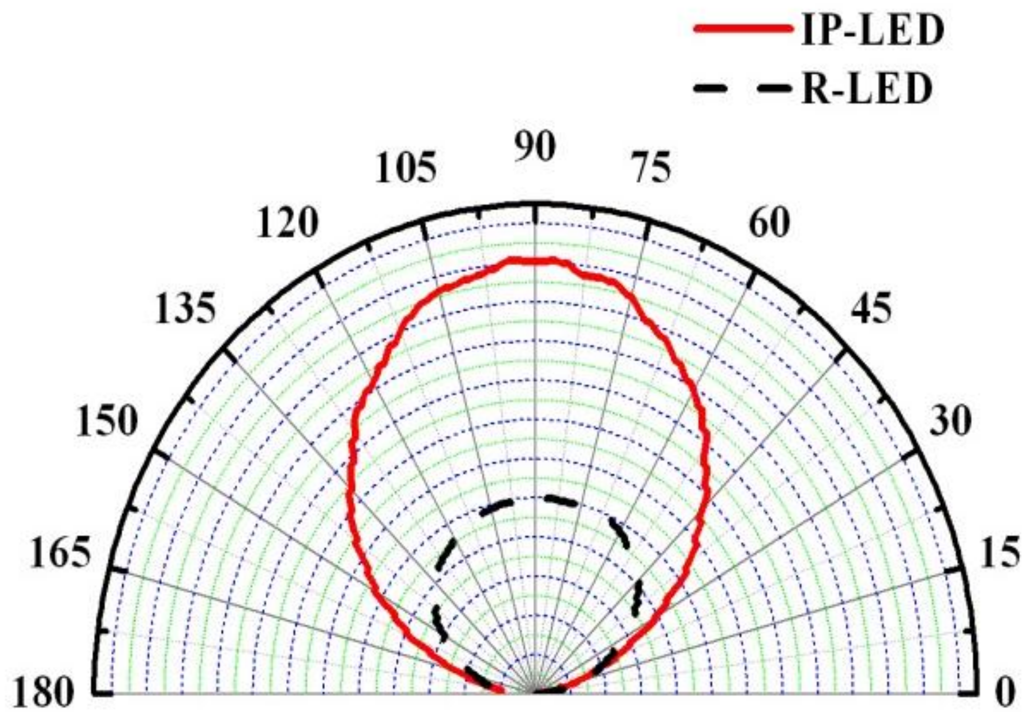

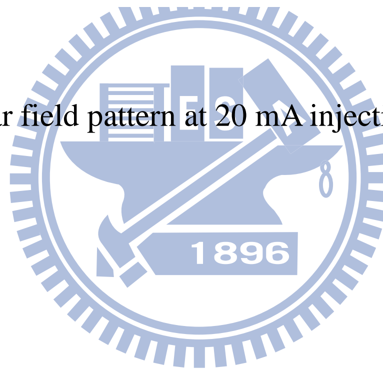

Fig. 5.12 Two-dimension far field pattern at 20 mA injection current (normal direction)

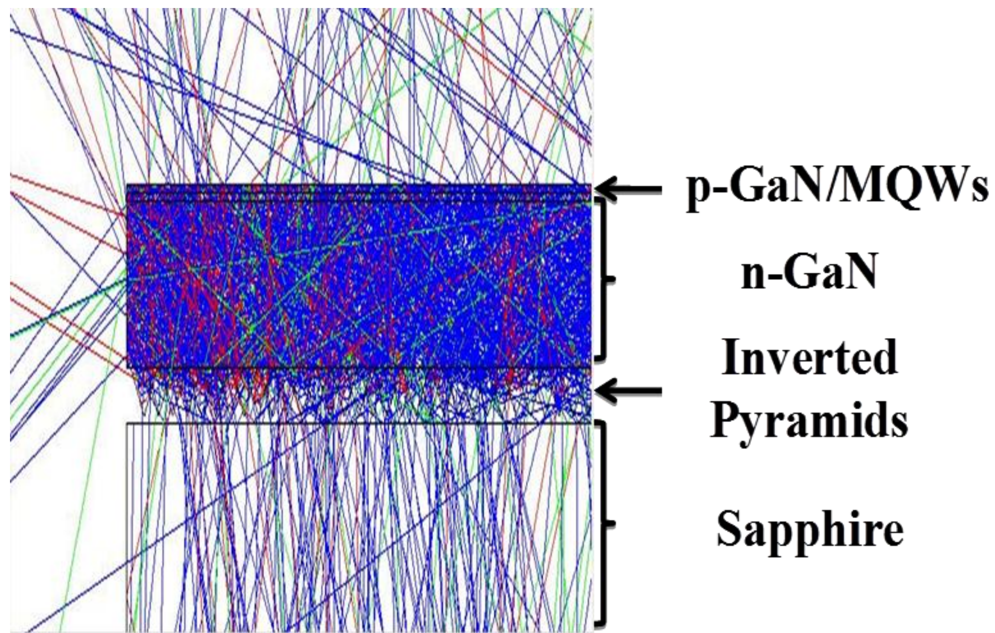

(a)

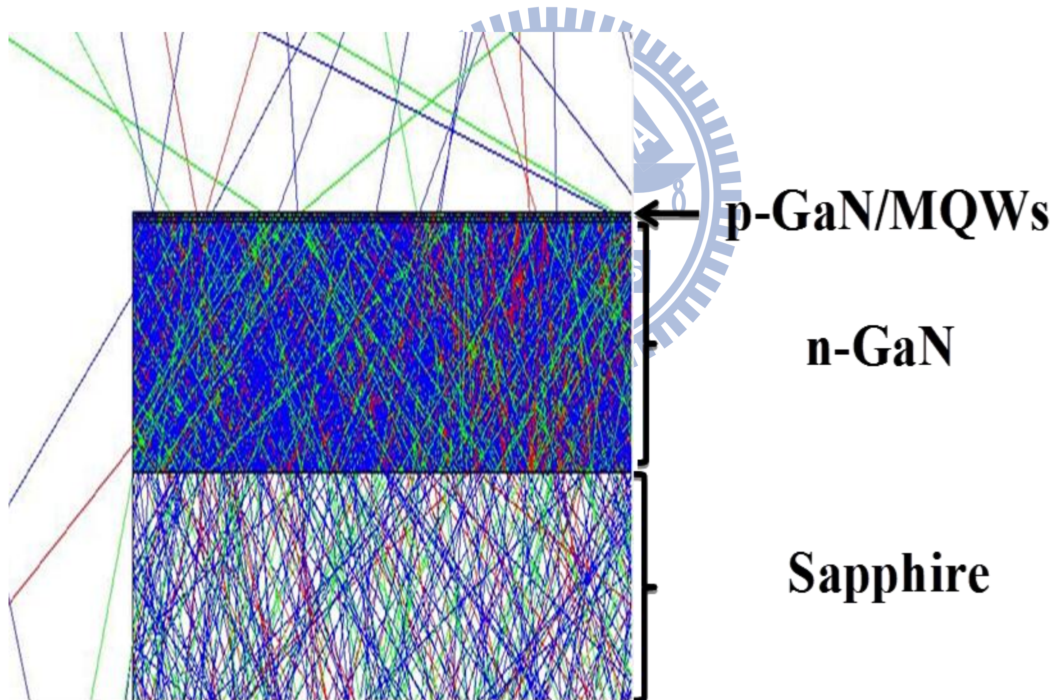

(b)

Fig. 5.13 Monte Carlo Ray tracing simulations. (a) and (b) are zoom in views at GaN-sapphire interface for IP-LED and R-LED

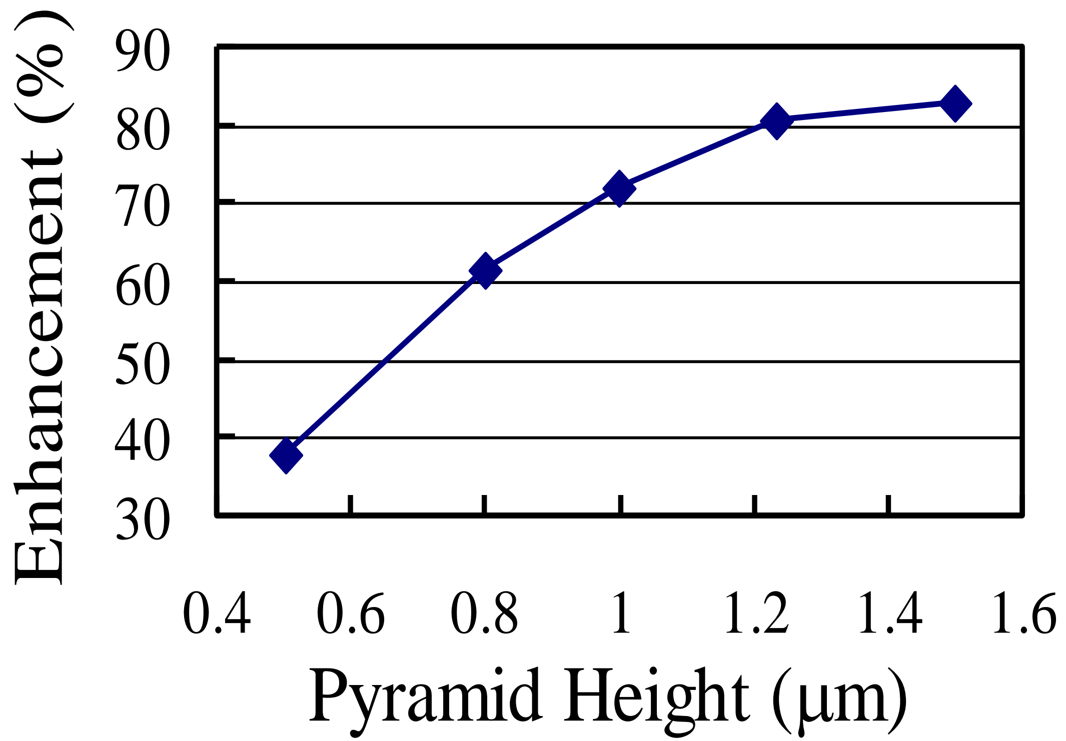

Fig. 5.14 Light extraction enhancements versus different pyramid heights

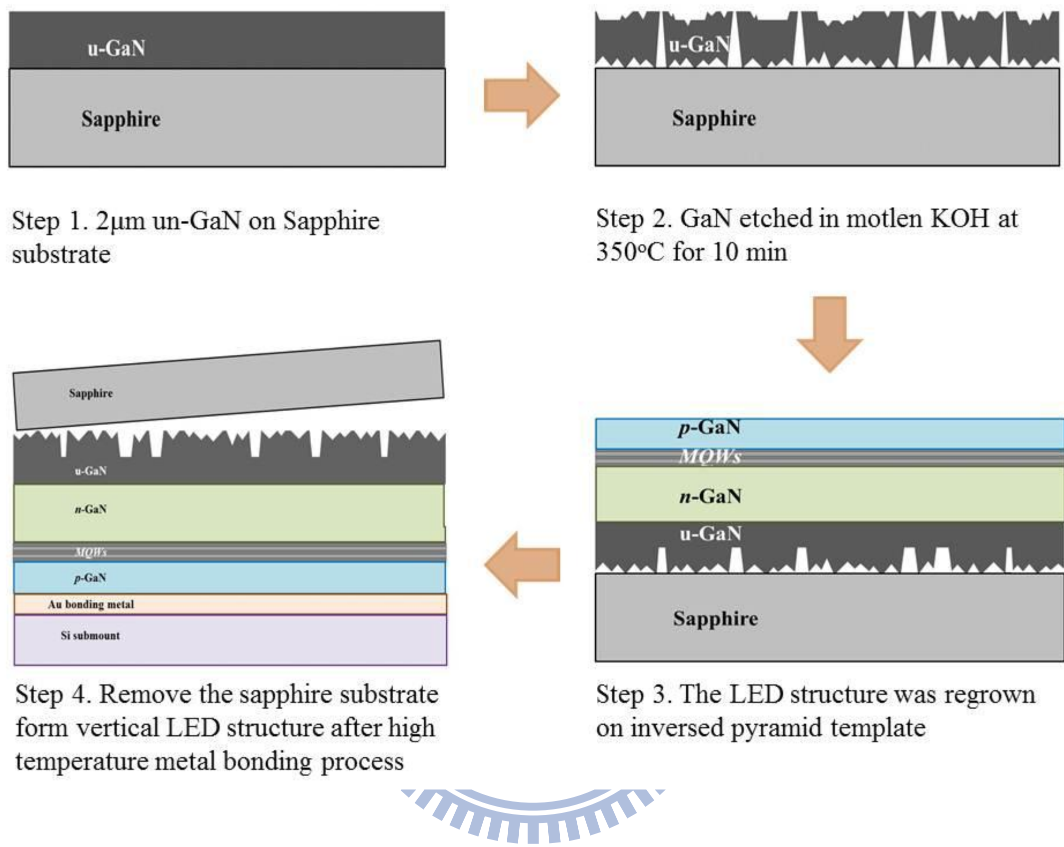

Fig. 5.15 The process flowchart for fabrication of thin GaN structure

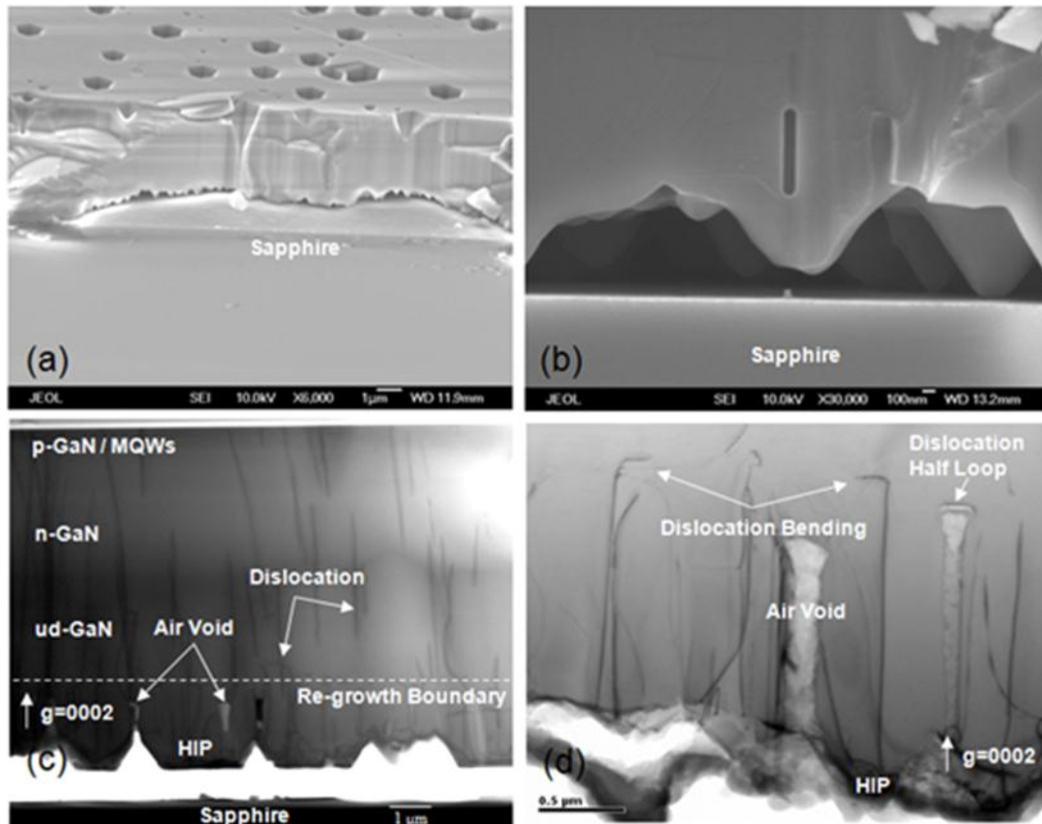

Fig. 5.16 Cross-sectional SEM images of (a) IP structure formed in the wet etching process (b) The re-growth HIP GaN/air interface; Cross-sectional TEM images of (c) GaN-based LED structure grown on IP GaN/air template (d) The re-growth IP GaN/air boundary. The diffraction condition is g=(0002).

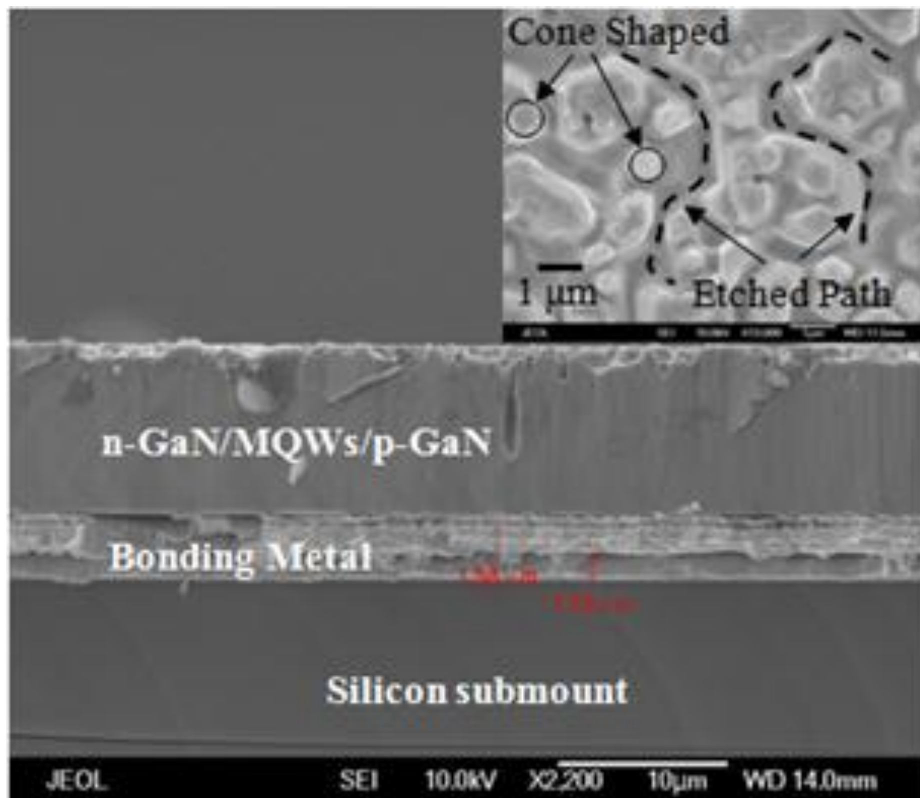

Fig. 5.17 Cross-sectional SEM image of the vertical LED structure after mechanical lift-off GaN LED/Silicon from sapphire substrate. Inset shows top-view SEM image of the IP surface morphology.

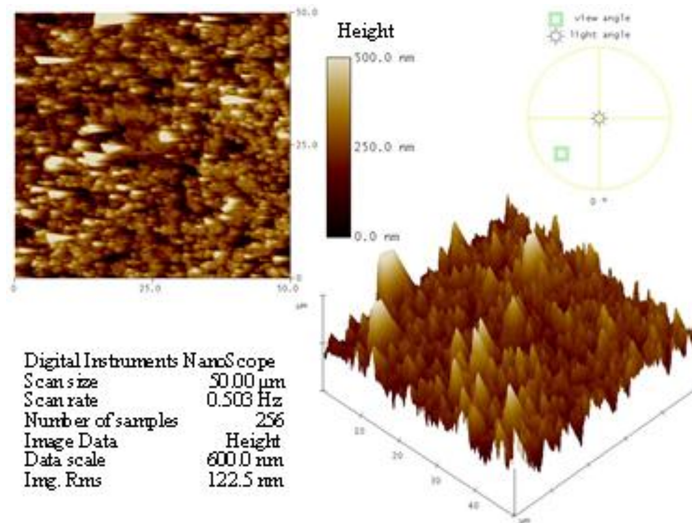

Fig. 5.18 Surface morphology of the thin GaN LED structure after mechanical lift-off scanned by AFM

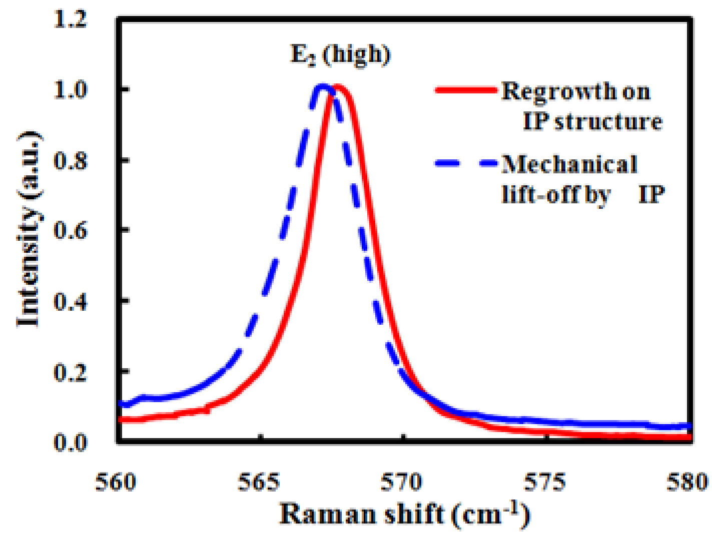

Fig. 5.19 Room temperature Raman spectrum of GaN epilayer regrowth on IP structure and mechanical lift-off by IP structure

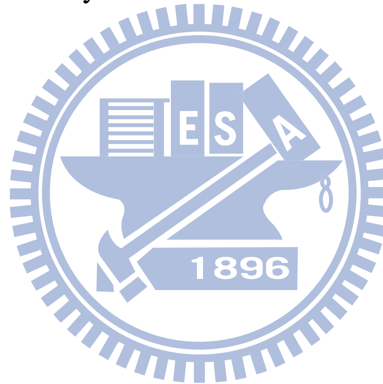

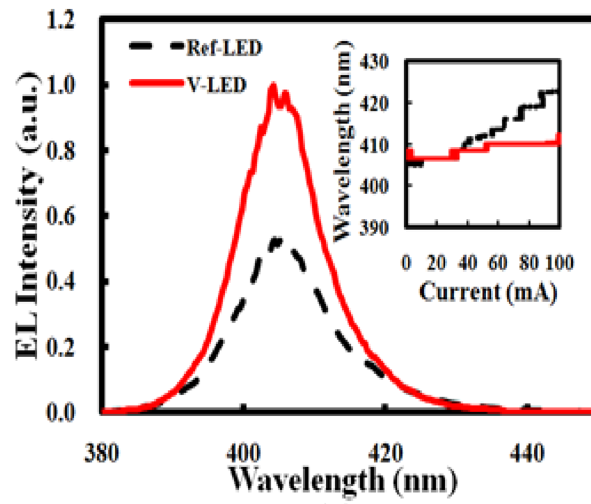

Fig. 5.20 EL spectra of Ref-LED and V-LED in normal direction at 20mA. Inset shows peak wavelength shift of Ref-LED and V-LED

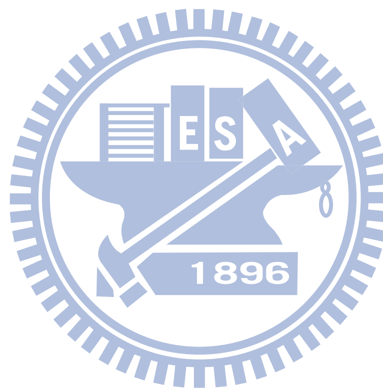

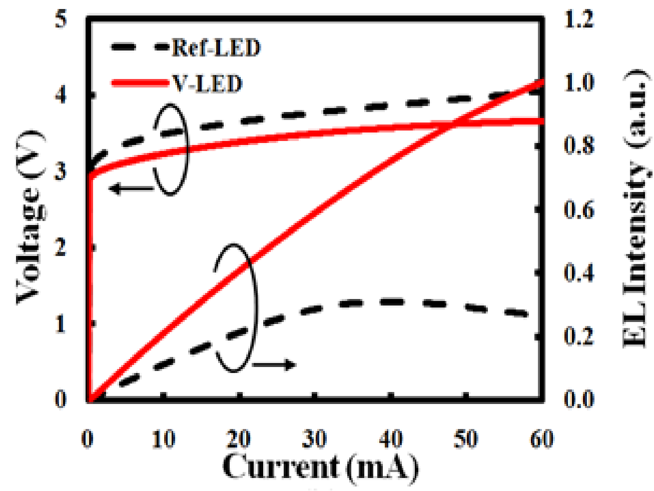

Fig. 5.21 L-I-V characteristics of the two fabricated LEDs

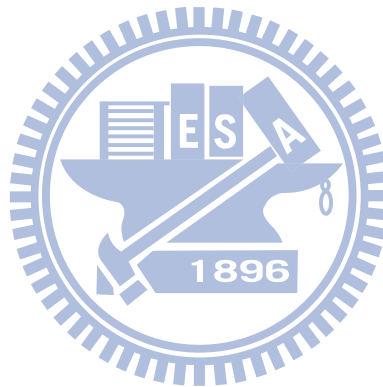

References

[1]. T. Fujii, Y. Gao, R. Sharma, E. L. Hu, S. P. DenBaars, and S. Nakamura, Appl. Phys. Lett. **84**, 855 (2004).

[2]. Chia-En Lee, Yea-Chen Lee, Hao-Chung Kuo, Tien-Chang Lu, and Shing-Chung Wang, IEEE Photonics Technol. Lett. **20**, 659 (2008).

[3]. S. J. Chang, C. F. Shen, W. S. Chen, C. T. Kuo, T. K. Ko, S. C. Shei, and J. K. Sheu, Appl. Phys. Lett. **91**, 013504 (2007).

[4]. A. David, T. Fujii, E. Matioli, Rajat Sharma, Shuji Nakamura, Steven P. DenBaars, and Claude Weisbuch, Appl. Phys. Lett. **88**, 133514 _2006.

[5]. T. A. Truong, L. M. Campos, E. Matioli, I. Meinel, C. J. Hawker, C. Weisbuch, and P. M. Petroff, Appl. Phys. Lett. **94**, 023101 (2009).

[6]. Y. J. Lee, H. C. Kuo, T. C. Lu, B. J. Su, and S. C. Wang, Journal of The Electrochemical Society, **153,** G1106 (2006).

[7]. A. Bell, R. Liu, F. A. Ponce, H. Amano, I. Akasaki, and D. Cherns, Appl. Phys. Lett. **82**, 349, 2003.

[8]. J. Lee, S. Ahn, S. Kim, D.-U. Kim, H. Jeon, S.-J. Lee, and J. H. Baek, Appl. Phys. Lett. **94**, 101105 (2009).

[9]. K. Tadatomo, H. Okagawa, Y. Ohuchi, T. Tsunekawa, Y. Imada, M. Kato, and T. Taguchi, Jpn. J. Appl. Phys., Part 2 **40**, L583 (2001).

[10]. Eun-Hyun Park, Jin Jang,1 Shalini Gupta, Ian Ferguson, Cheol-Hoi Kim, Soo-Kun Jeon, and Joong-Seo Park, Appl. Phys. Lett. **73,** 1688 (2008).

[11]. H. Heinke, V. Kirchner, S. Einfeldt, and D. Hommel, Appl. Phys. Lett., **77**, 2145, (2000).

[12]. P. P. Paskov, R. Schifano, T. Malinauskas, T. Paskova, J. P. Bergman,

ES A 1896

B. Monemar, S. Figge, D. Hommel, B. A. Haskell, P. T. Fini, J. S. Speck, and S. Nakamura, phys. stat. sol. (c) **3**, 1499-1502 (2006)

[13] S. Nakamura and G. Fasol, *The Blue Laser Diode: GaN based Light Emitters and Lasers*, Spring-Verlag, Berlin and Heidelberg (1997).

[14] E. F. Schubert, *Light Emitting Diodes*, 1st ed. (Cambridge University Press, Cambridge, 2003).

[15] J. Han, M. H. Crawford, R. J. Shul, J. J. Figiel, L. Zhang, Y. K. Song, H. Zhou and A. V. Nurmikko, Appl. Phys. Lett. **73**, 1688 (1998).

[16] W. S. Wong, T. Sands, N. W. Cheung, M. Kneissl, D. P. Bour, P. Mei, L.T. Romano, and N. M. Johnson, Appl. Phys. Lett. **75**, 1360 (1999).

[17] W. Y. Lin, D. S. Wuu, K. F. Pan, S. H. Huang, C.E. Lee, W.K. Wang, S. C. Hsu, Y. Y. Su, S. Y. Huang, R. H. Horng, IEEE Photonics Technol. Lett. **17**, 1809 (2005).

[18] H. Goto, S. W. Lee, H. J. Lee, H.-J. Lee, J. S. Ha, M. W. Cho, and T.Yao, Phys. Status Solidi C **5**, 1659 (2008).

[19] D. J. Rogers, F. Hosseini Teherani, A. Ougazzaden, S. Gautier, L. Divay, A. Lusson, O. Durand, F. Wyczisk, G. Garry, T. Monteiro, M. R. Correira, M. Peres, A. Neves, D. McGrouther, J. N. Chapman, and M. Razeghi, Appl. Phys. Lett. **91**, 071120 (2007).

[20] J. Park, K. M. Song, S. R. Jeon, J. H. Baek, and S. W. Ryu, Appl. Phys. Lett. **94**, 221907 (2009).

[21] M. H. Lo, P. M. Tu, C. H. Wang, C. W. Hung, S. C. Hsu, Y. J. Cheng, H. C. Kuo, H. W. Zan, S. C. Wang, C. Y. Chang, and S. C. Huang, Appl. Phys. Lett. **95**, 041109 (2009).

[22] P. Puech, F. Demangeot, J. Frandon, C. Pinquier, M. Kuball, V.

Domnich, Y. Gogotsi., J. Appl. Phys. **96**, 2853 (2004).

[23] S. Hearne, E. Chason, J. Han, J.A. Floro, J. Figiel, J. Hunter, H. Amano, and I.S.T. Tsong, Appl. Phys. Lett. **74**, 356 (1999).

[24] K. Kusakabe, A. Kikuchi and K. Kishino, Jpn. J. Appl. Phys., Part 2 **40**, L192 (2001).

[25] J. R. Chang, T. H. Yang, J. T. Ku, S. G. Shen, Y. C. Chen, Y. Y. Wong and C.Y. Chang, J. Cryst. Growth **311**, 1997 (2009).

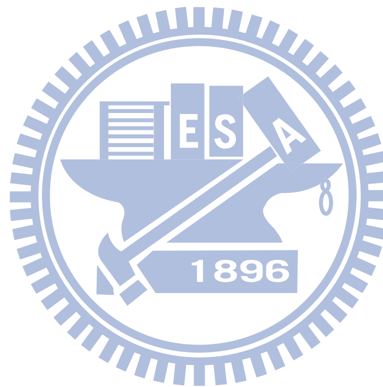

Chapter 6 Growth and Fabrication of GaN nanopillars

6.1 The progress of low dimension GaN structure

GaN 1-D nanostructure (i.e. nanorods、nanowires and nanopillars) have potential to increase light extraction efficiency of light emitting devices and reduce the quantum confine stark effect in strain relaxed GaN multiple quantum wells devices. In addition, the 1-D GaN nanowires structure have been shown that it can function as optical waveguides and Fabry-Perot cavities for strong light confinement and coherent feedback [1, 2]. Its cavities typically have a small size with diameters ranging from 10 to 100 nm and lengths ranging from 0.5 to 40 μm and a large refractive index contrast between GaN (n=2.5) and air (n=1). The room temperature optically pumped GaN nanowire lasers have been demonstrated [2, 3]. For the synthesis of GaN 1-D nanostructure, bottom-up and top-down approaches have been developed on GaN nanowire or nanorod structure by MOCVD、HVPE and RF-MBE systems. The GaN nano structure devices can be fabricated by top-down approach, which employs nano mask and etching, or bottom-up approach, which relies on nano scale crystalline growth. The top-down approach [4] has better control on patterning but the etching process often induces surface defects. The bottom-up approach [5], on the contrary, has less control on over all patterning but often produces crystalline GaN facets on the sidewalls with much less defects. In this chapter, we report the fabrication of hexagonal crystalline nanopillars and observation observation of room temperature lasing action form an optically pumped GaN nanopillars The nanopillars were fabricated using self-assembled Ni as nanomask and ICP-RIE etching followed by crystalline regrowth of nanopillar formed

wafer

6.2 Fabrication of hexagonal GaN Nanopillars

The schematic of fabrication process flow is shown in Fig. 6.1(a)-(d). The sample with a 3μm GaN buffer layer is grown on a c-plane sapphire (0001) substrate by low pressure metal organic chemical vapor deposition (MOCVD). First, a 300 nm Si_3N_4 thin film is deposited on the GaN buffer layer by plasma-enhanced chemical-vapor deposition system, followed by electron-beam evaporation of a 100 nm Ni metal film as illustrated in Fig. 6.1(a). The as grown sample is subsequently subjected to rapid temperature annealing at 850 ˚C under a nitrogen ambiance for 1 min. to form self-assembled Ni nano masks on Si_3N_4 film surface as shown in Fig. 6.1 (b). A reactive ion etching is conducted to etch Si_3N_4 film using a CF_4/O_2 gas-mixture to transfer Ni nano mask pattern down to Si_3N_4 layer. The sample is subsequently etched down to the GaN buffer layer by the ICP-RIE system (SAMCO ICP-RIE 101iPH) operated at 13.56 MHz under a gas mixture of Cl_2/Ar = 50/20 sccm with 2 mins. of etching time to form nanopillars as shown in Fig. 6.1(c). The ICP source power, bias power and the chamber pressure of the ICP-RIE system are set at 400/100 W. The sample is dipped into a nitric acid solution (HNO_3) at 100 ◦C for 5 min. to remove the Ni nano masks. Finally, the GaN nanopillar provides seed layer for epitaxial regrowth, which grows a GaN passivation layer on the sidewalls of etched GaN nanopillars as shown in Fig. 6.1 (d). Fig. 6. 2(a)-(e) shows the scanning electron microscope images of as grown GaN nanopillars sample after regrowth process. Self-assembled Ni nano masks on Si_3N_4 film surface as shown in Fig. 6. 2(a) and its diameter is about 100nm. Fig. 6. 2 (b) shows nanopillars etched down by ICP-RIE then were removed the Ni nano maskd. The Fig. 6.2 (c) is the top view of nanopillars showing hexagonal crystalline

sidewall facets and the hexagonal nanopillar density about ~$8.5 \times 10^5/cm^2$. Various nanopillar with different diameter from 200nm to 300nm were prepared by using self-assembled different size Ni nano masks. At the top of each nanopillar, there is GaN slightly growing over Si_3N_4 mask showing inclined {1102} facets as shown in Fig. 6.2(d). The diameter and height of nano-pillars are about 250 nm and 660 nm, respectively, as shown in Fig. 6.2 (e).

6.3 Characteristics of Optically Pumped Nitride-Based nanopillars

The fabricated GaN nanopillars were pumped with 355 nm tripled Nd:YAG laser at room temperature. The focus spot had a Gaussian beam waist of 1.8 μm, verified by knife edge measurement Fig. 6.3 shows nanopillars emission spectra at several pump intensities. At low pump intensity, the emission spectrum has a broad spontaneous emission with small peak at 363 nm. As pump intensity increases, the emission at 363 nm become the dominant peak with intensity increases drastically with pumping power as shown in Fig. 6.3. The clear lasing threshold behavior is observed at a threshold pumping power density of 122 MW/cm^2. The variation of emission linewidth versus pump intensity is also shown in Fig. 6.4. The emission linewidth decreases with pumping power and reaches a lowest value of about 0.38 nm beyond the threshold.

6.4 Random lasing in GaN nanopillars

A threshold behavior was observed in our as-grown samples: the sharp peak at 363 nm emerged in the emission spectrum when increasing pumping density, the integrated emission intensity increased much more rapidly with the pump power. These data suggest that laser action has occurred in GaN nanopillars. Because of the short scattering mean free path in GaN nanopillars, the emitted light is strongly scattered, and closed

loop paths can be formed through multiple scattering. There are many such closed loop paths in GaN nanopillars. These loops could serve as ring cavities for light. Along different loop paths, the probability of a photon or exciton scattered back to its starting point is different. In other words, the ring cavities formed by recurrent scattering have different loss. When the pump intensity increases, the gain reaches the loss first in the low-loss cavities. Then laser oscillation occurs in these cavities, and the lasing frequencies are determined by the cavity resonances. Laser emission from these resonators results in a small number of discrete narrow peaks in the emission spectrum. As the pump power increases further, the gain increases and it exceeds the loss in the lossier cavities. Laser oscillation in those cavities adds more discrete peaks to the emission spectrum.

As shown in the Fig. 6.5, when the scattering mean free path becomes equal to or less than the wavelength, light may return to a scatterer from which it was scattered before, and thereby forming closed loop paths. If the amplification along such a loop path exceeds the loss, laser oscillation could occur in the loop which serves as a laser resonator. The requirement of the phase shift along the loop being equal to a multiple of 2π determines the oscillation frequencies. Such a laser is called a “random laser.”[7] It represents a coherent effect in an active random medium

In summary, we report the fabrication of GaN nanopillars by self-assembled Ni nanomasked etching, followed by epitaxial regrowth to form crystalline facets on the etched nanopillars. The density of GaN nanopillars is about $8.5\times10^{8}/cm^{2}$ and the diameter and height of GaN

nanopillars are about 250 nm and 660 nm respectively. At low pumping intensity, the emission has a broad spontaneous emission spectrum with a peak around 363 nm. As pump intensity increases, a narrow peak at 363 nm emerges quickly from the broad spontaneous emission back ground. The lasing action occurs at threshold pump power density of about 122 MW/cm^2. The laser emission linewidth decreases with pumping power and reaches a lowest value of about 0.38 nm beyond the threshold. The lasing phenomenon could to due to random laser action with coherent feedback in GaN nanopillars under optical pumping at room temperature. This observation provides direct evidence for the existence of scattering of light.

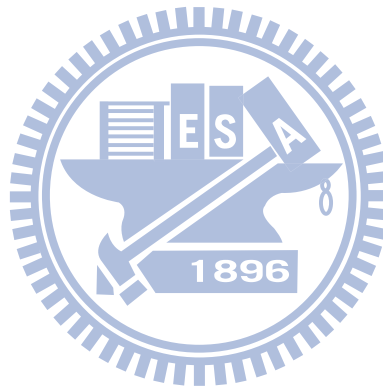

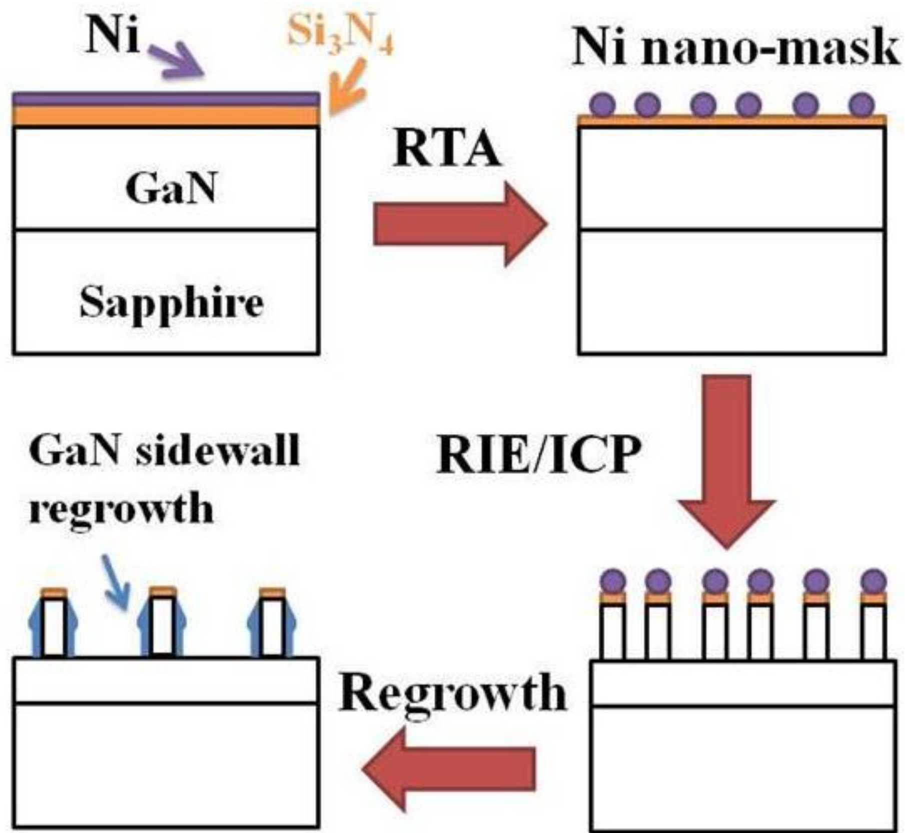

Fig. 6.1 (a)-(d) GaN nanopillars fabrication steps

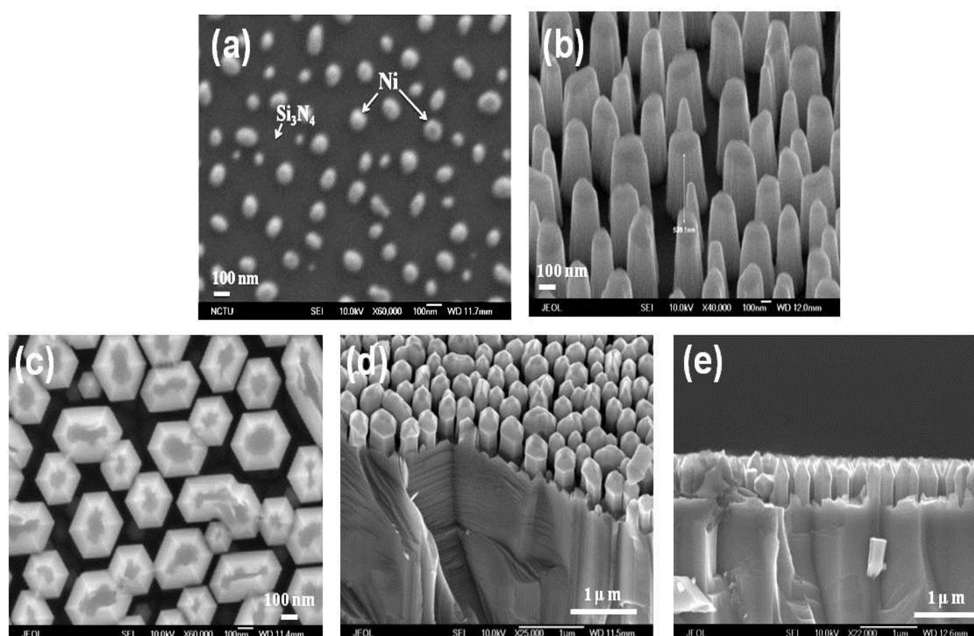

Fig.6.2 (a) Top view SEM image of Ni nano mask, (b) Tilted SEM image of GaN nanopillars before regrowth, (c) Top view SEM image of GaN nanopillars after regrowth, (d) Tilted SEM image of GaN nanopillars after regrowth and (e) cross section SEM image of GaN nanopillars after regrowth

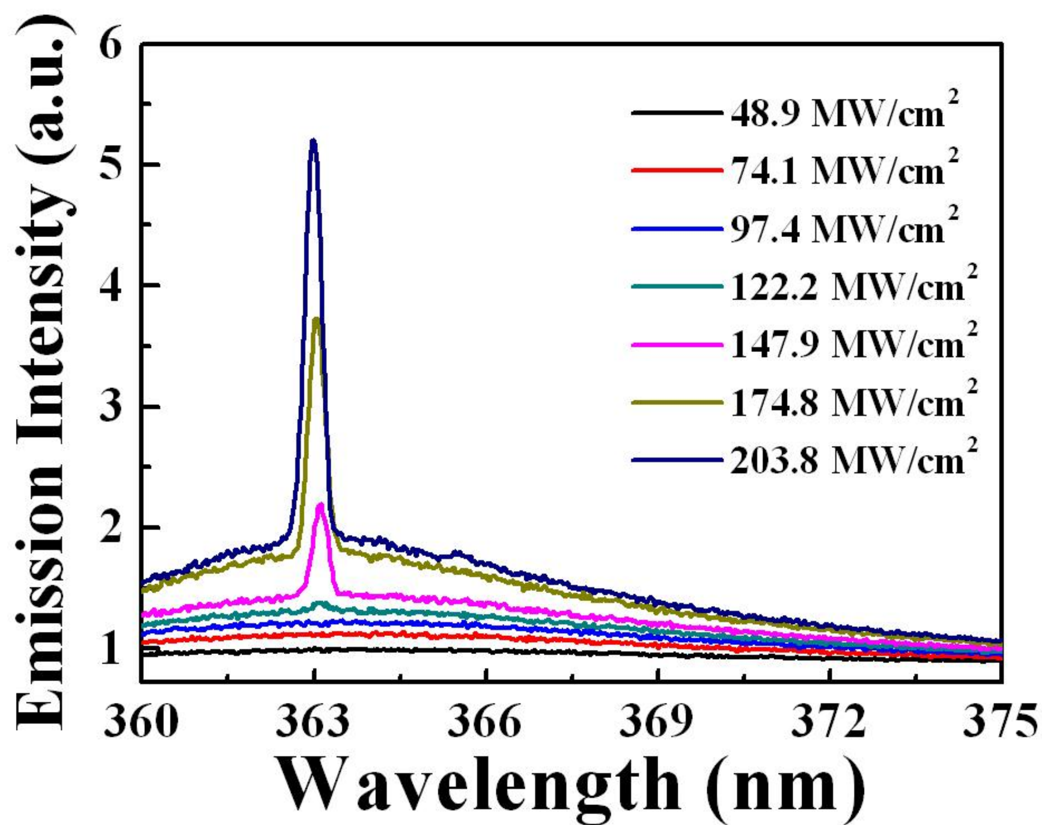

Fig. 6.3 Emission spectra of optically pumped GaN nanopillars

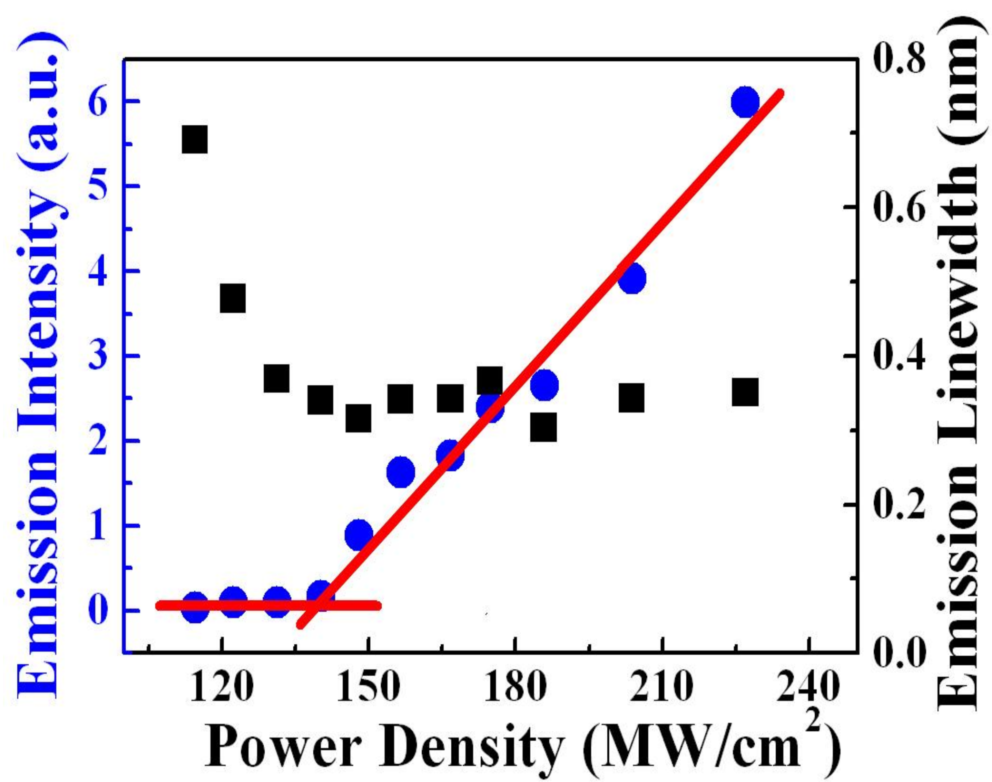

Fig. 6.4 Peak intensity and linewidth vs. pump intensity

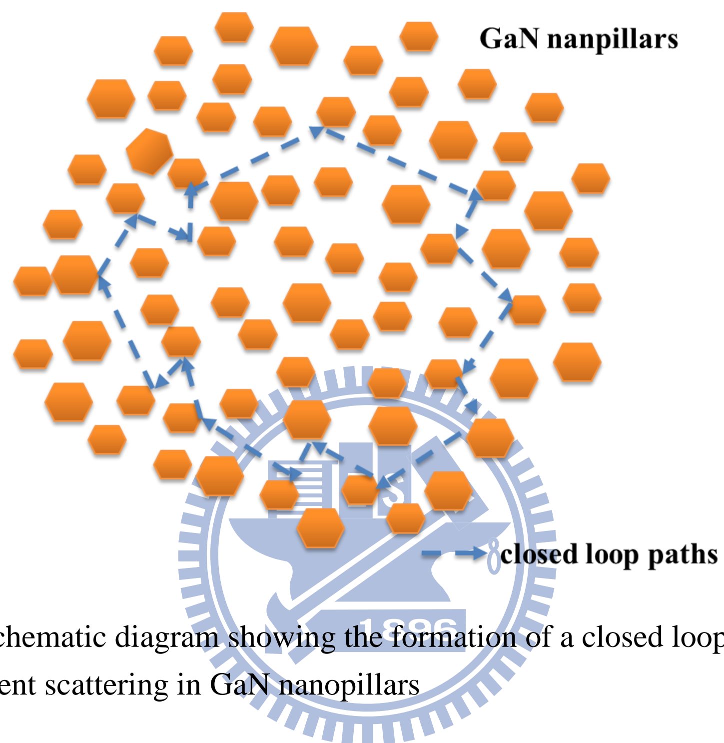

Fig. 6.5 The schematic diagram showing the formation of a closed loop path for light through recurrent scattering in GaN nanopillars

References

[1] C.-H. Lee, J. Yoo, Y. J. Hong, J. Cho, Y.-J. Kim, S.-R. Jeon, J. H. Baek, and G.-C. Yi Appl. Phys. Lett. **94**, 213101. (2009)

[2] Huang H W, Chu J T, Hsueh T H, Ou-Yang M C, Kuo H C and Wang S C J. Vac. Sci. Technol. B **24** 1909(2006)

[3] Justin C. Johnson, Heon-Jin Choi, Kelly P. Knutsen, Richard D., Schaller, Peidong Yang, and Richard J. Saykally, Nature, Materials **1**, 106 (2002)

[4] H. W. Huang, J. T. Chu, T. H. Hsueh, M. C. Ou-Yang, H. C. Kuo, and S. C. Wang J. Vac. Sci. Technol. B **24** 1909(2006)

[5] Ching-Lien Hsiao,a_ Li-Wei Tu,b_ Tung-Wei Chi,c_ and Min Chen Appl. Phys. Lett., **90**, 043102 (2007)

[6] S. Kako, T. Someya, and Y. Arakawa, Appl. Phys. Lett., **80**, 722 (2002)

[7] H. Cao, Y. G. Zhao, H. C. Ong, S. T. Ho, J. Y. Dai, J. Y. Wu, and R. P. H. Chang Appl. Phys. Lett., **73**, 3656 (2002)

Chapter 7 Summary and Future Works

7.1 Summary

In summary, in this dissertation we have studied low dislocation and high crystalline quality AlGaN/GaN MQWs grown on sapphire substrate by using the ALD grown AlGaN barrier consisted of AlN/GaN SLs. he AFM data show smooth surface morphology with a small surface roughness RMS value of about 0.35 nm and no surface cracks. The TEM and HRXRD measurements show that the grown sample has sharp interfaces between SLs layers and QWs with good periodicity. The light output power for the GaN-based LED with an ALD insert layer at 20 mA was 27% higher than that for a conventional GaN-based LED structure

In the case of defect selective passivation LED have been grown and fabricated. The defect passivation SiO_2 masks are self-aligned to the TD defect pits created by KOH defect selective etching without photolithography patterning and can significantly reduce TD density from $1x10^9$ to $4x10^7$ cm^{-2}. The SiO_2 masks also improve the light extraction efficiency in LED application. TEM image shows that some defects are resistive to KOH etching and propagate all the way to the top surface. The output power of DP-LED is enhanced by 45% at 20 mA compared to a reference one without using defect passivation.

In the case of InGaN/GaN UV LEDs with inverted pyramid structure have been grown and fabricated. The density of threading dislocations can be efficiently reduced from 2×10^9 to 1×10^8 cm^{-2} by applying the re-growth GaN epilayer on IP structure. The UV LED was fabricated by growth interrupt, chemical etching, and regrowth processes. The device electrical performance is well maintained after these steps. The overall optical output power has shown significant 85% enhancement at nominal

operating current 20 mA, which is attributed to both improved crystal quality and better light extraction efficiency. In addition, the fabrication of vertical type LED with IP structure and mechanical lift-off approach were successfully demonstrated. The in-plane compressive strain ε_{xx} are calculated to be about 1.30×10^{-3} and 6.03×10^{-4} for the GaN epilayer re-growth on IP structure and mechanical lift-off by IP structure, respectively. The overall optical output power has shown significant 100% enhancement under operating current 20 mA with this mechanical lift-off technique for fabrication the vertical-LED

Finally, we report the observation of lasing action in optically pumped GaN nanopillars at room temperature. The density of GaN nanopillars is about $8.5\times10^{8}/cm^{2}$ and the diameter and height of GaN nanopillars are about 250 nm and 660 nm respectively. The GaN nanopillars emit lasing wavelength at 363 nm with a narrow linewidth of about 0.38 nm under optical pumping at room temperature.

7.2 Future Works

7.2.1 Fabrication and characterization of ultra-low dislocation density LED with Two-step Maskless defects passivation layers

In our early reports, the low dislocation density LEDs with maskless defects passivation layer have been demonstrated. But, the high temperature molten KOH can only etch the screw type of dislocations, that's why there still remain dislocations of other types. Based on the realization of high efficient light emitting devices, we will further fabricate ultra-low dislocation density LED by two-step maskeless defects passivation layers. The entire process flowchart and thin GaN structure are shown in Fig. 7.1. The epitaxial layers of two-step LED

structure were grown by metal-organic chemical vapor deposition (MOCVD). First, we grew 2 μm GaN on sapphire as a template, and the GaN epilayer was etched in molten KOH for 10 min at high temperature (approximate 250 ~ 300 degree).After several minutes of etching by KOH, defects on the surface of GaN epilayer were etched into pits, and the etching depth was approximately 1μm. Afterward the 1μm SiO_2 film was deposited on the etched surface by plasma enhanced chemical vapor deposition (PECVD). The SiO_2 film was used as defects-passivation layer. And then we remove the sacrificial SiO_2 film on top of the GaN by chemical mechanical polishing (CMP) to expose the GaN top layer which acts as the regrowth seed layer for next step crystal overgrowth. In order to further investigate the dislocation type etched by various solutions, we repeat above process using H_3PO_4 to etch the difference type dislocation. Finally, LED structures were grown on two-step DP layer.

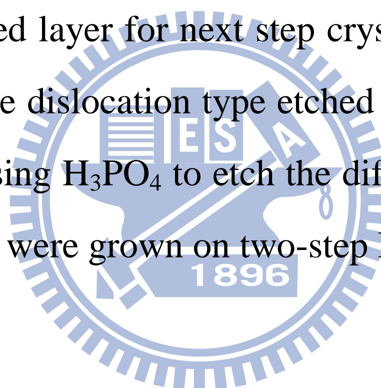

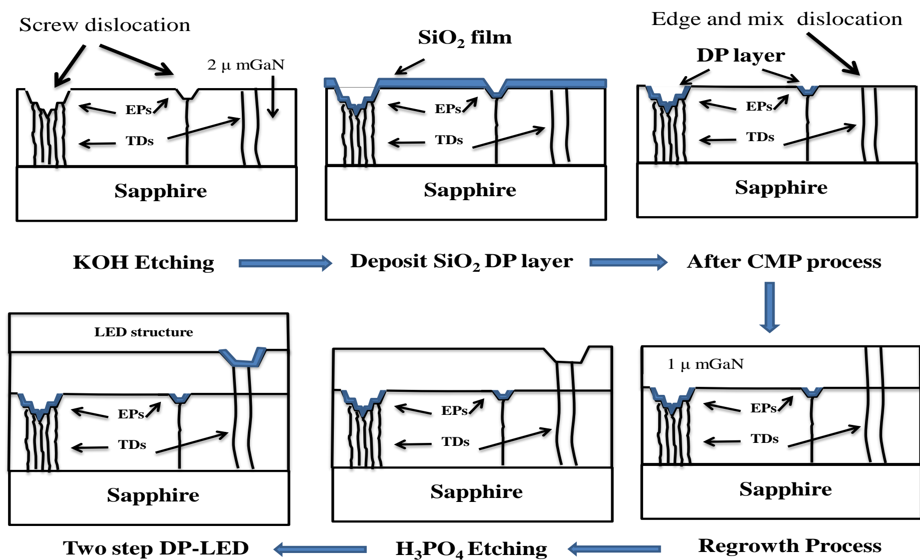

Fig. 7.1 The process flowchart for fabrication of two-step DP-LED

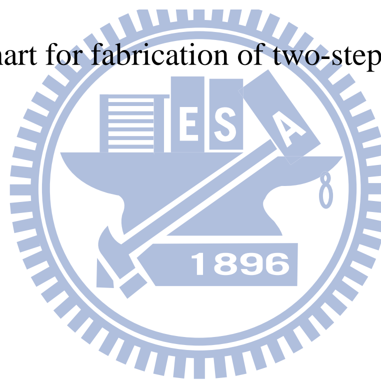

Publication lists

Journal paper

[1] **Ming-Hua Lo**, Po-Min Tu, Chao-Hsun Wang, Cheng-Wei Hung, Shih-Chieh Hsu, Yuh-Jen Cheng, Hao-Chung Kuo, Hsiao-Wen Zan, Shing-Chung Wang, Chun-Yen Chang, and Shih-Cheng Huang "Defect selective passivation in GaN epitaxial growth and its application to light emitting diodes" Appl. Phys. Lett., **95**, 211103, (2009)

[2] **Ming-Hua Lo,** Chao-Hsun Wang, Po-Min Tu, Cheng-Wei Hung, Shih-Chieh Hsu, Yuh-Jen Cheng, Hao-Chung Kuo[1], Hsiao-Wen Zan , Shing-Chung Wang , Chun-Yen Chang and Che-Ming Liu "High efficiency light emitting diode with anisotropically etched GaN-sapphire interface" Appl. Phys. Lett., **95**, 041109, (2009)

[3] S. W. Chen, **M. H. Lo**, T. T. Kao, C. C. Kao, J. T. Chu, L. F. Lin, H. W. Huang, T. C. Lu, H. C. Kuo, S. C. Wang, C. C. Kuo, and C. C. Lee, "Effects of Inhomogeneous Gain and Loss on Nitride-based Vertical-Cavity Surface Emitting Lasers" Jpn. J. Appl. Phys., **48**, 04C127 (2009)

[4] C.H. Chiu, S. Y. Kuo, **M. H. Lo**, T.C. Wang, Y. T. Lee, H. C. Kuo, T. C. Lu, and S. C. Wang, "Optical Properties of a-plane InGaN/GaN Multiple Quantum Wells on r-plane Sapphire Substrates with Different Indium Compositions," J. Appl. Phys., **105**, N6, 063105 (2009)

[4] Zhen-Yu Li, Wu-Yih Uen, **Ming-Hua Lo**, Ching-Hua Chiu, Po-Chun Lin, Chih-Tsang Hung, Tien-Chang Lu, Hao-Chung Kuo, Shing-Chung Wang, and Yen-Chin Huang "Enhancing the Emission Efficiency of In0.2Ga0.8N/GaN MQW Blue LED by Using Appropriately Misoriented Sapphire Substrates " J. Electrochem. Soc. 156, H129 (2009)

[5] Z. Y. Li, T. C. Lu*, H. C. Kuo, S. C. Wang **M. H. Lo**, and K. M. Lau "HRTEM investigation of high reflectance AlN/GaN Distributed Bragg Reflectors by inserting AlN/GaN supperlattice," J. Crystal Growth, **311**, 3089 (2009)

[6] Z. Y. Li, **M. H. Lo**, C. H. Chiu, P. C. Lin, T. C. Lu, H. C. Kuo, S. C. Wang, "Carrier localization degree of InGaN/GaN multiple quantum wells grown on vicinal sapphire substrates," J. Appl. Phys., **105**, 013103 (2009)

[7] C. H. Chiu, Zhen-yu Li, C. L. Chao, **M. H. Lo,** H. C. Kuo, P. C. Yu, T. C. Lu, and S. C. Wang, K. M. Lau, S. J. Cheng, "Efficiency Enhancement of UV/Blue Light Emitting Diodes via Nanoscaled Epitaxial Lateral Overgrowth of GaN on a SiO_2 Nanorod-Array Patterned Sapphire Substrate," J. Crystal Growth, **310,**5150 (2008)
[8] T. S. Ko, T. C. Lu, T. C. Wang, J. R. Chen, **M. H. Lo**, R. C. Gao, H. C. Kuo, and S. C. Wang, J. L. Shen "Optical characteristics of *a*-plane InGaN/GaN multiple quantum wells with different well width grown by metal-organic chemical vapor deposition", J. Appl. Phys., **104**, 093106 (2008)
[9] Z.Y. Li, **M. H. Lo**, C.T. Hung, S.W. Chen, T. C. Lu, H. C. Kuo and S. C. Wang "High quality ultraviolet AlGaN/GaN multiple quantum wells grown by using atomic layer deposition technique", Appl. Phys. Lett., **93**, 131116, (2008)
[10] C.H. Chiu, **M. H. Lo**, T. C. Lu, P. Yu, H.C. Kuo, H. W. Huang, and S.C. Wang, "Nano-processing Techniques Applied in GaN-based Light Emitting Devices with Self-assembly Ni Nano-masks", IEEE J. Lightwave Tech.,**26**,1445 (2008)
[11] Ching-Hua Chiu, Chia-En Lee, **Ming-Hua Lo**, Hung-Wen Huang, Tien-Chang Lu, Hao-Chung Kuo and Shing Chung Wang "Metal organic chemical vapor deposition growth of GaN-based light emitting diodes with naturally formed nano pyramids", Jpn. J. Appl. Phys., **47**, 2954 (2008)
[12] Zhen-Yu Li, Wu-Yih Uen, **Ming-Hua Lo**, Ching-Hua Chiu, Po-Chun Lin, Chih-Tsang Hung, Tien-Chang Lu, Hao-Chung Kuo, Shing-Chung Wang, Yen-Chin Huang, "Enhancing the emission efficiency of $In_{0.2}Ga_{0.8}N$/GaN MQW blue LED by using appropriately misoriented sapphire substrates," J. Electrochem. Soc., **156**, H129 (2008)
[13] C. H. Chiu, **M. H. Lo**, C. F. Lai, T. C. Lu, Y. A. Chang, H. W. Huang, H. C. Kuo, S. C. Wang, C. F. Lin, and Y. K. Kuo, "Optical properties of high Indium $In_{0.3}Ga_{0.7}N$/GaN MQW green nanorods by plasma etching with nanoscale nickel metal islands", Nanotechnology, **18**, 335706 (2007)
[14] G. S. Huang, H. C. Kuo, **M. H. Lo**, T. C. Lu, S. C. Wang, and J. Y. Tsai, "Improvement of efficiency and ESD characteristics of ultraviolet light emitting diodes by inserting AlGaN and SiN buffer layers", J. Crystal Growth, **305**,55 (2007)
[15] T. S. Ko, T. C. Lu, T. C. Wang, **M. H. Lo**, J. R. Chen, R. C. Gao, H. C. Kuo, S. C. Wang "Optical characteristics of a-plane InGaN multiple quantum wells with different well width", Appl. Phys. Lett., **90**, 181122, (2007), also selected for the June 2007

issue of Virtual Journal of Ultrafast Science

Conference paper

[1] **Ming-Hua Lo et al.** “Output power enhancement of light-emitting diodes with defect passivation layer” Proc. SPIE 7602, 76021X (2010)

[2] **Ming-Hua Lo**, Po-Min Tu, Chao-HsunWang, Hao-Chung Kuo, Shing-Chung Wang, Hsiao-Wen Zan, Chun-Yen Chang, Shih-Chieh Hsu, Yuh-Jen Cheng and Shih-Cheng Huang “Multilayer Epitaxial Lateral Overgrowth of Light Emitting Diode with Anisotropically Etched GaN/Sapphire Interface” Late News, SSDM (2009)

[3] **M. H. Lo**, S.W. Chen Z.Y. Li. T. C. Lu, H. C. Kuo and S. C. Wang “AlGaN/GaN multiple quantum wells grown by atomic layer deposition Lasers” 2008 Conference on Quantum Electronics and Laser Science. CLEO/QELS (2008).

[4] **M. H. Lo**, Z. Y. Li, J. R. Chen, T. S. Ko, T. C. Lu, H. C. Kuo, and S. C. Wang “AlGaN/GaN multiple quantum wells grown by atomic-layer deposition” Proc. SPIE 6894, 68941V (2008)

[5] **Ming-Hua Lo**, Zhen-Yu Li, Shih-Wei Chen, Jhih-Cang Hong, Ting-Chang Lu, Hao-Chung Kuo, Shing-Chung Wang “AlGaN/GaN multiple quantum wells grown by using atomic layer deposition technique” 1068-C05-07 MRS (2008)

[6] C. H. Chiu, C. L. Chao, **M. H. Lo**, Y. J. Cheng, H. C. Kuo, P. C. Yu, T. C. Lu, S. C. Wang, and K. M. Lau “Epitaxial Lateral Overgrowth of GaN-based Light Emitting Diodes on SiO2” Nanorod-Array Patterned Sapphire Substrates by MOCVD Proc. SPIE 7135, 71351Z (2008)

Patent

[1] **Ming-Hua Lo**, Yuh-Jen Cheng, and Hao-Chung Kuo “Method for fabricating GaN substrates and devices” 製作氮化鎵基板及元件之方法 (美國，台灣申請中)

[2] **Ming-Hua Lo**, Yuh-Jen Cheng, and Hao-Chung Kuo “Fabrication of GaN substrate by defect selective passivation” 以缺陷防護層製作氮化鎵基板半導体元件之方法 (美國，台灣申請中)

[3] **Ming-Hua Lo**, Yuh-Jen Cheng, and Hao-Chung Kuo”Method for fabricating semiconductor substrates and smiconductor devices” 製作氮化鎵基板之方法 (美國，台灣申請中)